DEVELOPMENT OF NOVEL SERIES AND PARALLEL SENSING SYSTEM BASED ON NANOSTRUCTURED SURFACE ENHANCED RAMAN SCATTERING SUBSTRATE FOR BIOMEDICAL APPLICATION

BY

TE-WEI CHANG

DISSERTATION

Submitted in partial fulfillment of the requirements
for the degree of Doctor of Philosophy in Electrical and Computer Engineering
in the Graduate College of the
University of Illinois Urbana-Champaign, 2015

Urbana, Illinois

Doctoral Committee:

Associate Professor Gang Logan Liu, Chair
Professor Brian T. Cunningham
Professor Kyekyoon Kim
Associate Professor Xiuling Li

ABSTRACT

With the advance of nanofabrication, the capability of nanoscale metallic structure fabrication opens a whole new study in nanoplasmonics, which is defined as the investigation of photon-electron interaction in the vicinity of nanoscale metallic structures. The strong oscillation of free electrons at the interface between metal and surrounding dielectric material caused by propagating surface plasmon resonance (SPR) or localized surface plasmon resonance (LSPR) enables a variety of new applications in different areas, especially biological sensing techniques.

One of the promising biological sensing applications by surface resonance polariton is surface enhanced Raman spectroscopy (SERS), which significantly reinforces the feeble signal of traditional Raman scattering by at least 10^4 times. It enables highly sensitive and precise molecule identification with the assistance of a SERS substrate. Until now, the design of new SERS substrate fabrication process is still thriving since no dominant design has emerged yet. The ideal process should be able to achieve both a high sensitivity and low cost device in a simple and reliable way. In this thesis two promising approaches for fabricating nanostructured SERS substrate are proposed: thermal dewetting technique and nanoimprint replica technique. These two techniques are demonstrated to show the capability of fabricating high performance SERS substrate in a reliable and cost efficient fashion. In addition, these two techniques have their own unique characteristics and can be integrated with other sensing techniques to build a serial or parallel sensing system. The breakthrough of a combination system with different sensing techniques overcomes the inherent limitations of SERS detection and leverages it to a whole new level of systematic sensing.

The development of a sensing platform based on thermal dewetting technique is covered as the first half of this thesis. The process optimization, selection of substrate material, and

improved deposition technique are discussed in detail. Interesting phenomena have been found including the influence of Raman enhancement on substrate material selection and hot-spot rich bimetallic nanostructures by physical vapor deposition on metallic seed array, which are barely discussed in past literature but significantly affect the performance of SERS substrate. The optimized bimetallic backplane assisted resonating nanoantenna (BARNA) SERS substrate is demonstrated with the enhancement factor (EF) of 5.8×10^8 with 4.7 % relative standard deviation. By serial combination with optical focusing from nanojet effect, the nanojet and surface enhanced Raman scattering (NASERS) are proved to provide more than three orders of enhancement and enable us to perform stable, nearly single molecule detection.

The second part of this thesis includes the development of a parallel dual functional nano Lycurgus cup array (nanoLCA) plasmonic device fabricated by nanoimprint replica technique. The unique configuration of the periodic nanoscale cup-shaped substrate enables a novel hybrid resonance coupling between SPR from extraordinary (EOT) and LSPR from dense sidewall metal nanoparticles with only single deposition process. The sub-50nm dense sidewall metal nanoparticles lead to high SERS performance in solution based detection, by which most biological and chemical analyses are typically performed. The SERS EF was calculated as 2.8×10^7 in a solution based environment with 10.2 % RSD, which is so far the highest reported SERS enhancement achieved with similar periodic EOT devices. In addition, plasmonic colorimetric sensing can be achieved in the very same device and the sensitivity was calculated as 796 nm/RIU with the FOM of 12.7. It creates a unique complementary sensing platform with both rapid on-site colorimetric screening and follow-up precise Raman analysis for point of care and resource limited environment applications. The implementations of bifunctional sensing on opto-microfluidic and smartphone platforms are proposed and examined here as well.

ACKNOWLEDGMENTS

I would like to express my sincere gratitude to my doctoral thesis advisor Prof. Gang Logan Liu. His broad knowledge, insightful guidance and continuous support encouraged me during my doctoral program. I would never have achieved this without his mentoring.

I am truly grateful to have Prof. Kevin Kim, Prof. Brian Cunningham and Prof. Xiuling Li on my thesis committee. Their comments and suggestions for this thesis are precise and critical, which makes it more rigid and complete. In addition, I especially thank to Prof. Shun-Lien Chuang for the valuable guidance during both lecture and qualifying examinations. I will always keep this great instructor in my mind as my role model.

My colleagues in the Liu Nanobionics Group provided me with endless help in problem discussion, experiment design and execution. I would like to thank Manas Ranjan Gartia, Xinhao Wang, Austin Hsiao, Sujin Seo, Zhida Xu, Yi Chen, Jing Jiang, Lisa Plucinski, Yemaya Bordain, Abid Ameen, Chester Hu and Yuken Ren for being part of the group. My thanks are also due to current and past members of the Liu Nanobionics group for creating a very friendly environment to work in. In addition, I would like to acknowledge the staff of the Micro and Nanotechnology Laboratory, Materials Research Laboratory, and the Beckman Institute at the University of Illinois at Urbana-Champaign for the help in experiment.

I would like to thank my parents for their continuing support throughout my academic endeavors. Finally and most importantly, my deepest gratitude goes to my wonderful wife Yu-Ting Huang for her endless support and unconditional love even as this relationship has crossed thousands of miles over many years. Her care, encouragement and faith in me are always my strongest backup when I face difficulties.

TABLE OF CONTENTS

CHAPTER 1 INTRODUCTION

1.1. Nanoplasmonics: background to application

As the classical talk by Feynman predicted, "There is plenty of room at the bottom." Research in nanotechnology has been studied vigorously in recent decades and exploits numerous intriguing and extraordinary phenomena. Examples abound in various realms: in material science, the basic mechanical properties become totally dissimilar when arrangement of atoms has changed. Carbon nanotube (CNT) is a notable example for its high tensile strength and high elastic modulus which are very different from other allotropes. In mechanics, what would be the major influence in a system may be neglected. For instance, line force, which is usually ignored, plays a more significant role than other traditional major forces like gravity when the scale goes down. In optics, nanophotonics is the study of light behavior when interacting with matter on the nanometer scale, where researchers are discovering new phenomena and developing technologies that go beyond what is possible within conventional scale.

Nanoplasmonics, a branch of nanophotonics, is the study of optical phenomena in the vicinity of nanoscale metal structures. It has drawn considerable attention because of its unique properties which have shown significant advantages in different fields such as nanofabrication [1], optical communication [2] and biological sensing [3-4]. The uniqueness originates from the highly enhanced near field by strong electron oscillation either in propagating surface plasmon resonance (SPR) or localized surface plasmon resonance (LSPR) condition. Among all applications, surface enhanced Raman scattering (SERS) induced by LSPR is considered a powerful analytical tool in biological and chemical studies [5]. SERS has been intensively studied from its theoretical fundamentals to device development, to potential applications. As a result, various design of SERS substrate fabrication processes have been exploited; however, at present there is no dominant

design which meets all criteria. In the following sections of this chapter the details of Raman spectroscopy and SERS fundamental theories are introduced as background for the remainder of the dissertation.

1.2. Raman spectroscopy

Raman scattering was discovered in 1928 by C. V. Raman who later won the Noble Prize in Physics because of this accomplishment [6]. It is the inelastic scattering of incident photons caused by to the molecular vibrational motions. When an electromagnetic wave is incident to a molecule, most of the photons are elastically scattered, as the photon energy remains the same before and after scattering happens. This phenomenon is also known as Rayleigh scattering. However, a small fraction of incident photons (approximately one in one million) lose or gain a certain amount of energy during the interaction with the molecules, thus changing their frequency when they are scattered out. The energy difference is due to energy absorption or release from the electron when it transfers between molecular vibrational states. This energy exchange between electron and photon during the interaction is defined as inelastic scattering. The comparison between Rayleigh and Raman scattering is shown in figure 1.1 (a).

Until now, Raman scattering has been intensively applied in substance analysis as Raman spectroscopy [7]. Similar to infrared (IR) spectroscopy, Raman spectroscopy identifies molecular motion by measuring the molecular vibrational modes from the Raman spectrum. Therefore, the molecular information such as component and orientation can be unambiguously obtained by the scattering peaks from the Raman spectrum. In addition, Raman spectroscopy has many advantages when compared with IR spectroscopy. For example, IR spectroscopy is not suitable for aqueous samples since water absorbs significantly in the infrared range. However, detection of low concentration sample is quite challenging because of the very small scattering cross section of

Raman scattering, typically around 10^{-28} to 10^{-30} cm^2 $molecule^{-1}$ $stereoradian^{-1}$ [8]. For example, in the 1970s researchers attempted to detect monolayers adsorbed on metallic surface in the field of spectroelectrochemistry, which is the real-time observation of the chemical reactions in electrochemical processes by spectroscopy techniques. Since most of the electrochemical system contains metallic electrodes and aqueous environment, Raman spectroscopy was considered as an appropriate candidate. However, the researchers, despite extensive efforts, achieved little success mostly due to the weak signal from traditional Raman spectroscopy.

1.3. Surface enhanced Raman spectroscopy (SERS)

In 1974 Fleischmann *et al.* attempted to increase the number of adsorbed molecules by applying roughened a metallic electrode surface and observed a very high signal-to-noise ratio Raman spectrum [9]. They attributed this enhancement to the larger surface area of roughened silver electrode by electrochemical plating method. Later on two groups independently discovered the enhancement is exaggerated by only taking the increase of surface area into account [10-11]. The concept of enhancement by metallic surface was established by Moskovits and named surface enhanced Raman scattering [12].

After the efforts from many researchers, it has been broadly accepted that this dramatic enhancement is due to two mechanisms: electromagnetic (EM) model and charge transfer (CT) model. According to the EM model, the surface enhanced Raman signal has been enhanced by the electric field localized around the metallic nanostructures from both incident light and scattered Raman radiation. Therefore, the enhancement can be approximately predicted as the ratio between incident and localized electric field to the power of four [13]. Although the EM model fits most of the experiment results and successfully explains the ultrahigh enhancement of SERS, it is not able to explain the SERS performance differences between different chemical structures of probing

molecules. This dependence is due to the appearance of a new electronic state from the metal when the molecule comes in contact with the SERS substrate. Generally the transition from HOMO (highest occupied molecular orbital) to LUMO (lowest unoccupied molecular orbital) is possible with excitation such as UV light because of its high energy gap between HOMO and LUMO for most molecules. However, with the assistance of an additional electronic state from the surface metal, the transition becomes feasible with visible light excitation [14]. This mechanism of enhancement is known as the charge transfer model, as shown in figure 1.1 (b).

As a result, the theoretical total enhancement from the SERS substrate is a multiplication of the EM model and CT model. For SERS performance measurement, enhancement factor (EF) has been broadly used and is defined as follows [15]:

$$EF = \frac{I_{SERS}}{N_{SERS}} \frac{N_{Ref}}{I_{Ref}}$$

where I_{SERS} and I_{Ref} are scattered intensity of Raman signal from SERS substrate and reference. N_{SERS} and N_{Ref} are the number of molecules being probed by SERS and reference respectively.

In the aspect of SERS substrate fabrication, the EM model is more significant, since the SERS performance is able to be controlled by tuning the geometrical parameters of SERS substrate such as feature size, shape and spacing. This is because adjusting geometrical features of the SERS substrate leads to the modification of localized surface plasmon resonance (LSPR). The basics of LSPR will be introduced in next section, which also explains how it is related to SERS performance.

1.4. Localized surface plasmon resonance (LSPR)

A plasmon is defined as the dense fluctuation of free electrons. When an incident electromagnetic wave radiates to a metal particle or roughened metal surface with feature size smaller than the incident wavelength, the electrons inside the metal will perform a collective oscillation at frequency of the excitation electromagnetic wave. Due to the assumption of the feature size of the metallic structure/particle, it can be considered a quasi-static condition, which means the electric field across the whole metallic structure/particle is constant. Under this condition, the Laplace equation can be applied to solve the electric potential in the whole domain. According to the analytical solution from the Laplace equation, the metallic structure/particle can be treated as a Hertzian dipole antenna which forms higher electric field around the particle [13]. This phenomenon is known as localized surface plasmon resonance (LSPR) and shown in figure 1.2 (a). Researchers have found that the geometry of the metal nanostructure has a significant effect on the LSPR position and intensity. Figure 1.2 (b) shows the schematics of some available nanostructures, and the corresponding field enhancements are shown in the same figure as well. Therefore, the LSPR-induced highly localized field at resonance condition provides the possibility to tune the local field and thus influences the SERS performance according to the EM model.

For decades, researchers have attempted to fabricate a variety of different SERS substrates with many different methods. In the following chapter the current progress on SERS substrate fabrication will be introduced and the motivation of designing an advantageous nanostructured SERS substrate and combined systematic platforms will be proposed as well.

1.5. Overview of thesis

In this thesis, the development of fabrication techniques for industrially nanostructured SERS substrate with both high sensitivity and production feasibility will be studied in detail. In addition, two novel sensing systems based on nanostructured SERS substrate, series with optical nanojet focusing and parallel plasmonic colorimetric screening, are proposed and studied. Chapter 2 summarizes current state-of-the-art approaches to SERS substrate fabrication processes and provides a comprehensive comparison. Chapter 3 mainly includes the details of nanostructured backplane assisted resonating nanoantenna array (BARNA) SERS substrate from its design, fabrication process, and optimization to applications. This SERS substrate is fabricated based on thermal dewetting technique and the benefits of utilizing such technique are shown here as well. Chapter 4 discusses the influence on SERS performance due to the optical properties of different substrate materials. It manifests the significance of substrate material selection, which has been ignored by the past research. In addition, an improved process, seed assisted deposition, is demonstrated in chapter 5 and is shown to be a direct and simple method to achieve bimetallic nanostructure array for further improvement on sensitivity and uniformity as well as reducing fabrication complexity at the same time. In chapter 6, a novel sensing system combined with nanojet and surface enhanced Raman scattering (NASERS) on nanostructured bimetallic BARNA substrate is proposed and demonstrated to show a promising way to perform highly stable, ultrahigh sensitive sensing for molecule-level detection.

Chapter 7 is an introduction to the nano Lycurgus cup array (nanoLCA) plasmonic device, which is fabricated by nanoimprnt replica method and contains a highly uniform periodic nanoscale cup-shaped array with compact sidewall nanoparticles. This unique configuration has been shown to be a hybrid SPR and LSPR resonance, which enables both colorimetric sensing and

SERS detection performed at the same device. The dual-functional property of nanoLCA plasmonic device provides a complementary parallel sensing system for point-of-care or in-line screening applications. Chapter 8 discusses the current progress on exploring the biomedical applications with bifunctional nanoLCA device in opto-microfluidic drug screening and mobile phone-based point-of-care personal health monitoring platforms.

1.6. Figures

(a) (b)

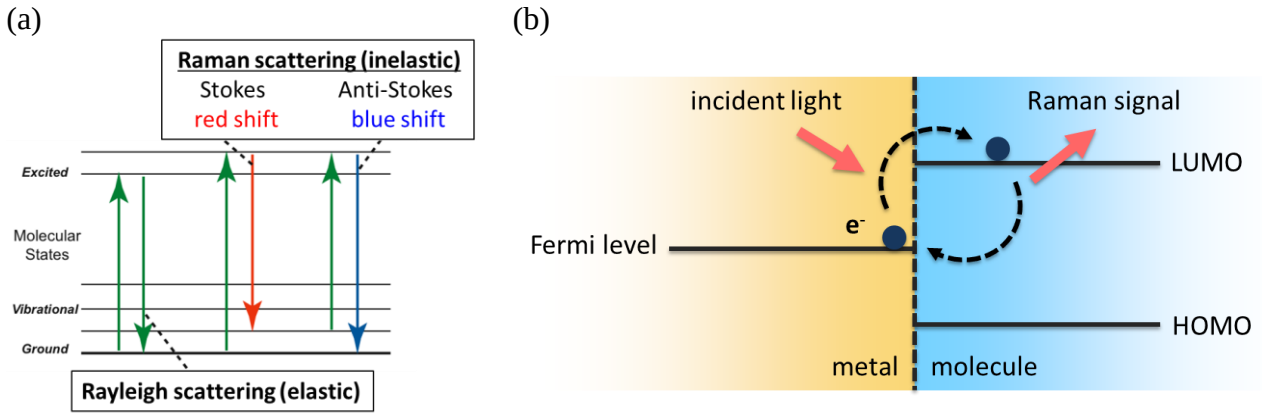

Figure 1.1 (a) Comparison of Rayleigh scattering, Stokes and anti-Stokes Raman scattering. (b) Schematic of charge transfer model mechanism.

(a) (b)

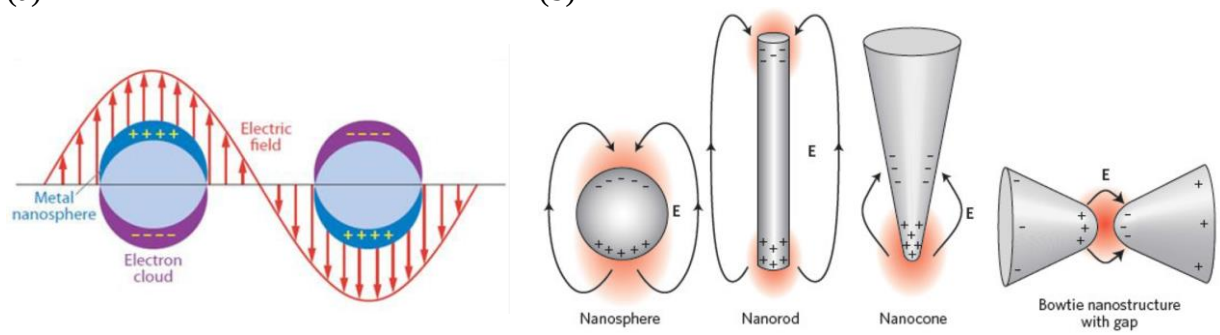

Figure 1.2 (a) Schematic of localized surface plasmon resonance (LSPR) (adapted from [16]). (b) Examples of some commonly used nanostructure for LSPR including nanosphere, nanorod, nanocone and bowtie nanostructure (adapted from [17]).

1.7. References

[1] Pan, L.; Park, Y.; Xiong, Y.; Ulin-Avila, E.; Wang, Y.; Zeng, L.; Xiong, S.; Rho, J.; Sun, C.; Bogy, D. B.; Zhang, X. Maskless Plasmonic Lithography at 22 Nm Resolution. *Scientific Reports* **2011**, *1*, 175.

[2] Maier, S. A.; Atwater, H. A. Plasmonics: Localization and Guiding of Electromagnetic Energy in metal/dielectric Structures. *J. Appl. Phys.* **2005**, *98*, 011101.

[3] Camden, J. P.; Dieringer, J. A.; Wang, Y.; Masiello, D. J.; Marks, L. D.; Schatz, G. C.; Van Duyne, R. P. Probing the Structure of Single-Molecule Surface-Enhanced Raman Scattering Hot Spots. *J. Am. Chem. Soc.* **2008**, *130*, 12616.

[4] Thanh, N. T. K.; Rosenzweig, Z. Development of an Aggregation-Based Immunoassay for Anti-Protein A using Gold Nanoparticles. *Anal. Chem.* **2002**, *74*, 1624-1628.

[5] Kneipp, K.; Kneipp, H.; Kneipp, J. Surface-Enhanced Raman Scattering in Local Optical Fields of Silver and Gold Nanoaggregates - from Single-Molecule Raman Spectroscopy to Ultrasensitive Probing in Live Cells. *Acc. Chem. Res.* **2006**, *39*, 443-450.

[6] Raman, C.; Krishnan, K. A New Type of Secondary Radiation. *Nature* **1928**, *121*, 501-502.

[7] Kneipp, K.; Kneipp, H.; Itzkan, I.; Dasari, R.; Feld, M. Ultrasensitive Chemical Analysis by Raman Spectroscopy. *Chem. Rev.* **1999**, *99*, 2957.

[8] Fan, M.; Andrade, G. F. S.; Brolo, A. G. A Review on the Fabrication of Substrates for Surface Enhanced Raman Spectroscopy and their Applications in Analytical Chemistry. *Anal. Chim. Acta* **2011**, *693*, 7-25.

[9] Fleischmann, M.; Hendra, P.; McQuillan A. J. Raman-Spectra from Electrode Surfaces. *J. Chem. Soc. Chem. Commun.* **1973**, 80-81.

[10] Jeanmaire, D.; Vanduyne, R. Surface Raman Spectroelectrochemistry .1. Heterocyclic, Aromatic, and Aliphatic-Amines Adsorbed on Anodized Silver Electrode. *J Electroanal Chem* **1977**, *84*, 1-20.

[11] Albrecht, M.; Creighton, J. Anomalously Intense Raman-Spectra of Pyridine at a Silver Electrode. *J. Am. Chem. Soc.* **1977**, *99*, 5215-5217.

[12] Moskovits, M. Surface-Roughness and Enhanced Intensity of Raman-Scattering by Molecules Adsorbed on Metals. *J. Chem. Phys.* **1978**, *69*, 4159-4161.

[13] Willets, K. A.; Van Duyne, R. P. Localized Surface Plasmon Resonance Spectroscopy and Sensing. *Annu. Rev. Phys. Chem.* **2007**, *58*, 267-297.

[14] Lombardi, J. R.; Birke, R. L.; Lu, T. H.; Xu, J. Charge-Transfer Theory of Surface Enhanced Raman-Spectroscopy - Herzberg-Teller Contributions. *J. Chem. Phys.* **1986**, *84*, 4174-4180.

[15] Gopinath, A.; Boriskina, S. V.; Reinhard, B. M.; Dal Negro, L. Deterministic Aperiodic Arrays of Metal Nanoparticles for Surface-Enhanced Raman Scattering (SERS). *Optics Express* **2009**, *17*, 3741-3753.

[16] Lu, X.; Rycenga, M.; Skrabalak, S. E.; Wiley, B.; Xia, Y. Chemical Synthesis of Novel Plasmonic Nanoparticles. Annu. Rev. Phys. Chem. 2009, 60, 167-192.

[17] Kawata, S.; Inouye, Y.; Verma, P. Plasmonics for Near-Field Nano-Imaging and Superlensing. *Nature Photonics* **2009**, *3*, 388-394.

CHAPTER 2 LITERATURE REVIEW AND MOTIVATION

In this chapter, a review on current state-of-the-art SERS substrate fabrication techniques will be introduced. In addition, the advantages and disadvantages of each process will be discussed. After comparing all the existing techniques, two approaches based on thermal dewetting and nanoimprint replica technique are proposed to overcome the hindrance of current technology and enable a SERS technique for practical application.

2.1. Introduction

Soon after the SERS effect was discovered, metallic nanoparticles (MNPs) were widely studied due to their much higher enhancement when compared to roughened metallic surface. Later research on nanostructured metallic surface has been emphasized since it took advantage of rapid progress in recent nanofabrication techniques and possibilities for optimization of geometrical parameters for SERS performance. Until now, many decades of research have been devoted to create practical SERS substrates for industrial application and a large number of different fabrication techniques have emerged. Generally SERS substrates can be classified into three main categories: (1) MNPs in suspension; (2) MNPs immobilized on solid substrates and (3) nanostructures fabricated directly on solid substrate [1]. The most well-known and representative SERS substrates and their fabrication techniques will be introduced in the following sections.

2.2. Criteria of ideal SERS substrate

Before introducing any SERS substrate fabrication techniques, the criteria of ideal SERS substrate should be elaborated in order to create a standard for comparison. Followings are the criteria to define an ideal SERS substrate [2]:

(1) Either MNPs or metallic nanostructure should be arranged periodically or regularly.

(2) The fabrication of the SERS substrate must be reproducible from batch to batch.

(3) The signal enhancement has to be homogenous both across the surface and from batch-to-batch.

(4) The SERS substrate needs to have long-term stability and be insensitive to environmental influences, e.g., oxygen, humidity, and light.

(5) The SERS surface has to show a large enhancement factor, potentially down to single-molecule sensitivity.

(6) The SERS substrate should be biocompatible when the application is for biological sensing or investigation of biological specimens.

(7) All kinds of substances must be detectable including molecules with and without resonance Raman effects or fluorescent molecules used as molecular labels in bioanalytics.

(8) The SERS substrate should be cost-efficient and with a simple fabrication protocol.

2.3. Metallic nanoparticles in suspension

Metallic nanoparticles (MNPs) in suspension was applied for SERS application not long after the discovery of the SERS phenomenon and therefore has been studied for a long time. It is defined as a certain concentration of the probed molecules which is mixed in the sample solution with MNPs. The Raman signal can be enhanced by the presence of probed molecules in the proximity of MNPs. MNPs are mostly fabricated by "bottom-up" chemical synthesis and several well-established processes are available [3-4]. A variety of shapes have been prepared such as spheres [5], nanorods, nanoprisms [6], bipyramids [7], nanostars [8] and polyhedral [9] as shown in figure 2.1. Among all shapes, highly faceted MNPs have drawn more interest, since the facet edges or tips provide higher localized electric field and therefore ultrahigh enhancement (EF around 10^{10}) can be achieved by such geometry [10]. Besides the high SERS performance, they

show several other advantages such as good stability and ease of fabrication. Because of these advantages, MNP suspension has been used for initial single molecule SERS detection [11].

However, the main drawback of this method is the non-uniform distribution of MNPs. When MNPs are suspended in the solution, the aggregation of MNPs can easily happen and reproducibility of the Raman signal becomes barely possible. On the other hand, sometimes aggregation is essential for achieving high SERS performance [12-13].

2.4. Metallic nanoparticles immobilized on solid substrates

As discussed in the previous section, MNPs perform as a good method to achieve high SERS enhancement by aggregation, but simultaneously the problem of non-reproducibility arises. In order to mitigate this problem, Natan's group proposed synthesizing MNPs by wet chemistry and then immobilizing the MNPs onto the solid supporting substrate [14]. After this concept came to light, it quickly drew researchers' attention and several different methods to immobilize MNPs were developed. The most dominant method is self-assembly, in which MNPs are immobilized on the surface by chemically pre-treating surface or intrinsic physical properties of MNPs.

Chemical attachment is achieved by polymer functionalization with the amine or thiol groups on the surface of the supporting substrate [15]. These functional groups can be anchored onto the surface and also can capture MNPs at the same time. Figure 2.2 shows the general process of chemical attachment. This procedure is beneficial for higher reproducibility than MNPs in suspension. In addition, wide range of choices in process, such as choosing functional groups, incubation temperature between MNPs and surface, concentration of MNPs and surface adsorbates on the MNPs, provide researchers room to tune and achieve large SERS enhancement. Flat surface

chemical attachment method was also successfully applied on non-flat surface material such as Ag nanowires [16] and optical fiber tip [17].

This chemical self-assembly method can also be extended to a "multi-layer" MNP design [18]. In this case, additional MNPs are deposited layer by layer after the first monolayer is deposited. By applying multi-layer method, morphology similar to aggregation of MNPs in suspension can be observed and enhance the SERS performance by 2-3 orders when compared with monolayer configuration [19]. Surprisingly, the spatial and sample-to-sample Raman signal variation reduces as the number of deposited MNP layers increases [20].

Another popular self-assembly method is via electrostatic attraction of polymers and biomolecules. Polymer examples are immobilization Ag nanoparticles (AgNPs) on Ag thin film by Poly(vinylpyridine) [21] and immobilization Au nanoparticles (AuNPs) on Au electrode by polyvinylpyrrolidone(PVP) [22] as shown in figure 2.3(a). Cheng et al. claimed that the enhanced localized electric field can not only happen between MNPs but also in the contact of metallic thin film and MNPs, which provides higher stability of SERS performance than other MNPs immobilized SERS substrate. Biomolecule examples include DNA and proteins, which act as linkers for MNPs immobilization. Nicholas *et al.* utilized avidin as both the linker to bind AgNPs with the surface and recognition index of SERS performance as shown in figure 2.3(b) [23]. In addition to chemical and electrostatic methods, other different techniques were developed such as capillary force [24] and direct transfer from pre-assembled MNP film [25].

Although immobilization of MNPs provides a considerable improvement on MNP suspension in reproducibility and other benefits discussed above, other critical problems still arise. For example, further step of immobilization requires additional time, from several hours to a few days, and dramatically delays the production rate of SERS substrate. In addition, most of the

chemical molecules used for immobilization induce undesired Raman signals, which might interfere and mislead the identification of probed molecule. Finally, the problem of the probed molecule requiring pre-treatment in order to stay in between MNPs is still not solved by this modification.

2.5. Nanostructures fabricated directly on solid substrate

This section is mainly focused on SERS substrates where metallic nanostructures are fabricated directly on the supporting substrate by different nanofabrication processes. This type of fabrication technique is known as “top-down” method in opposition to “bottom-up” MNP synthesis methods discussed in the previous two sections. Depending on the morphology of the nanostructure, this kind of SERS nanostructured substrate can be classified as periodic or randomized.

(1) Periodic nanostructured SERS substrate

Direct writing method including electron beam lithography (EBL) and focused ion beam (FIB) technique utilizes a finely focused beam of electrons or ions (usually gallium) to directly create a periodic pattern either on the e-beam resist or metallic thin film. The accelerated energy of the electron or ion beam ranges from 1 to 50 keV. This method is considered a perfect candidate to create precise patterning in terms of size, shape and inter-spacing of nanostructure. With the excellent controllability, an arbitrary periodic pattern with ultrahigh accuracy can be fabricated and plays a significant role to establish and verify SERS theory [26]. With the assistance of this method, researchers have identified ultrahigh enhancement of nanostructured SERS substrate mainly attributed to the hot-spot effect, by which LSPR can be coupled to induce large localized field when the inter-spacing of two or more metallic nanostructures is down to the order of few

nanometers [27]. SERS substrates with sub-10 nm hot spot have been fabricated by both e-beam lithography [28] and FIB technique [29] as shown in figure 2.4 (a) and (b). However, the inevitably time-consuming process limits the direct writing method for laboratory application only.

Another popular method is the nanosphere template technique, which is based on applying one or multiple layers of self-assembled nanospheres on the solid support surface by vapor [30] or electrochemical [31] metal deposition. After removal of the nanosphere mask, a periodic metal nanostructure deposited through the interspace among nanospheres can be achieved. The nanostructures can be either triangular or hexagonal depending on the number of layers of nanosphere mask used [32-34]. Also the in-plane and out-of-plane diameters of nanostructures can be controlled with appropriate deposition condition. Through nanosphere template technique, the relationship between LSPR resonance and SERS performance has been examined and high enhancement (EF~10^8) has been reported [35]. Instead of removing the nanosphere array, metal film over nanosphere (FON) SERS substrate shows high LPSR resonance at the junctions among nanospheres [36]. In addition, spinning during the deposition causes a shuttering effect and leads to immobilized nanorod assembly (INRA) SERS substrate on nanopshere array [37]. The diameter of nanorods corresponding to LSPR resonance wavelength can be controlled by applied diameter of nanospheres, which means that IRNA SERS substrate can be optimized and matched with the excitation laser of the system. Nanosphere template methods provide a higher efficiency to fabricate precise periodic nanostructured SERS substrate compared with direct writing method. Nevertheless, a highly uniform nanosphere monolayer with industrially practical area (e.g. wafer scale) still requires a delicate process and is extremely difficult to achieve.

Anodic alumina oxide (AAO) membrane was also used as the nanostructured template for SERS substrate fabrication. AAO obtained by high-voltage dissolution of alumina in acid solution

contains hexagonal periodic nanopores with size of tens of nanometers. Different shapes of metallic nanostructure can be fabricated by either vapor [38] or electrochemical [39] deposition. However, similar to most of the chemically treated nanostructured substrates, AAO technique suffers from time-consuming and complicated dissolution process [40].

(2) Randomized nanostructured SERS substrate

In comparison to periodic nanostructure, randomized nanostructured SERS substrate often requires less delicate fabrication. Large-area and highly efficient fabrication which meets industrial requirements is easily realized. As shown in figure 2.5, several different methods have been explored including maskless black silicon etching [41], metal nanorods by oblique vapor deposition [42], annealed AuNPs on carbon nanotube template [43], electrochemical deposition on polycarbonate membranes (PCM) [44] and Ag nanostructures on porous Si substrate [45]. The main drawback of this category is the randomness of the nanostructures, which leads to higher spatial and batch-to-batch variation on SERS performance when compared to the periodic case. This disadvantage hinders this category of SERS substrates in the performance of quantitative chemical analysis.

Table 2.1 lists all the SERS substrate fabrication techniques discussed above as well as the commercially available commercial Klarite SERS substrate [46] and rates them with ideal SERS substrate criteria (reproducibility, high sensitivity, cost efficiency, fabrication simplicity and fabrication time). It can be obviously seen that current techniques cannot provide a comprehensive solution to fabricate SERS substrate that meets industrial standard. In the following chapters two approaches will be introduced, thermal dewetting technique in chapter 3 and nanoimprint replica technique in chapter 7, which meet all the criteria. The details of these two approaches will be explicitly described in the two chapters.

2.6. Figures and table

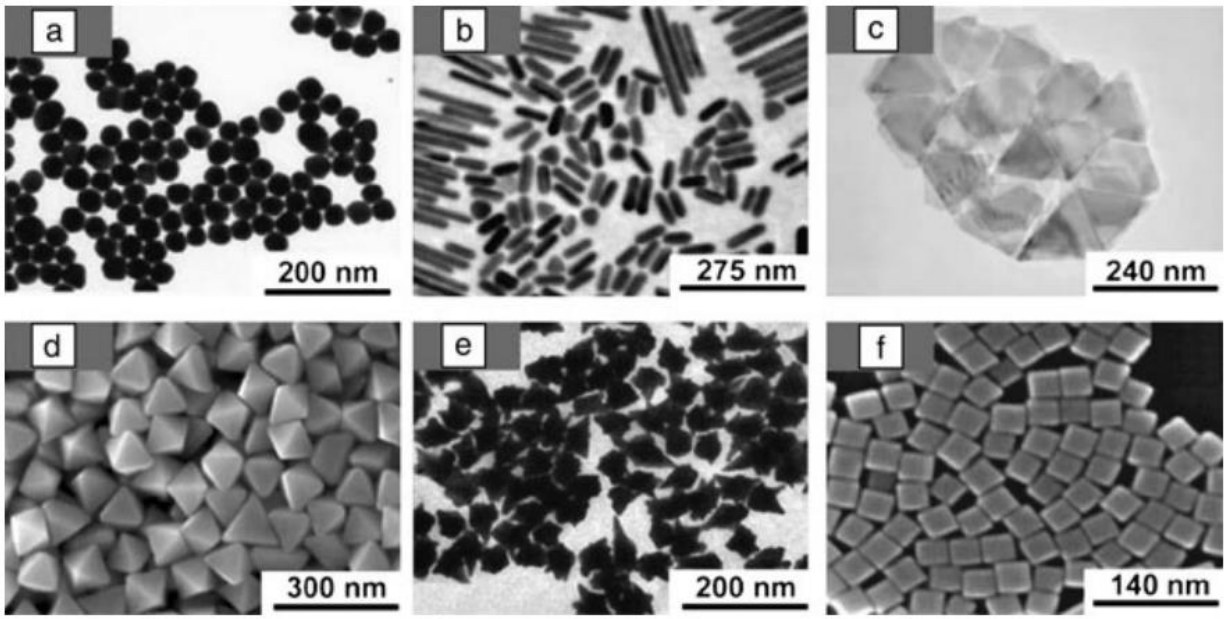

Figure 2.1 (a) Transmission electron microscopy (TEM) images of Au nanospheres. (b) TEM images of Au nanorods. (c) TEM images of Au nanoprisms. (d) SEM images of Au bipyramids; (e) TEM images of Au nanostars. (f) SEM images of Ag polyhedra (All images are adapted from [13].)

Figure 2.2 Example of chemical attachment method for self-assembly MNPs on glass slide. X can be CN, NH_2, 2-pyridyl, $P(C_6H_5)_2$, or SH; R=CH_3 or CH_2CH_3 (adapted from [1].)

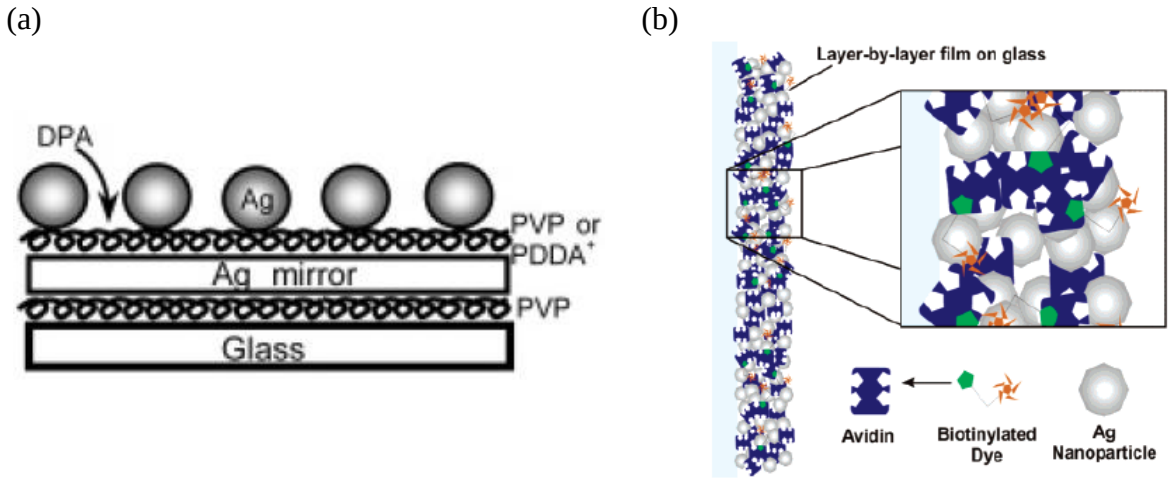

Figure 2.3 Examples of electrostatic self-assembled MNPs; (a) AgNPs on Ag thin film by applying Poly(vinylpyridine). (b) AgNPs on Ag thin film by avidin.

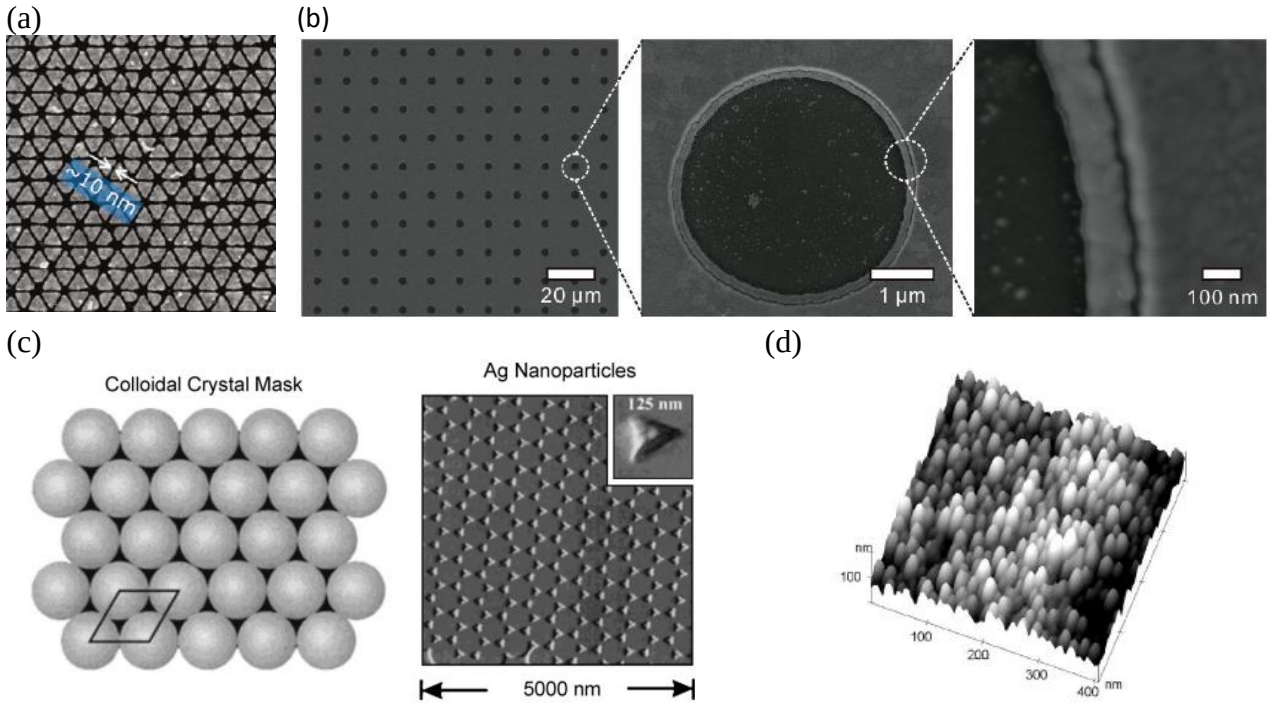

Figure 2.4 (a) SEM image of periodic SERS substrate fabricated by EBL. (b) Low and high magnitude SEM image of periodic SERS substrate fabricated by FIB. (c) Schematic and SEM images of SERS substrate fabricated by nanosphere template technique. (d) AFM result of silver deposited AAO template for SERS application.

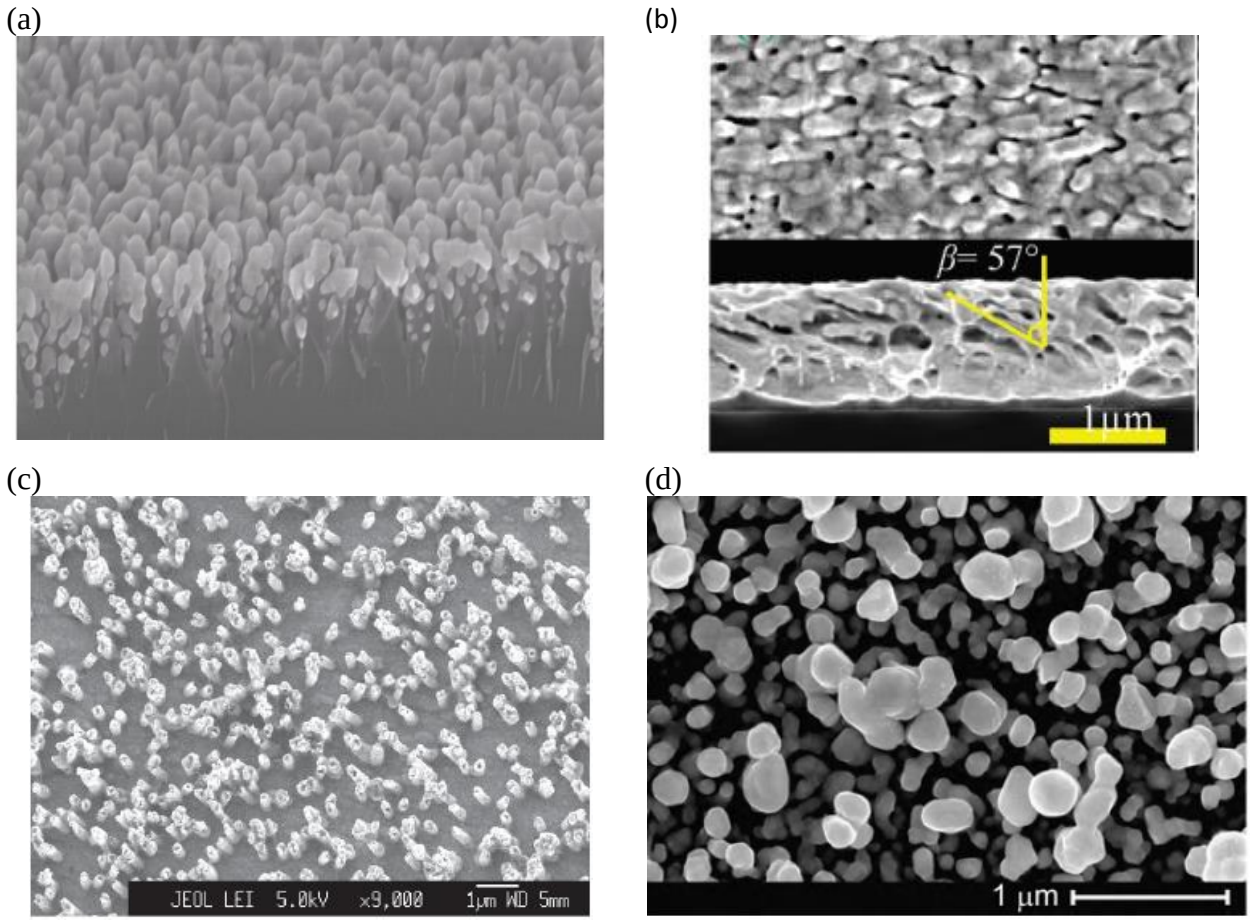

Figure 2.5 (a) SEM image of randomized SERS substrate fabricated by maskless black silicon etching. (b) Top and cross section SEM image of randomized SERS substrate fabricated by oblique vapor deposition. (c) SEM images of randomized SERS substrate fabricated by electrochemical deposition on PCM. (d) SEM images of randomized SERS substrate fabricated by Ag deposition on porous Si substrate.

Table 2.1 The comparison among SERS substrates fabricated by a variety of different fabrication techniques and rated in the categories of reproducibility, sensitivity, cost efficiency, fabrication simplicity and fabrication time.

	Reproducibility	Sensitivity	Cost efficiency	Fabrication Simplicity	Fabrication Time
MNPs in suspension	Low (Random)	High	High	High	Long
Immobilized MNPs on substrate	Medium (Random)	High (with interference)	Medium	Medium	Very Long
Direct writing technique	High (Periodic)	High	Low	Very Low	Very Long
Nanosphere template technique	High (Periodic)	High	High	Low	Low
AAO template technique	High (Periodic)	Medium	Medium	Medium	Long
Randomized SERS substrate	Medium (Random)	High	High	High	Low
Commercial Klarite SERS substrate	High (Periodic)	Low	Medium	High	Medium
Thermal dewetting technique	Medium-High (Semi-random)	High	High	High	Low
Nanoimprint replica technique	High (Periodic)	Medium-High	High	High	High

2.7. References

[1] Fan, M.; Andrade, G. F. S.; Brolo, A. G. A Review on the Fabrication of Substrates for Surface Enhanced Raman Spectroscopy and their Applications in Analytical Chemistry. *Anal. Chim. Acta* **2011**, *693*, 7-25.

[2] Cialla, D.; Maerz, A.; Boehme, R.; Theil, F.; Weber, K.; Schmitt, M.; Popp, J. Surface-Enhanced Raman Spectroscopy (SERS): Progress and Trends. Analytical and Bioanalytical Chemistry 2012, 403, 27-54.

[3] Lee, P. C.; Meisel, D. Adsorption and Surface-Enhanced Raman of Dyes on Silver and Gold Sols. *J. Phys. Chem.* **1982**, *86*, 3391-3395.

[4] Frens, G. Controlled Nucleation for Regulation of Particle-Size in Monodisperse Gold Suspensions. *Nature-Physical Science* **1973**, *241*, 20-22.

[5] Bastus, N. G.; Comenge, J.; Puntes, V. Kinetically Controlled Seeded Growth Synthesis of Citrate-Stabilized Gold Nanoparticles of Up to 200 Nm: Size Focusing Versus Ostwald Ripening. *Langmuir* **2011**, *27*, 11098-11105.

[6] Millstone, J. E.; Wei, W.; Jones, M. R.; Yoo, H.; Mirkin, C. A. Iodide Ions Control Seed-Mediated Growth of Anisotropic Gold Nanoparticles. *Nano Letters* **2008**, *8*, 2526-2529.

[7] Niu, W.; Zheng, S.; Wang, D.; Liu, X.; Li, H.; Han, S.; Chen, J.; Tang, Z.; Xu, G. Selective Synthesis of Single-Crystalline Rhombic Dodecahedral, Octahedral, and Cubic Gold Nanocrystals. *J. Am. Chem. Soc.* **2009**, *131*, 697-703.

[8] Sau, T. K.; Rogach, A. L.; Doeblinger, M.; Feldmann, J. One-Step High-Yield Aqueous Synthesis of Size-Tunable Multispiked Gold Nanoparticles. *Small* **2011**, *7*, 2188-2194.

[9] Xia, X.; Zeng, J.; Zhang, Q.; Moran, C. H.; Xia, Y. Recent Developments in Shape-Controlled Synthesis of Silver Nanocrystals. *Journal of Physical Chemistry C* **2012**, *116*, 21647-21656.

[10] Rodriguez-Lorenzo, L.; Alvarez-Puebla, R. A.; Pastoriza-Santos, I.; Mazzucco, S.; Stephan, O.; Kociak, M.; Liz-Marzan, L. M.; Javier Garcia de Abajo, F. Zeptomol Detection through Controlled Ultrasensitive Surface-Enhanced Raman Scattering. *J. Am. Chem. Soc.* **2009**, *131*, 4616-+.

[11] Kneipp, K.; Wang, Y.; Kneipp, H.; Perelman, L. T.; Itzkan, I.; Dasari, R.; Feld, M. S. Single Molecule Detection using Surface-Enhanced Raman Scattering (SERS). *Phys. Rev. Lett.* **1997**, *78*, 1667-1670.

[12] Pieczonka, N. P. W.; Aroca, R. F. Inherent Complexities of Trace Detection by Surface-Enhanced Raman Scattering. *Chemphyschem* **2005**, *6*, 2473-2484.

[13] Sharma, B.; Cardinal, M. F.; Kleinman, S. L.; Greeneltch, N. G.; Frontiera, R. R.; Blaber, M. G.; Schatz, G. C.; Van Duyne, R. P. High-Performance SERS Substrates: Advances and Challenges. *MRS Bull* **2013**, *38*, 615-624.

[14] Freeman, R. G.; Grabar, K. C.; Allison, K. J.; Bright, R. M.; Davis, J. A.; Guthrie, A. P.; Hommer, M. B.; Jackson, M. A.; Smith, P. C.; Walter, D. G.; Natan, M. J. Self-Assembled Metal Colloid Monolayers - an Approach to SERS Substrates. *Science* **1995**, *267*, 1629-1632.

[15] Toderas, F.; Baia, M.; Baia, L.; Astilean, S. Controlling Gold Nanoparticle Assemblies for Efficient Surface-Enhanced Raman Scattering and Localized Surface Plasmon Resonance Sensors. *Nanotechnology* **2007**, *18*, 255702.

[16] Lee, S. J.; Baik, J. M.; Moskovits, M. Polarization-Dependent Surface-Enhanced Raman Scattering from a Silver-Nanoparticle-Decorated Single Silver Nanowire. *Nano Letters* **2008**, *8*, 3244-3247.

[17] Andrade, G. F. S.; Fan, M.; Brolo, A. G. Multilayer Silver Nanoparticles-Modified Optical Fiber Tip for High Performance SERS Remote Sensing. *Biosens. Bioelectron.* **2010**, *25*, 2270-2275.

[18] Ko, H.; Singamaneni, S.; Tsukruk, V. V. Nanostructured Surfaces and Assemblies as SERS Media. *Small* **2008**, *4*, 1576-1599.

[19] Addison, C. J.; Brolo, A. G. Nanoparticle-Containing Structures as a Substrate for Surface-Enhanced Raman Scattering. *Langmuir* **2006**, *22*, 8696-8702.

[20] Fan, M.; Brolo, A. G. Self-Assembled Au Nanoparticles as Substrates for Surface-Enhanced Vibrational Spectroscopy: Optimization and Electrochemical Stability. Chemphyschem 2008, 9, 1899-1907.

[21] Daniels, J. K.; Chumanov, G. Nanoparticle-Mirror Sandwich Substrates for Surface-Enhanced Raman Scattering. *J Phys Chem B* **2005**, *109*, 17936-17942.

[22] Cheng, H.; Huan, S.; Wu, H.; Shen, G.; Yu, R. Surface-Enhanced Raman Spectroscopic Detection of a Bacteria Biomarker using Gold Nanoparticle Immobilized Substrates. *Anal. Chem.* **2009**, *81*, 9902-9912.

[23] Pieczonka, Nicholas P. W.; Goulet, P. J. G.; Aroca, R. F. Chemically Selective Sensing through Layer-by-Layer Incorporation of Biorecognition into Thin Film Substrates for Surface-Enhanced Resonance Raman Scattering. *J. Am. Chem. Soc.* **2006**, *128*, 12626-12627.

[24] Kahraman, M.; Yazici, M. M.; Sahin, F.; Culha, M. Convective Assembly of Bacteria for Surface-Enhanced Raman Scattering. *Langmuir* **2008**, *24*, 894-901.

[25] Yun, S.; Park, Y.; Kim, S. K.; Park, S. Linker-Molecule-Free Gold Nanorod Layer-by-Layer Films for Surface-Enhanced Raman Scattering. *Anal. Chem.***2007**, *79*, 8584-8589.

[26] Yu, Q.; Guan, P.; Qin, D.; Golden, G.; Wallace, P. M. Inverted Size-Dependence of Surface-Enhanced Raman Scattering on Gold Nanohole and Nanodisk Arrays. *Nano Letters* **2008**, *8*, 1923-1928.

[27] Gunnarsson, L.; Bjerneld, E. J.; Xu, H.; Petronis, S.; Kasemo, B.; Kall, M. Interparticle Coupling Effects in Nanofabricated Substrates for Surface-Enhanced Raman Scattering. *Appl. Phys. Lett.* **2001**, *78*, 802-804.

[28] Duan, H.; Hu, H.; Kumar, K.; Shen, Z.; Yang, J. K. W. Direct and Reliable Patterning of Plasmonic Nanostructures with Sub-10-Nm Gaps. *Acs Nano* **2011**,*5*, 7593-7600.

[29] Im, H.; Bantz, K. C.; Lindquist, N. C.; Haynes, C. L.; Oh, S. Vertically Oriented Sub-10-Nm Plasmonic Nanogap Arrays. *Nano Letters* **2010**, *10*, 2231-2236.

[30] Haynes, C. L.; Van Duyne, R. P. Nanosphere Lithography: A Versatile Nanofabrication Tool for Studies of Size-Dependent Nanoparticle Optics. *J Phys Chem B* **2001**, *105*, 5599-5611.

[31] Abdelsalam, M. E.; Bartlett, P. N.; Baumberg, J. J.; Cintra, S.; Kelf, T. A.; Russell, A. E. Electrochemical SERS at a Structured Gold Surface. *Electrochemistry Communications* **2005**, *7*, 740-744.

[32] Hulteen, J. C.; Treichel, D. A.; Smith, M. T.; Duval, M. L.; Jensen, T. R.; Van Duyne, R. P. Nanosphere Lithography: Size-Tunable Silver Nanoparticle and Surface Cluster Arrays. *J Phys Chem B* **1999**, *103*, 3854-3863.

[33] Hulteen, J. C.; Vanduyne, R. P. Nanosphere Lithography - a Materials General Fabrication Process for Periodic Particle Array Surfaces. *Journal of Vacuum Science & Technology A-Vacuum Surfaces and Films* **1995**, *13*, 1553-1558.

[34] Jensen, T. R.; Malinsky, M. D.; Haynes, C. L.; Van Duyne, R. P. Nanosphere Lithography: Tunable Localized Surface Plasmon Resonance Spectra of Silver Nanoparticles. *J Phys Chem B* **2000**, *104*, 10549-10556.

[35] Haynes, C. L.; Van Duyne, R. P. Plasmon-Sampled Surface-Enhanced Raman Excitation Spectroscopy. *J Phys Chem B* **2003**, *107*, 7426-7433.

[36] Farcau, C.; Astilean, S. Mapping the SERS Efficiency and Hot-Spots Localization on Gold Film Over Nanospheres Substrates. *Journal of Physical Chemistry C* **2010**, *114*, 11717-11722.

[37] Greeneltch, N. G.; Blaber, M. G.; Schatz, G. C.; Van Duyne, R. P. Plasmon-Sampled Surface-Enhanced Raman Excitation Spectroscopy on Silver Immobilized Nanorod Assemblies and Optimization for Near Infrared (Lambda(Ex)=1064 Nm) Studies. *Journal of Physical Chemistry C* **2013**, *117*, 2554-2558.

[38] Chung, A. J.; Huh, Y. S.; Erickson, D. Large Area Flexible SERS Active Substrates using Engineered Nanostructures. *Nanoscale* **2011**, *3*, 2903-2908.

[39] Yao, J. L.; Tang, J.; Wu, D. Y.; Sun, D. M.; Xue, K. H.; Ren, B.; Mao, B. W.; Tian, Z. Q. Surface Enhanced Raman Scattering from Transition Metal Nano-Wire Array and the Theoretical Consideration. *Surf. Sci.* **2002**, *514*, 108-116.

[40] Zhang, J.; Shen, S.; Dong, X. X.; Chen, L. S. Low-Cost Fabrication of Large Area Sub-Wavelength Anti-Reflective Structures on Polymer Film using a Soft PUA Mold. *Optics Express* **2014**, *22*, 1842-1851.

[41] Xu, Z.; Chen, Y.; Gartia, M. R.; Jiang, J.; Liu, G. L. Surface Plasmon Enhanced Broadband Spectrophotometry on Black Silver Substrates. *Appl. Phys. Lett.* **2011**, *98*, 241904.

[42] Liu, Y. J.; Chu, H. Y.; Zhao, Y. P. Silver Nanorod Array Substrates Fabricated by Oblique Angle Deposition: Morphological, Optical, and SERS Characterizations. *Journal of Physical Chemistry C* **2010**, *114*, 8176-8183.

[43] Lee, S.; Hahm, M. G.; Vajtai, R.; Hashim, D. P.; Thurakitseree, T.; Chipara, A. C.; Ajayan, P. M.; Hafner, J. H. Utilizing 3D SERS Active Volumes in Aligned Carbon Nanotube Scaffold Substrates. *Adv Mater* **2012**, *24*, 5261-5266.

[44] Batista, E. A.; dos Santos, D. P.; Andrade, G. F. S.; Sant'Ana, A. C.; Brolo, A. G.; Temperini, M. L. A. Using Polycarbonate Membranes as Templates for the Preparation of Au Nanostructures

for Surface-Enhanced Raman Scattering. *Journal of Nanoscience and Nanotechnology* **2009**, *9*, 3233-3238.

[45] Panarin, A. Y.; Terekhov, S. N.; Kholostov, K. I.; Bondarenko, V. P. SERS-Active Substrates Based on n-Type Porous Silicon. *Appl. Surf. Sci.* **2010**,*256*, 6969-6976.

[46] Perney, N. M. B.; Baumberg, J. J.; Zoorob, M. E.; Charlton, M. D. B.; Mahnkopf, S.; Netti, C. M. Tuning Localized Plasmons in Nanostructured Substrates for Surface- Enhanced Raman Scattering. *Optics Express* **2006**, *14*, 847-857.

CHAPTER 3 WAFER-SCALE BACKPLANE ASSISTED RESONATING NANOANTENNA ARRAY (BARNA) SERS SUBSTRATE BY THERMAL DEWETTING TECHNIQUE

3.1. Introduction

In this chapter a deterministic process based on thermal dewetting technique will be demonstrated for fabricating large-area and low-cost plasmonic substrate for ultra-sensitive SERS sensing application, and the correlation between the plasmonic enhancement and tunable parameters of the process will be discussed in detail [1]. It is shown that plasmonic resonance frequency and intensity can be easily tuned by modulating morphology of metal nanoparticles, appearance of nanostructure and backplane assisted coupling effect in this process.

The overview of plasmonic effects and their dependences is shown in figure 3.1. The significant enhancement is due to the novel backplane assisted resonating nanoantenna array (BARNA) design, in which a metal backplane underlies a metallic nanoparticle array supported by silicon nanostructures. The enhanced lateral coupling and increased hot spot region have shown it to be advantageous for improving the scattered field of the Raman signal. The optimized plasmonic device for SERS is identified through numerical analysis and validated experimentally. The high SERS enhancement factor ($> 1.38\times10^{8}$) is demonstrated in the detection of nitrate ions, vitamin molecules and sensitive identification of DNA molecules.

3.2. Material and methods

3.2.1. Thermal dewetting technique

In recent years thermal dewetting technique has began to reveal its potential for low-cost nanostructure fabrication. The concept of combination of top-down and bottom-up techniques

offers an efficient way to create a nanostructured surface. Thermal dewetting is based on the spinodal phenomenon on metal thin film [2-4] and is illustrated in figure 3.2. With thermal energy injection, the metal generates fluctuation on the surface and conducts a bicontinuous sinusoidal pattern (figure 3.2 (a)). When the minimum thickness of fluctuation is within the unstable range (i.e. $\partial^2(\Delta G)/\partial h^2 < 0$ where ΔG is the total excess intermolecular interaction free energy per unit area and h is the film thickness, shown in figure 3.2 (e)), thermally induced perturbation will be amplified by dispersion force (figure 3.2 (b) and (c)) and lead to ruptured surface, then forming a semi-random metallic isolated nanostructure pattern (figure 3.2 (d)).

The ability to form a large-area metallic nanoparticle array using thermal dewetting technique has been exploited to fabricate SERS substrate. However, the planar substrate with single plasmonic layer made by this method provided only modest enhancement factor of about 10^6 [5]. Oh and Jeong demonstrated high SERS enhancement by applying thermal dewetted metallic particle pattern as mask to fabricate SiO_2 nanostructures [6]. After glanced angle deposition, the AgNPs can be deposited on the top and sidewall of nanostructures. They achieved enhancement factor of the order of 10^7 experimentally due to the 3D dielectric structure with higher density of both top and sidewall AgNPs. However, the optical characteristic of this substrate is not fully discussed and the underlying mechanism of the difference between planar and nanostructured thermal dewetting substrate is not clear so far. These questions will be discussed both experimentally and numerically in the following sections.

3.2.2. Nanofabrication process

The substrate used here is 4" single crystalline p-type doped silicon wafer. The crystalline orientation is <1,0,0> and the resistivity is 0.2 to 0.5 Ω/cm. All the substrates were cleaned with

acetone, isopropyl alcohol and DI water before any further fabrication steps. Then different thicknesses of gold thin film (5, 7.5 and 10 nm) were deposited on the substrate by Temescal six pocket electron-beam evaporation systems for thermal dewetting process.

In order to perform thermal dewetting, rapid thermal process (RTP) system Jipelec rapid thermal processor was applied for injecting thermal energy to gold thin film and inducing thermal disturbance. The RTP system significantly reduces the heating time and enables the process to be finished within 5 minutes. The chamber was purged with nitrogen gas to prevent any oxidation during the whole process. The dewetting temperature varied from 100 °C to 500 °C for 90 seconds.

After thermal dewetting process, the nanostructure pattern was transferred by dry etching technique. In this step, inductively coupled plasma reactive ion etching (ICP-RIE) STS advanced silicon etcher was used. A high aspect ratio structure can be achieved by continuously applying etching and passivation processes. SF_6 and O_2 were used for the etching phase and C_4F_8 was used for passivation. The pressure was set to 100 mTorr and the RF powers of inductive and capacitive chamber were set to be 600W and 12W respectively. To further improve the field enhancement, metal nanoparticles were removed by placing the sample into a gold etcher for 5 minutes and then silver was deposited by CHA SEC-600 electron-beam evaporator system. The power of the electron beam was 10 kV and the operating pressure was around 10^{-7} Torr. The evaporation rate was set to 0.5 Å/s to ensure uniformity of the silver layer. The deposited thicknesses were varied from 20 to 140 nm in order to find optimal SERS performance.

3.2.3. Reflectance measurement

In order to understand plasmonic properties and light trapping phenomenon of this device, optical reflectance was measured by Varion Cary 5G UV-VIS-NIR spectrophotometer. Integrated

sphere was used to collect all scattered light to ensure the data accuracy and the measured wavelength range was from 300 to 1100 nm.

3.2.4. SERS measurement

Renishaw PL/Raman micro spectroscope system was used for Raman spectra measurement. 20X objective lens was used for focusing and collecting incident laser and Raman signals. The wavelengths of excitation light source were 633 nm and 785 nm and acquisition time was set to 10 s. The laser intensity was reduced to 10 % for 633 nm and 0.5 % for 785 nm of maximum intensities in order to prevent saturation of the detector. The measured wavenumber range was from 700 to 1100 cm^{-1}.

3.2.5. Numerical simulation

The electric field distribution and reflectance of the electromagnetic field through the nanostructured substrates were studied by using the three-dimensional finite-difference time-domain (3D-FDTD) method and implemented by FDTD software from Lumerical Solutions, Inc. The transverse magnetic (TM) polarized electromagnetic wave was set to propagate normal to the substrate for both diffuse reflectance simulation and plasmonic enhancement simulation. The boundary conditions for x and y directions were periodic to calculate the inter-particle effect in periodic arrays of nanostructures and the maximum mesh size around the metal particles was 1.5 nm.

3.3. Results and discussion

3.3.1. Tunability of metallic nanoparticle pattern by thermal dewetting technique

Nanostructure tunability in our fabrication process is demonstrated in figure 3.3: (1) Nanoparticle size: Based on the spinodal dewetting theory, the size of the metal particle can be

tailored by varying the thickness of gold thin film layer. [7] In figure 3.3 (a) to (c), SEM images show the size of metallic particles with different thicknesses of gold layer (5, 7.5 and 10 nm) after applying thermal annealing. The corresponding distributions of particle size are shown in figure 3.3 (d) to (f). The result indicates that the thicker the metal layer, the larger the metallic nanoparticles that can be formed. The statistics have shown good agreement with theory and also proved that the size of metal nanoparticles can be controlled by the thickness of deposition. (2) Nanoparticle shape: In figure 3.3 (g) to (i) the shape of metal particle varies with different thermal dewetting temperatures at 100 °C, 300 °C and 500 °C respectively with continuous nitrogen purging. As the temperature increases, the AuNPs become more spherical in shape from increasing height and decreasing width of particle. (3) Nanorod height: Figure 3.3 (j) to (l) show that different heights of silicon nanorod can be made under different etching conditions or etching time durations. Hence the shape and diameter of the AuNPs as well as the height of the silicon nanorod can be tuned to achieve the desired design of 3D nanostructured device.

3.3.2. Optical characterization of thermal dewetted AuNPs

In order to optimize the design of the plasmonic substrate for SERS applications with all the controllabilities discussed above, it is necessary to understand the influences of all tunable parameters on its plasmonic property. Figure 3.4 (a) shows the diffuse reflectance spectra of AuNPs made with thermal dewetting for two different metal thin film thicknesses, 5 and 10 nm. As shown in figure 3.2, the particle size becomes larger when the deposited metal layer increases. The main difference between the two cases is the reflectance peak associated with the coupled localized surface plasmon resonance (LSPR) red-shifts from 560 nm to 700 nm when the dewetting thickness varies from 5 nm to 10 nm. In addition the coupled LSPR peak becomes broader when the thicker metal layer is applied. The reason for the broadening is that the variation of particle

size is larger with thicker metal layer (as shown in figure 3.3). From FDTD simulation in figure 3.4 (b) we can observe the same tendency with particle sizes of 30 nm and 70 nm. As a result, the LSPR peak can be tuned by controlling different metal thicknesses in order to fit the excitation laser wavelength. The insets show the electric field at 633 nm excitation in both cases and it indicates that the 5 nm metal film is more appropriate at certain wavelength applied where the resonance peak is closer to the excitation wavelength.

The dewetting temperature dependence is shown in figure 3.4 (c). The diffuse reflectance was measured for samples with different dewetting temperatures at 100 °C and 500 °C respectively. It can be inferred from SEM images in figure 3.3 that as we increase the dewetting temperature, the shape of the metal particle becomes more spherical. This shape difference provides different plasmonic resonance modes inside the AuNPs due to different damping attenuations. This phenomenon is verified in the FDTD simulation in figure 3.4 (d). The insets are the electric field distribution at 633 nm wavelength for the two different dewetting temperature cases and it suggests that higher electric field and lower damping loss can be achieved in more spherical nanoparticles produced by applying higher dewetting temperature.

Finally, after performing silicon etching process and forming nanostructured AuNPs substrate, figure 3.4 (e) shows the diffuse reflectance measurements with various silicon etching depths of 0nm, 100 nm and 500 nm, respectively. Broadband antireflection effect can be observed when silicon nanorods appear. This is because of the light-trapping phenomenon where photons have higher probability to be eventually absorbed by the nanostructures. This phenomenon can also be found in the FDTD simulation shown in figure 3.4 (f). The insets show the higher electric field enhancement due to light-trapping. In summary, all the geometrical properties can affect

plasmon resonance of the device including the transition of plasmonic mode or modifying the coupling efficiency.

3.3.3. SERS optimization of BARNA plasmonic substrate

In order to achieve higher enhancement, proper nanostructured plasmonic structure design with highly packed "hot spots" is necessary for the SERS substrate as discussed in previous chapter. FDTD simulation in figure 3.5 (a) shows the differences in the electric field distribution with different sizes of AgNPs where the periodicity of nanorods stays the same. It can be observed that the enhancement becomes largest when the AgNPs are separated with ultra-small gaps. Besides that, by placing an additional metal layer around the bottom of the silicon nanorod, a backplane metal layer can be created and helps to further enhance the Raman signal. The advantages of backplane are (1) reflecting the back-scattered field instead of being absorbed by silicon; (2) providing additional hotspot regions around the silicon nanorods and (3) creating a resonating cavity with metal nanoparticles and increasing the lateral coupling field (illustrated in figure 3.5 (b)). Those advantages can be observed by comparison with FDTD simulations in figure 3.4 (c), and the resonating effect was also observed by other researchers with similar configurations [8-9]. The BARNA substrate can be achieved by the following processes: after nanostrcutured AuNPs substrate was fabricated, the top gold layer was removed from the silicon nanorods and a new silver layer was deposited on the nanostructured silicon surface. From the SEM images in figure 3.5 (d), we can clearly observe that silver is deposited at two different levels and the backplane is located at the bottom of silicon nanorods.

Figure 3.6 shows the optimization of the BARNA substrate. Firstly, different thicknesses of silver (20, 50, 80 and 140 nm) were deposited on the nanostructured substrate with the nanorod height of 100 nm. The average SERS intensity with 633 nm excitation wavelength was measured

and shown in figure 3.6 (a). The highest SERS enhancement was obtained from the substrate with 50 nm silver thickness. Secondly, samples with different structure heights (100, 500 and 1000 nm) were deposited with 50 nm silver layer and SERS intensity was measured on each substrate as shown in figure 3.6 (b). Clearly, the substrate with nanorod height of 100 nm provides the highest enhancement. The reason should be that the plasmonic coupling only happens when two metal-dielectric interfaces are close enough to each other [9]. Besides that, we also found that this optimized design (50 nm silver deposition and 100 nm pillar height) has better SERS enhancement with excitation wavelength at 633 nm than 785 nm as figure 3.6 (c) shows. From figure 3.6 (d), the FDTD simulations with different excitation wavelengths imply that 633 nm has better resonance both in lateral coupling of top AgNPs and metal backplane around the silicon nanorods.

Different concentrations of rhodamine 6G (R6G, from 100 μM to 10 nM) have been unambiguously detected with the optimized BARNA substrate (50 nm silver deposition and 100 nm pillar height) and are shown in figure 3.7 (a). Low concentration such as 10 nM can be routinely detected, which reflects the significantly high enhancement factor achievable by this design. An average enhancement factor of 1.38×10^8 uniformly across the wafer surface was obtained using the optimized BARNA device.

3.3.4. SERS detection of chemical and biomolecules using the optimized substrate

The optimized BARNA substrate has been utilized to detect several biologically and environmentally relevant chemicals and ions as shown here. For example, nitrate (NO_3^-) ion is a stable form of nitrogen and commonly found in environmental water such as streams, rivers or lakes. Since fertilizers used in agriculture usually contain nitrogen compounds, the concentration of nitrate in water will be significantly different according to agricultural activities. The more fertilizers used, the more nitrate will be dissolved into water, hence increasing the concentration

of nitrate in the environmental water. By sensing nitrate concentration in water in a field, the amount of fertilizer can be controlled depending on weather and soil conditions. Also, nitrate is directly related to environmental pollution and human health [10]. Figure 3.7 (b) shows that the Raman peak intensity of nitrate changes with different nitrate concentrations (50, 25 and 10 μM) [11]. It shows this substrate can detect much lower nitrate concentration than U.S. Environmental Protection Agency (EPA) maximum allowance of 10 ppm or 0.7 mM.

Next, more complicated chemicals such as B-group vitamins were detected on the optimized SERS substrate. B-group vitamins such as Riboflavin and Thiamine are significant elements in cell metabolism as cofactors of some key enzymes. The detection of such vitamins in body fluids has tremendous potential in pharmacokinetics. According to previous research, the concentrations of these two vitamins in human blood are at 100 nM range [12]. Figure 3.7 (c) shows the SERS spectrum of both 100 nM Riboflavin and Thiamine solutions. The peak positions in both vitamins have good agreement to the reported data in previous literatures [13-14]. In addition, nucleic acid such as DNA has been detected as shown in figure 3.7 (d). Here we use two different kinds of single stranded DNA: 5'-thiolCAGCAAATGGGCTCCGAC-3' and 3'-GTCGGAGCCCATTTGCTG-5'-HEX at a concentration of 1 nM. SERS spectra of both DNAs have their own distinctive peaks and some of them (such as peaks at 1298, 1400, 1502, 1532 and 1623 cm^{-1}) are identical to Raman peaks of nucleic acid bases themselves reported in previous literature [15-16]. It demonstrates the ability of the optimized BARNA substrate to detect and distinguish low concentrations of DNA.

3.4. Conclusion

Controllability and flexibility of thermal dewetting technique to fabricate plasmonic device's for SERS application is demonstrated. The correlations between plasmonic phenomena and corresponding tunable geometric parameters are thoroughly discussed based on optical characteristics and FDTD simulations. We demonstrate that the size, shape and appearance of the supported nanostructure can affect the plasmonic property significantly. With thicker deposited Au layer, the thermal dewetted AuNPs become larger and cause red-shift in LSPR mode. Higher dewetting temperature provides more thermal energy to form spherical AuNPs which hold LSPR better. Nanostructured substrate induces light-trapping near the surface and enhances near electric field. With the optimal backplane assisted resonating nanoantenna array (BARNA) substrate, the EF of 1.38×10^8 can be achieved due to the high density of hot spots and enhanced scattering field from the metal backplane assistance. Finally, biological chemicals with different structural complexities including nitrate, vitamins, and DNAs are detected with the optimized BARNA substrate to demonstrate the capability for general biological sensing applications. The study shows the potential that more complicated biological and chemical analysis such as kinetic analysis of DNA hybridization can be realized on this low-cost and high-sensitivity BARNA SERS substrate.

3.5. Figures

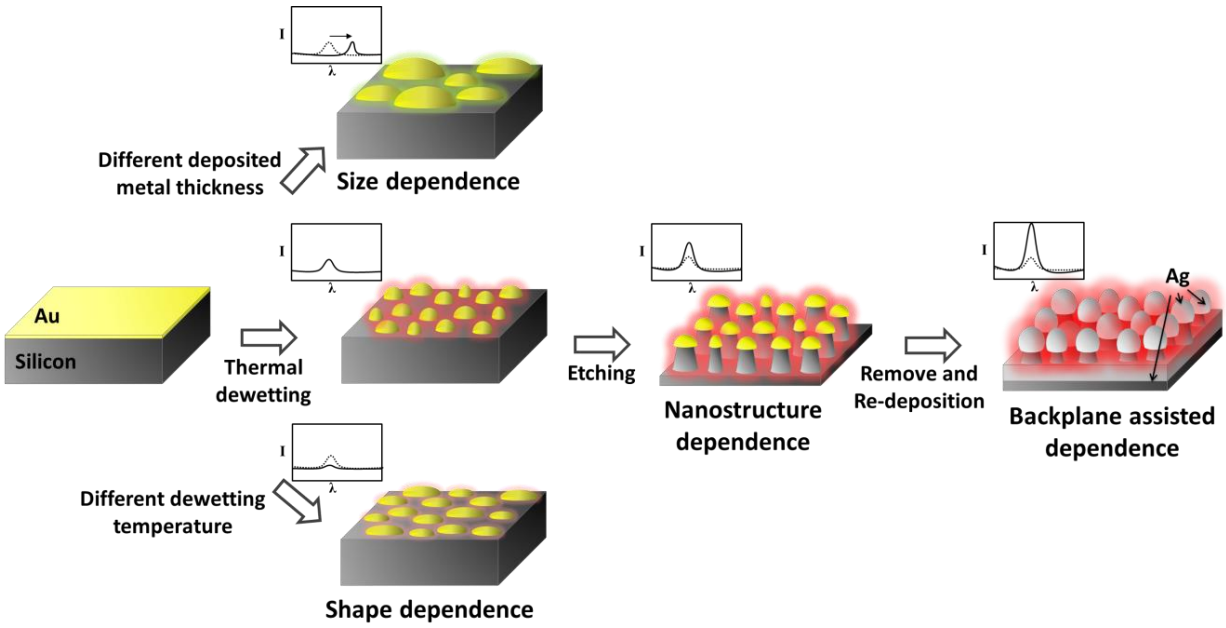

Figure 3.1 Overview of plasmonic enhancement with different process dependences including morphology of metal nanoparticle, appearance of nanostructure and backplane assisted effect.

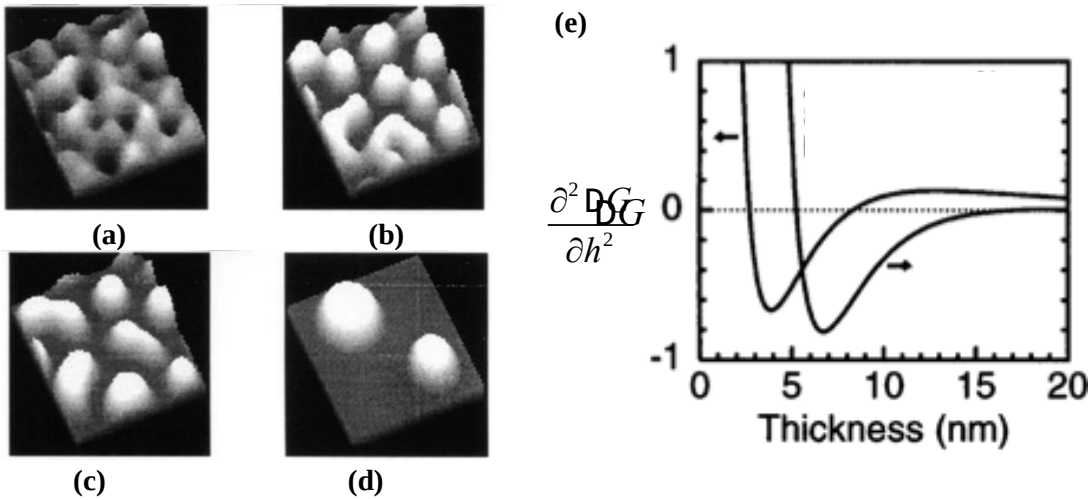

Figure 3.2 (a) to (d): Evolution of spinodal dewetting pattern. (e) Variation of excess intermolecular free energy per unit area (ΔG) and force per unit volume ($\partial^2(\Delta G)/\partial h^2$) with film thickness.

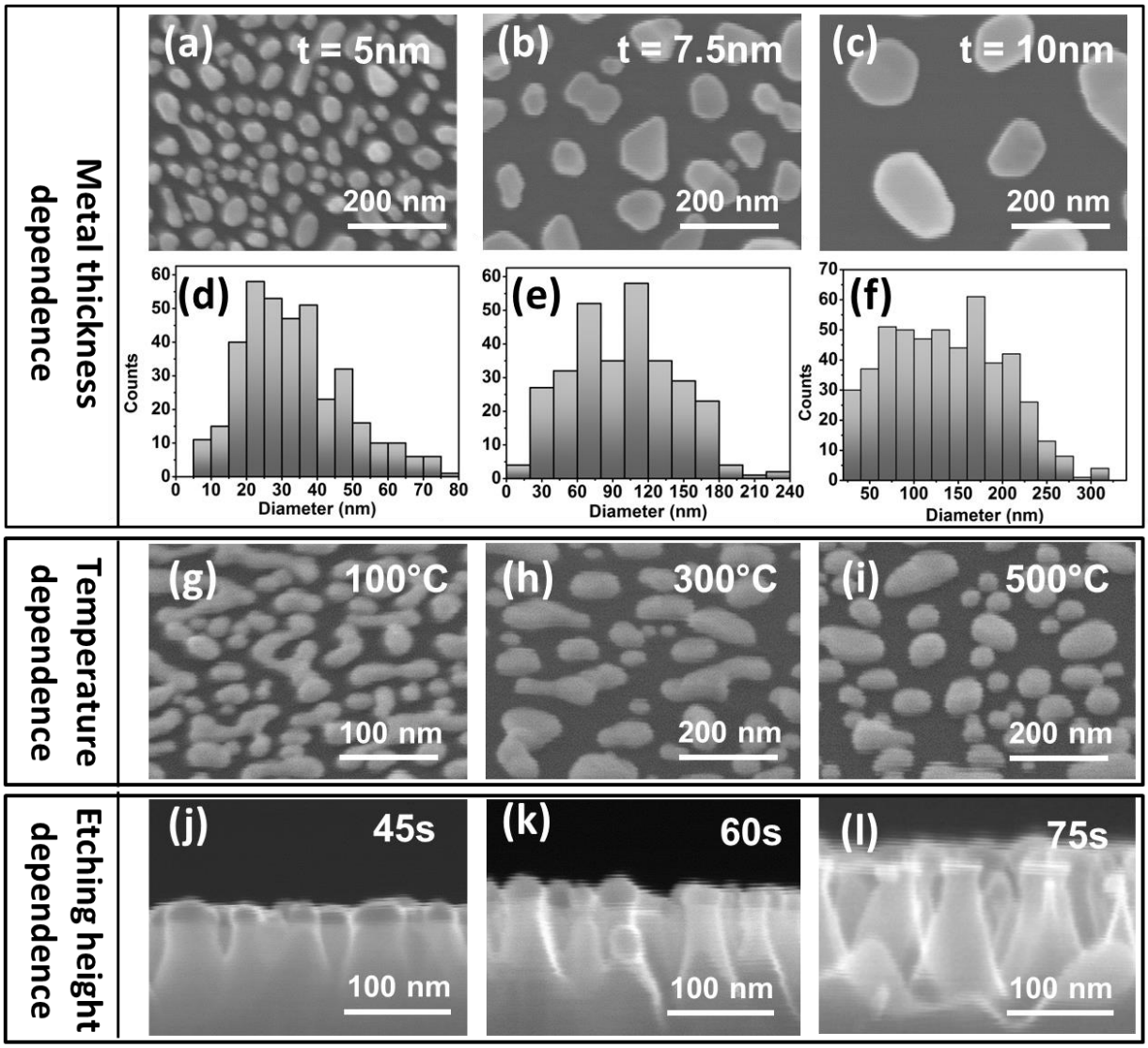

Figure 3.3 Controllability of different geometrical parameters. (a) to (c): SEM images of metal nanoparticle transformed from gold thin film with different thicknesses (t = 5, 7.5 and 10 nm). (d) to (e): The corresponding statistic distribution of metal nanoparticle size in (a) to (c). (g) to (i): SEM images of metal nanoparticle with different thermal dewetting temperatures (temperature = 100, 300 and 500 °C). (j) to (l): cross section SEM images of nanostructured substrate with different etching conditions.

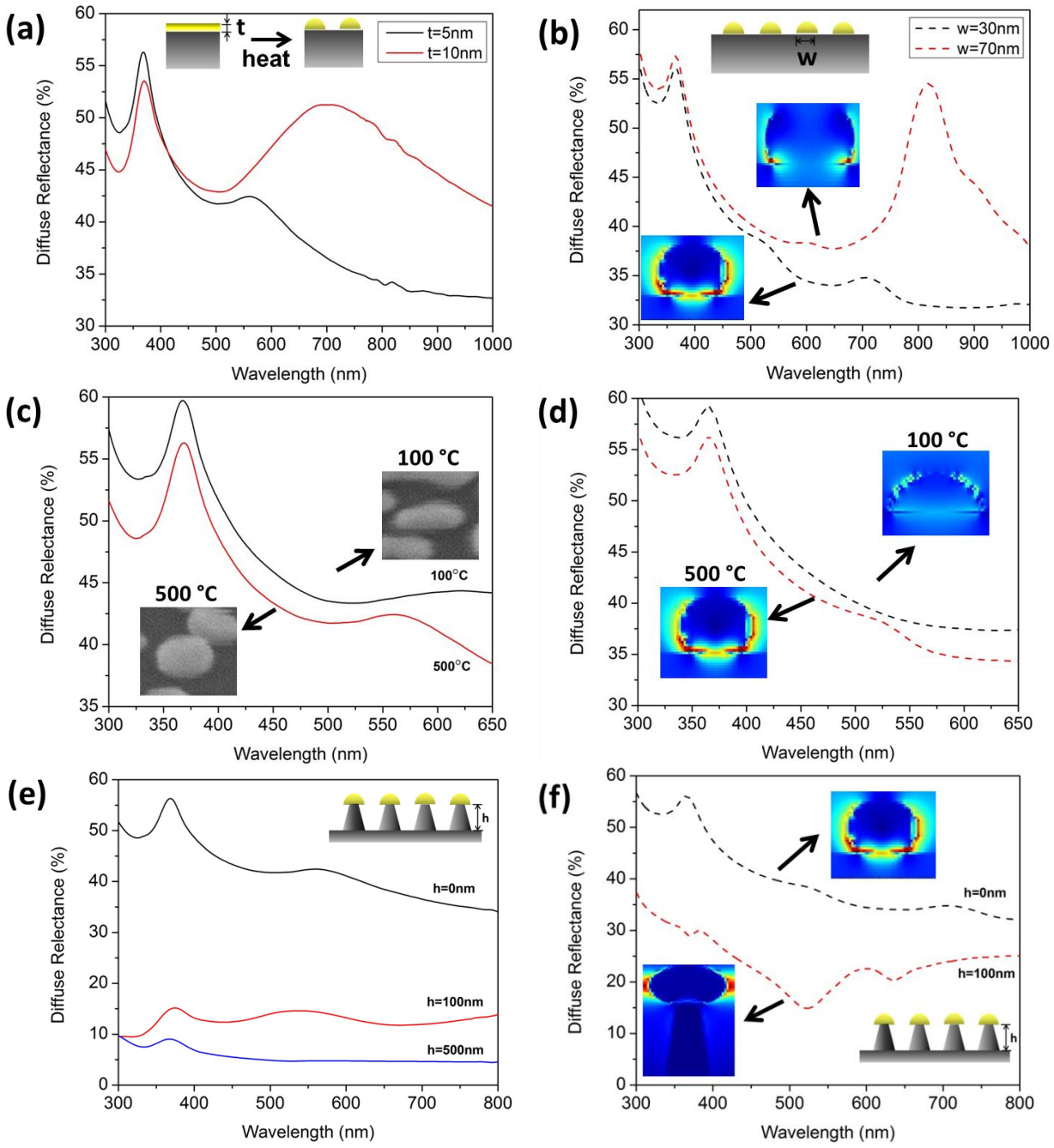

Figure 3.4 Optical characteristic by individually varying different geometrical parameters: (a) Experimental and (b) numerical diffuse reflectance spectrum of different AuNPs sizes by changing deposited thickness. (c) Experimental and (d): numerical reflectance spectrum of different AuNPs shapes by applying different thermal dewetting temperatures. (e) Experimental and (f): numerical reflectance spectrum of nanostructured AuNPs substrate with different nanorod heights.

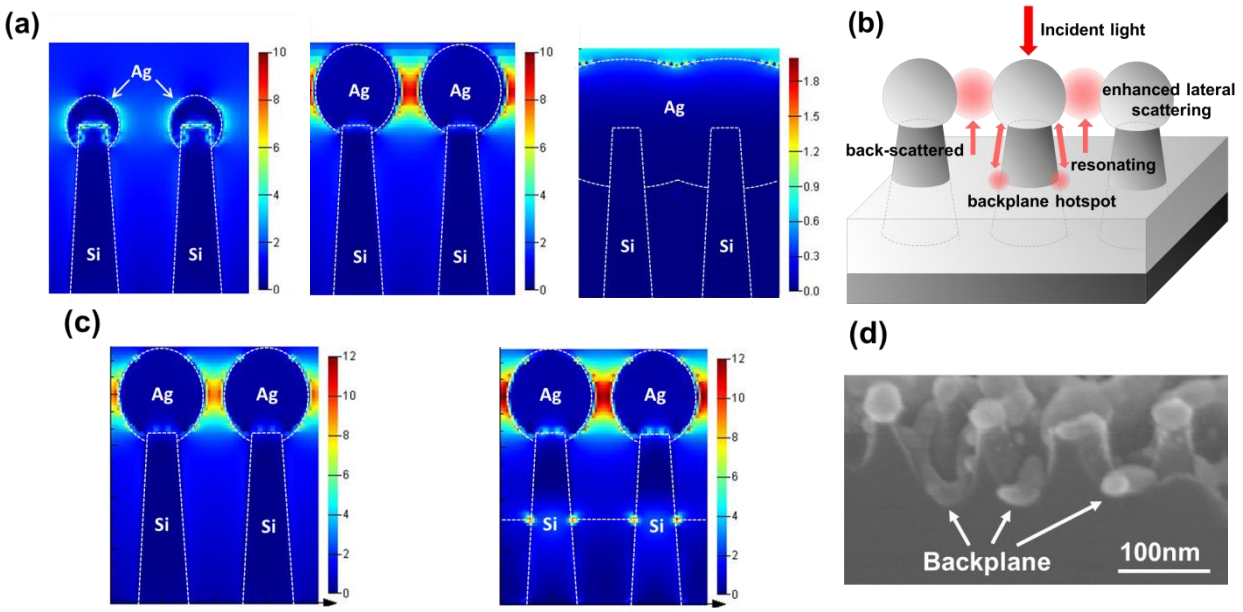

Figure 3.5 (a) FDTD simulations of electric field distribution with different sizes of metal nanoparticles on 3D AgNPs substrate. (b) Illustration of the enhanced scattering field assisted by metal backplane. (c) FDTD simulations of electric field distribution with and without metal backplane on 3D AgNPs substrate. (d) Cross section SEM image of BARNA substrate. The excitation wavelength of all FDTD simulations above is operated at 633 nm.

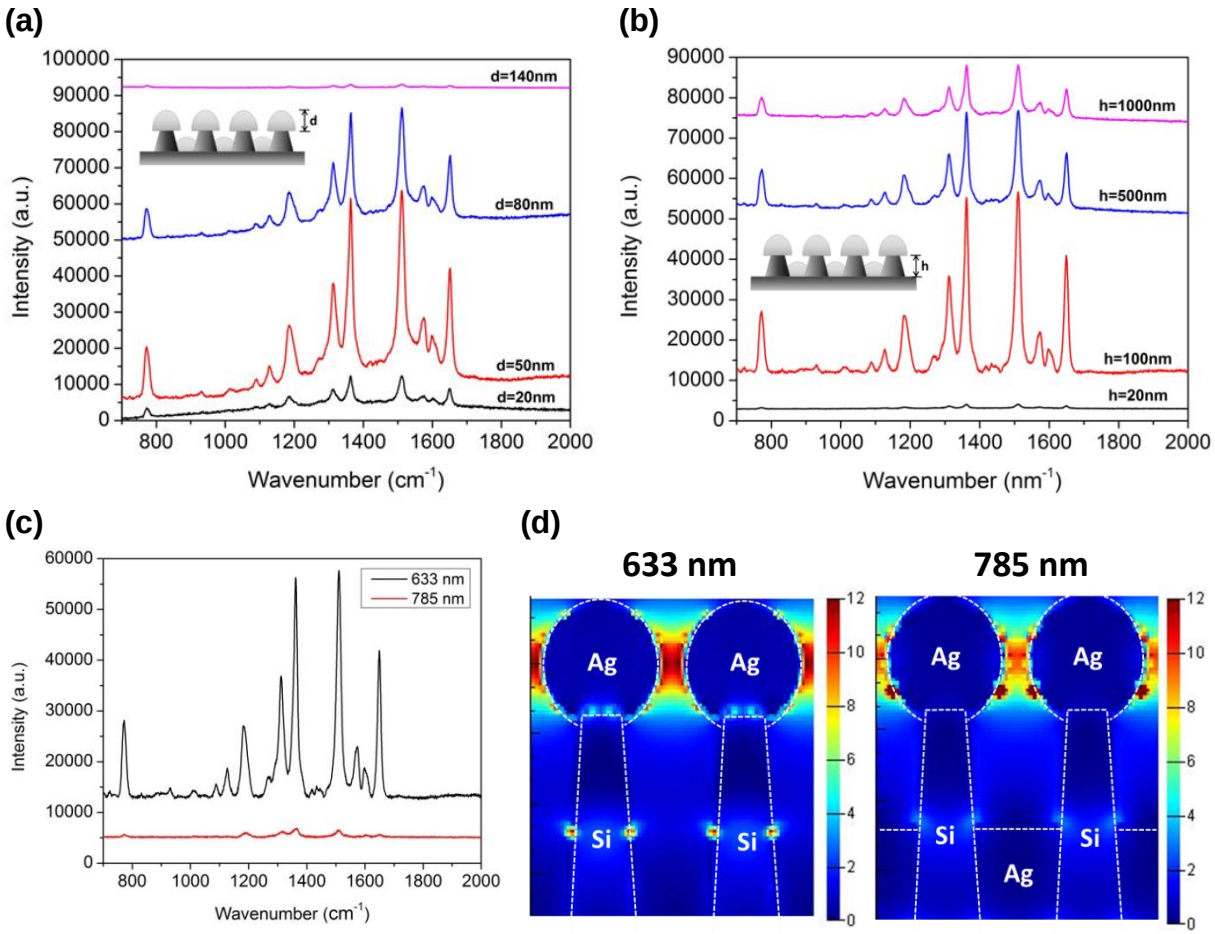

Figure 3.6 (a) SERS spectrum of 100 µM R6G on BARNA substrate with different Ag deposited thickness (d=20, 50, 80 and 140 nm). (b) SERS spectrum of 100 µM R6G on BARNA substrate with different etching heights (h=20, 100, 500 and 1000 nm). (c) SERS spectrum of 100 µM R6G on optimized BARNA substrate (50 nm silver deposition and 100 nm pillar height) with different excitation wavelengths (633 and 785 nm). Power of both laser sources is tuned to be the same. (d) FDTD simulation of electric field distribution with different excitation wavelengths on BARNA substrate.

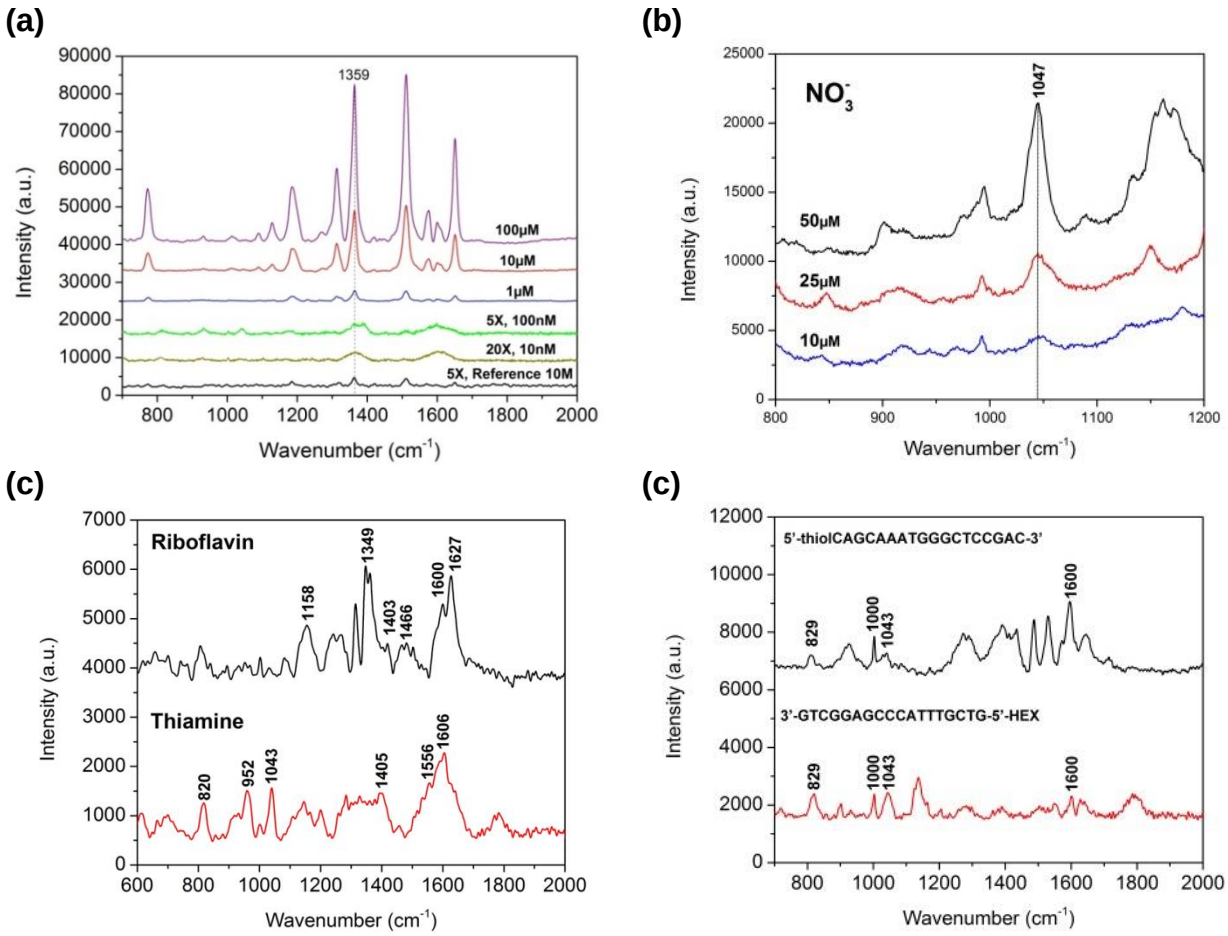

Figure 3.7 SERS spectrum of (a) different concentrations of R6G (from 100μM to 10nM). (b) different concentrations of nitrate (10. 25 and 50 μM); (c) 100 nM Riboflavin and Thiamine; and (d) 2 single stranded DNA: 5'-thiolCAGCAAATGGGCTCCGAC-3' and 3'-GTCGGAGCCCATTTGCTG-5'-HEX with 1 nM with BARNA substrate applied. All spectra are obtained by averaging three different times of measurement.

3.6. References

[1] Chang, T.; Gartia, M. R.; Seo, S.; Hsiao, A.; Liu, G. L. A Wafer-Scale Backplane-Assisted Resonating Nanoantenna Array SERS Device Created by Tunable Thermal Dewetting Nanofabrication. *Nanotechnology* **2014**, *25*, 145304.

[2] Bischof, J.; Scherer, D.; Herminghaus, S.; Leiderer, P. Dewetting Modes of Thin Metallic Films: Nucleation of Holes and Spinodal Dewetting. *Phys. Rev. Lett.* **1996**, *77*, 1536-1539.

[3] Sharma, A.; Khanna, R. Pattern Formation in Unstable Thin Liquid Films. *Phys. Rev. Lett.* **1998**, *81*, 3463-3466.

[4] Seemann, R.; Herminghaus, S.; Jacobs, K. Dewetting Patterns and Molecular Forces: A Reconciliation. *Phys. Rev. Lett.* **2001**, *86*, 5534-5537.

[5] Liao, T.; Lee, B.; Lee, C.; Wei, P. Large-Area Raman Enhancement Substrates using Spontaneous Dewetting of Gold Films and Silver Nanoparticles Deposition. *Sensors and Actuators B-Chemical* **2011**, *156*, 245-250.

[6] Oh, Y.; Jeong, K. Glass Nanopillar Arrays with Nanogap-Rich Silver Nanoislands for Highly Intense Surface Enhanced Raman Scattering. *Adv Mater***2012**, *24*, 2234-2237.

[7] Sharma, A.; Khanna, R. Pattern Formation in Unstable Thin Liquid Films. *Phys. Rev. Lett.* **1998**, *81*, 3463-3466.

[8] Li, W.; Ding, F.; Hu, J.; Chou, S. Y. Three-Dimensional Cavity Nanoantenna Coupled Plasmonic Nanodots for Ultrahigh and Uniform Surface-Enhanced Raman Scattering Over Large Area. *Optics Express* **2011**, *19*, 3925-3936.

[9] Wang, S.; Pile, D. F. P.; Sun, C.; Zhang, X. Nanopin Plasmonic Resonator Array and its Optical Properties. *Nano Letters* **2007**, *7*, 1076-1080.

[10] Gartia, M. R.; Braunschweig, B.; Chang, T.; Moinzadeh, P.; Minsker, B. S.; Agha, G.; Wieckowski, A.; Keefer, L. L.; Liu, G. L. The Microelectronic Wireless Nitrate Sensor Network for Environmental Water Monitoring. *Journal of Environmental Monitoring* **2012**, *14*, 3068-3075.

[11] Mosier-Boss, P. A.; Lieberman, S. H. Detection of Anions by Normal Raman Spectroscopy and Surface-Enhanced Raman Spectroscopy of Cationic-Coated Substrates. *Appl. Spectrosc.* **2003**, *57*, 1129-1137.

[12] Shils, M. E.; Shike, M.; Ross, A. C.; Caballero, B.; Cousins, R. J. Modern Nutrition in Health and Disease, tenth ed., Lippincott Williams & Wilkins: Philadelphia **2006**.

[13] Kokaislova, A.; Matejka, P. Surface-Enhanced Vibrational Spectroscopy of B Vitamins: What is the Effect of SERS-Active Metals used? *Analytical and Bioanalytical Chemistry* **2012**, *403*, 985-993.

[14] Leopold, N.; Cinta-Pinzaru, S.; Baia, M.; Antonescu, E.; Cozar, O.; Kiefer, W.; Popp, J. Raman and Surface-Enhanced Raman Study of Thiamine at Different pH Values. *Vibrational Spectroscopy* **2005**, *39*, 169-176.

[15] Kim, S. K.; Joo, T. H.; Suh, S. W.; Kim, M. S. Surface-Enhanced Raman-Scattering (SERS) of Nucleic-Acid Components in Silver Sol - Adenine Series. *J. Raman Spectrosc.* **1986**, *17*, 381-386.

[16] Koglin, E.; Sequaris, J. M.; Fritz, J. C.; Valenta, P. Surface Enhanced Raman-Scattering (SERS) of Nucleic-Acid Bases Adsorbed on Silver Colloids. *J. Mol. Struct.* **1984**, *114*, 219-223.

CHAPTER 4 COMPARISON OF SERS PERFORMANCE ON ABSORBING AND NON-ABSORBING NANOSTRUCTURED SUBSTRATE

4.1. Introduction

SERS devices have been thus far designed and fabricated by plenty of different methods. Among these methods different kinds of substrate materials such as silicon [1], III-V semiconductor [2], transparent conductive metal oxide [3], dielectric, [4] and polymer [5] have been demonstrated. In addition, previous studies have proved that LSPR is sensitive to the surrounding environment [6] and the metal thin film adhesion [7]. However, there is no study specifically on how different substrate materials affect SERS performance, even though the structure was fabricated by the same method.

In order to discuss the influence of substrate material on the Raman signal enhancement on SERS devices, nanostructured SERS devices were fabricated with the same process but on different substrate materials: silicon (Si) as light absorbing and silicon nitride (Si_3N_4) as non-absorbing material. These two materials are widely used in semiconductor fabrication processes. Optical properties of two nanostructured SERS devices fabricated by the thermal dewetting technique [8] are studied both experimentally and numerically to understand the effect of substrate material on SERS. Finally SERS measurements were conducted on both devices with two target analytes to show contrasting Raman enhancement between absorbing and non-absorbing substrate materials.

4.2. Materials and methods

4.2.1. Nanofabrication process

The schematic of processing steps for Si and Si_3N_4 nanostructured SERS devices is shown in figure 4.1. The base substrate is single crystalline p-type doped silicon wafer with crystalline orientation of <1,0,0> and resistivity of 0.2 to 0.5 Ω/cm. Before performing any treatment, the substrate was thoroughly cleaned with acetone, isopropyl alcohol and DI water to ensure no impurities or dust remain on the wafer surface. After cleaning, a thin layer of 300 nm Si_3N_4 was deposited by plasma enhanced chemical vapor deposition (PECVD) with N_2, SiH_4 and NH_3 as figure 4.1 (a) shows. Here STS plasma enhanced chemical vapor deposition system was utilized and operated with mixed RF frequency in order to reduce surface tension during thin film deposition. The deposition rate was 143 Å/min. The temperature of platen and showerhead were controlled at 300 °C and 240 °C respectively with tolerance of 20 °C. Operating pressure was 650 mTorr and RF power of both inductive and capacitive chambers were both 20 W. Then 10 nm Ag was deposited on substrates with and without Si_3N_4 by CHA SEC-600 electron-beam evaporator system as shown in figure 4.1 (b). The power of the electron beam was set as 10 kV and operating base pressure was around 10^{-7} Torr. The deposition rate was controlled at 1 Å/s to ensure surface uniformity.

Thermal dewetting technique was performed to generate self-assembled AgNPs pattern on both Si and Si_3N_4 as shown in figure 4.1 (c). Here Jipelec rapid thermal processor was applied to inject thermal fluctuation into the Ag thin film. The annealing was conducted for 10 min at 500 °C. After obtaining AgNPs, the pattern was transferred onto both substrates by inductively coupled plasma reactive ion etching (ICP-RIE) as shown in figure 4.1 (d). Bosch process was used by the

STS advanced silicon etcher in order to keep the fidelity of transferred nanostructures. SF_6 and O_2 were used as etching gases and C_4F_8 was used for passivation. The operating pressure was set at 100 mTorr and the RF power of the capacitive chamber was 12 W. The RF power of the inductive chamber was set as 350 W and 600 W for etching Si and Si_3N_4 respectively. Finally in figure 4.1 (e) the AgNPs were removed by silver etchant by immersing devices for 5 minutes and then another thicker layer of 80 nm Ag was deposited on nanostructured substrates as shown in figure 4.1 (f). The equipment and recipe of the second deposition were the same as those described before for thermal dewetting process of fabricating AgNPs.

4.2.2. Optical measurement

The spectral reflectance spectra were measured by a micro-spectroscopy workstation in the Beckman Institute, University of Illinois at Urbana Champaign, which was built upon a Zeiss Axio observer D1 inverted microscope. The workstation is equipped with two halogen lamp illuminators and one Hg lamp as incident sources. A Zeiss AxioCam MRC color CD camera and optical silicon PDA spectrometer coupled to microscope via multi-mode fiber optics are installed in this system for image capturing and micro-spectroscopic characterization in UV-visible range (300 to 900 nm).

4.2.3. Raman spectroscopy measurement

Renishaw PL/Raman micro-spectroscope system was used in this chapter for Raman signal measurements. 633 nm He-Ne and 785 nm diode lasers are used as excitation light sources. 20X objective lens was used to focus/collect incident light and Raman signal onto/from the surface of nanostructured SERS devices. The range of measured wavenumber was from 200 to 2000 cm^{-1}. Every spectrum showed in this paper is the average value measured from five different spots.

4.2.4. FDTD simulation

The numerical simulations of optical characteristics were studied by using three-dimensional finite-difference time-domain (3D-FDTD) method with FDTD software package from Lumerical Solutions, Inc.. The x-axis polarized electromagnetic wave was set to propagate normal to the substrate (-z direction) for both reflectance and near field simulations. The boundary conditions for x and y directions were periodic to simulate the array effect of nanostructures. Perfected matching layer has been applied to the boundary conditions in z direction to eliminate any interference from the boundaries. The simulated nanostructure was positioned at the origin in x-y plane and the profile was modeled from the observation of SEM image. The near field simulation observed in this chapter is at x-z plane at y = 0. The mesh size was set as 1 nm^3 and the total FDTD simulation region was 160 nm× 160 nm× 900 nm.

4.3. Results and discussion

4.3.1. Morphology comparison between Si and Si_3N_4 nanostructured SERS substrates

Figure 4.2 (a) shows the images of scanning electron microscopy (SEM) on Si and Si_3N_4 after thermal dewetting is performed. Although the pattern of thermal dewetted AgNPs is semi-random, nanoparticles from both substrates have similar size and morphology. The diameter of AgNPs is around 100 nm, which agrees with theoretical results from other literature that the diameter of thermal dewetted nanoparticles should equal to the square of the deposited metal thickness [9]. Then the pattern was transferred onto substrates by dry etching and cross section SEM images are shown in figure 4.2 (b). The etching height was controlled at 250 nm for both substrates to have fair comparison.

In order to obtain higher Raman enhancement from nanostructured device, the thermal dewetted AgNPs were removed and a replacement layer of 80 nm Ag was deposited. One reason is that the surface of the original dewetted Ag nanoparticle was oxidized from the dry etching gas O_2, which degrades the surface enhancement property. Another reason for this is to increase the lateral dimension of the Ag nanoparticles. When a thicker layer of metal is deposited on the nanostructures, Ag deposited on the top of the nanostructure will not only grow vertically but will gradually increase its lateral dimension as well. It reduces the distances among these newly deposited AgNPs, which increases the inter-particle coupling effect. Lastly, the additional metal deposition allows further decrease in inter-particle distance on the sidewall of nanostructures, resulting enhanced Raman signal. Figure 4.2 shows the (c) top and (d) 30 degrees tilted view of SEM images for SERS devices after Ag deposition. From the images it can be observed that the morphology of top and sidewall AgNPs are similar in both cases to provide good SERS comparison of different substrate materials instead of structure morphology.

4.3.2. Optical characterization of Si and Si_3N_4 nanostructured SERS substrates

Here the spectral reflectance measurement was performed in order to understand optical characteristics of both nanostructured SERS devices. The measured spectral reflectance of Si and Si_3N_4 are shown in figure 4.3 (a). Due to the difference of the refractive index between Si and Si_3N_4, the LSPR modes on both spectra appear at slightly different positions on the spectra with around 10 nm shifts. Figure 4.3 (b) is the FDTD simulation of spectral reflectance with the configuration designed from SEM images. When comparing the measured and simulated results, although there are some shifts in wavelength and variations in intensity, both of them show similar optical characteristics despite the semi-random configuration of etched thermal dewetting pattern. It indicates that microscopically the SERS devices have similar optical property as the one with

periodic nanostructured devices. Therefore these models are applied to investigate near field properties on both SERS devices.

4.3.3. FDTD simulation

Figure 4.4 shows x-z plane electric field distribution of Si and Si_3N_4 nanostructured SERS devices at 633 and 785 nm excitation wavelengths, which are commonly used for Raman measurement analysis. At 633 nm the LSPR mode comes mainly from the strong coupling effect of top AgNPs on both nanostructured SERS devices. However, sidewall AgNPs of the nanostructured Si_3N_4 SERS device exhibit high coupling among them as well. On the other hand, when the excitation wavelength is 785 nm near none of the LSPR modes according to reflectance spectra, the electric fields on both devices are lower than the 633 nm case. To estimate the enhancement, we set the enhancement factor (EF) as $|E_{max}/E_{in}|^4$ where E_{max} is the maximum amplitude of electric field near the device and E_{in} is the amplitude of incident electric field. The calculated results of simulated EF and ratio between the two devices are listed in table 4.1. The overall EF with 633 nm excitation wavelength is higher than that at 785 nm, which agrees with the reflectance measurement showing the strong LSPR mode at 633 nm. It can also be observed that EF of Si_3N_4 nanostructured SERS device is higher than that of Si device in both excitation wavelengths. The reason is two-fold: this higher enhancement is from (1) the shifts of LSPR modes due to the different refractive index and (2) the absence of absorption in non-absorption material. This result indicates that Si_3N_4 as non-absorbing material retains higher electric field at both 633 and 785 nm.

4.3.4. SERS measurement

For experimental SERS ability measurement, rhodamine 6G (R6G, Sigma-Aldrich, 99%), a commonly used Raman analyte, was applied here to examine the difference between Si and Si_3N_4 substrate material. A 2 µL droplet of 10 µM R6G was dropped on both devices and waited overnight to evaporate the solvent (water) completely. The diameter of the dried R6G droplet was around 1.2 mm^2, which is much larger than the spot size of the laser. Therefore, the laser was focused at the center of the droplet where the uniform region of molecule distribution was observed in order to avoid the aggregation phenomenon at the edge of the droplet (coffee ring effect). The laser powers of 633 and 785 nm were adjusted to keep at the same level to have better comparison between two excitation wavelengths. The output power of 633 and 785 nm laser measured by power meter was 211 and 342 µW respectively. The acquisition time of all measurements with Si and Si_3N_4 nanostructured devices was kept at 10 secs. The results are shown in figure 4.5 (a) and (b). Although there are some relative amplitude differences among the spectra excited by two excitation wavelengths, all the spectra show the distinctive peaks at 771, 1184, 1312, 1363, 1512 and 1651 cm^{-1}. The peak of 1363 cm^{-1}, the aromatic C-C stretching vibration mode [10], was selected to quantitatively compare the SERS ability between two devices, and the ratios of Raman intensity are shown in table 4.2. The SERS enhancement of Si_3N_4 substrate is larger than that of the Si at both excitation wavelengths, and ratios of their peak Raman intensities are 2.5 at 633 nm and 4.21 at 785 nm, respectively.

In order to obtain the approximate experimental EF and more accurately estimate the enhancement ratio, self-assembled monolayer of trans-1,2-bis(4-pyridyl)ethylene (BPE, Sigma-Aldrich, 99%) was applied here. Firstly both of the devices were immersed in 5mM BPE ethanolic solution for 24 hours and then rinsed with pure ethanol solution to wash out extra BPE molecules

stacked on the monolayer. Finally devices were blown with nitrogen gas to completely dry. In addition, a commercially available SERS substrate (Klarite KLA-313, D3 Technologies Ltd., UK) was treated with the same process to form BPE monolayer as a direct comparison of Raman enhancement.

Figure 4.5 (c) and (d) show the Raman spectra of BPE monolayer on both nanostructured Si and Si_3N_4 devices. All spectra show characteristic Raman peaks of BPE at 1020, 1200, 1340, 1607 and 1637 cm^{-1}. The peak intensity of 1200 cm^{-1}, which corresponds to C = C stretching vibrational mode [11], was used here to estimate the performance of SERS ability in each device. The peak intensity ratio from BPE measurement between two devices is listed in table 4.2 and it can be observed that Si_3N_4 also induces higher SERS intensity by 3 to 4 times (depend on different excitation wavelengths) when compared to Si as R6G measurement shows. It further verifies that this phenomenon happens with various analyte molecules.

From the datasheet of Klarite SERS substrate, the EF of Klarite SERS substrate is at least 10^6 for binding molecules. As a result, the spectrum with Klarite substrate with 1.23 mW 633nm laser and 30 secs acquiring time was used as reference and the EF is assumed to be at least 10^6. The calculation of estimated EF is based on the following equation [12]:

$$EF = \frac{I_{SERS}}{I_{Klarite}} \times \frac{N_{Klarite}}{N_{SERS}} \times \frac{P_{Klarite}}{P_{SERS}} \times \frac{T_{Klarite}}{T_{SERS}}$$

where I_{SERS} and $I_{Klarite}$ are scattered intensities of Raman signal from SERS with nanostructured device and Klarite substrate. N_{SERS} and $N_{Klarite}$ are the number of molecules being probed on nanostructured device and Klarite substrate. P_{SERS} and $P_{Klarite}$ are the power intensity applied onto nanostructured device and Klarite substrate. T_{SERS} and $T_{Klarite}$ are the acquiring time when

measuring Raman signal on nanostructured device and Klarite substrate. Table 4.3 shows the results of estimated EF. The enhancement is larger with Si_3N_4 than the one with silicon by 3 to 4 times with both 633 and 785 nm excitation as we expected. Furthermore, the enhancement is higher with 633 nm excitation than the one with 785 nm. The results agree with the simulation data in terms of Raman intensity ratio and comparison between different excitation wavelengths.

The summary of all results from experiment and simulation is plotted in figure 4.6. As shown in the figure, the experimental EF is larger than estimated EF from FDTD simulation by 1 to 2 orders. The reasons are: (1) The electromagnetic enhancement is the only factor considered in FDTD simulation, which means carrier transfer mechanism is not included. (2) The pattern from thermal dewetting is semi-random and there is some variation in terms of the size of nanostructure and the gap among them. It means that there will be chances that the gap between top metal nanoparticles is smaller than what has been simulated here. Therefore higher coupling will be induced and it leads to higher enhancement. In addition, the sidewall metal nanoparticles from evaporation are not distributed exactly the same as in FDTD simulation where all nanoparticles are the same distance from each other. By the same argument, if there is smaller gap between sidewall nanoparticles than the one in simulation, the experimental EF should have been larger.

In order to verify that this difference between Si and Si_3N_4 is not due to the fabrication difference or semi-random property of thermal dewetted pattern, mapping of SERS spectrum with BPE monolayer has been conducted on both devices. The total mapping is on area of 100 μm^2 and measured at every 10 μm distance. Figure 4.7 shows the SERS mapping result. It indicates that the Raman signal enhancement of Si_3N_4 is uniformly higher than that of Si, which implies that the substrate material did influence the SERS ability.

4.4. Conclusion

In summary, nanostructured SERS devices with AgNPs were fabricated with both Si and Si_3N_4 by the same process based on thermal dewetting technique. From the SEM images, both devices showed similar morphology on either AgNPs or nanostructured substrate, which provided a fair comparison for discussing how substrate material affects the SERS performance. Measured and simulated spectral reflectance spectra indicate that both devices support LSPR modes at similar wavelengths in the visible spectrum and can be predicted by FDTD simulation of periodic nanostructures. From near field FDTD simulation it was found that Si_3N_4 as non-absorbing material exists at higher local field than Si as absorbing material at two different commonly used laser excitation wavelengths, 633 and 785 nm. It shows the practicability of replacing Si with Si_3N_4 for enhancing the SERS ability. This phenomenon was observed experimentally in Raman measurement of R6G and BPE. The estimated EF of nanostructured Si_3N_4 SERS device is measured experimentally uniformly higher than the one on Si substrate by around 3 to 4 times depending on excitation laser wavelength. In the other words, higher SERS enhancement can be easily achieved by replacing substrate from absorbing to non-absorbing material. It provides a new path to further improve existing ultra-high sensitive SERS device based on light absorbing material such as silicon, which is beneficial to further extend this technique to better sensing sensitivity.

4.5. Figures and tables

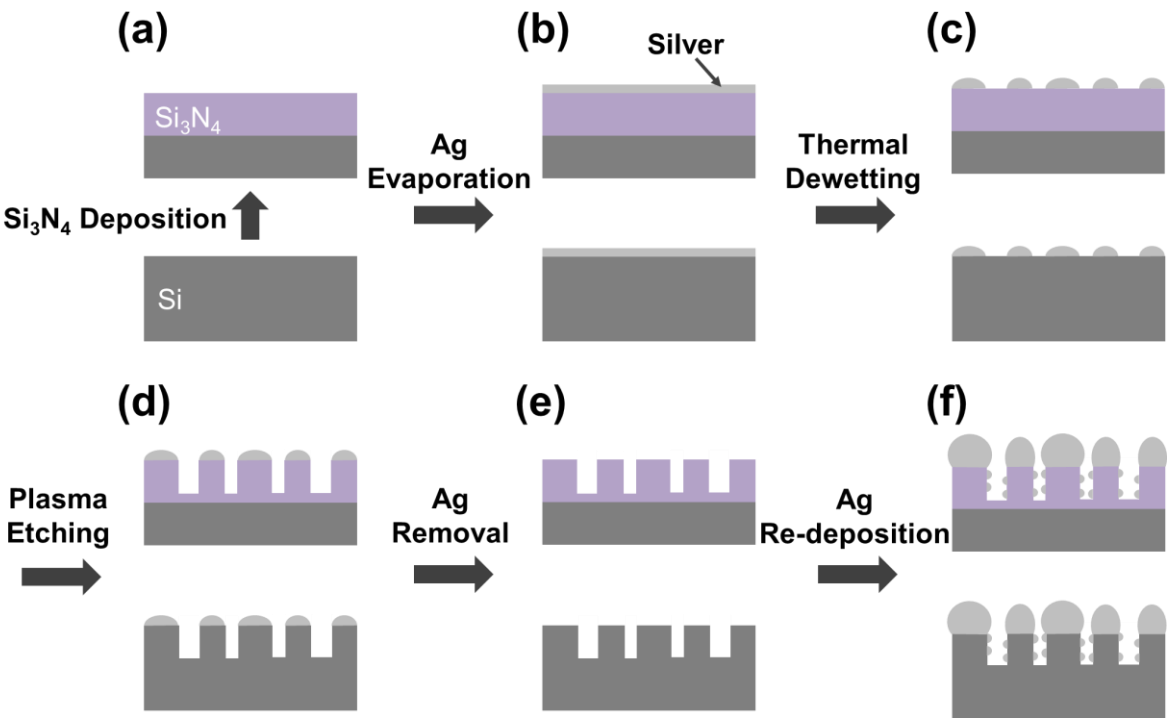

Figure 4.1 Schematic of processing steps for fabricating Si and Si_3N_4 SERS devices: (a) Si_3N_4 deposition by PECVD. (b) Ag thin film layer deposition by ebeam evaporation. (c) AgNPs generation by thermal dewetting technique. (d) Pattern transferred nanostructures by ICP-RIE. (e) AgNPs removal by silver etchant. (f) Ag re-deposition by ebeam evaporation.

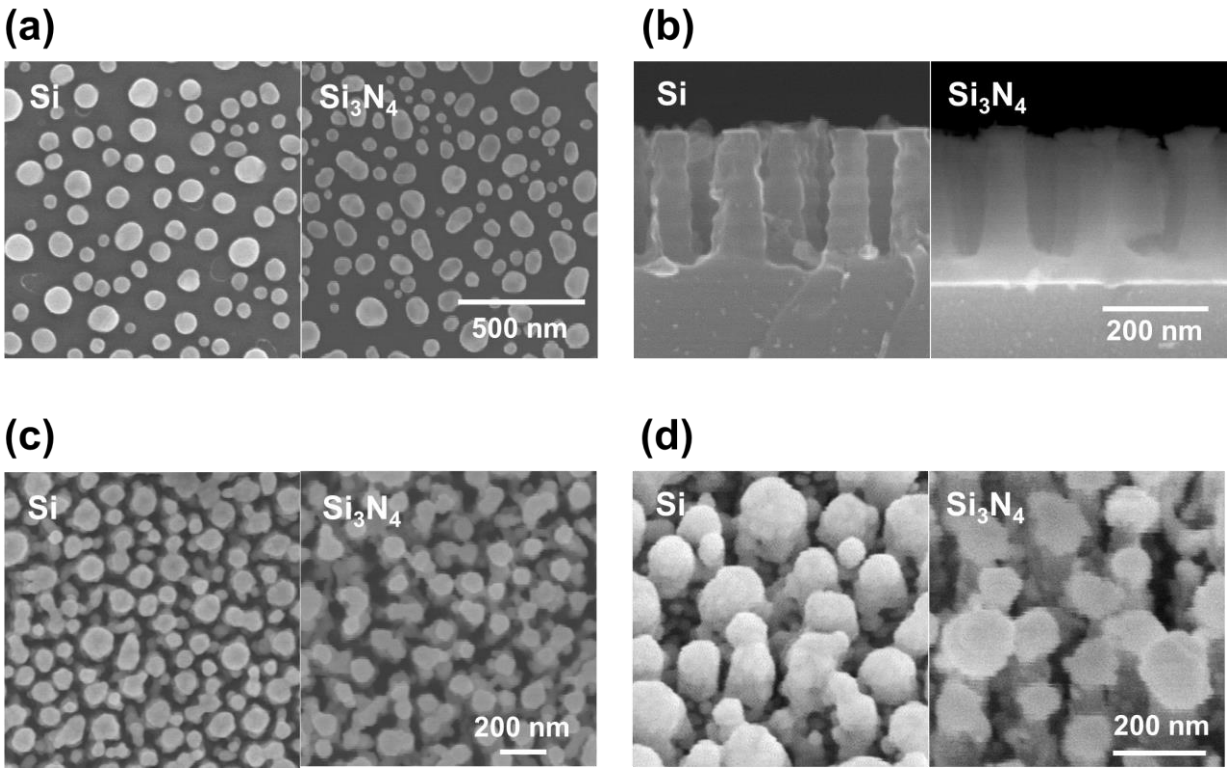

Figure 4.2 SEM images of (a) thermal dewetted AgNPs on Si and Si_3N_4 substrates. (b) Cross section view of etched Si and Si_3N_4 substrate. (c) Top view and (d) 30 degrees tilted view of 80nm Ag deposited Si and Si_3N_4 substrates after removal of thermal dewetted AgNPs.

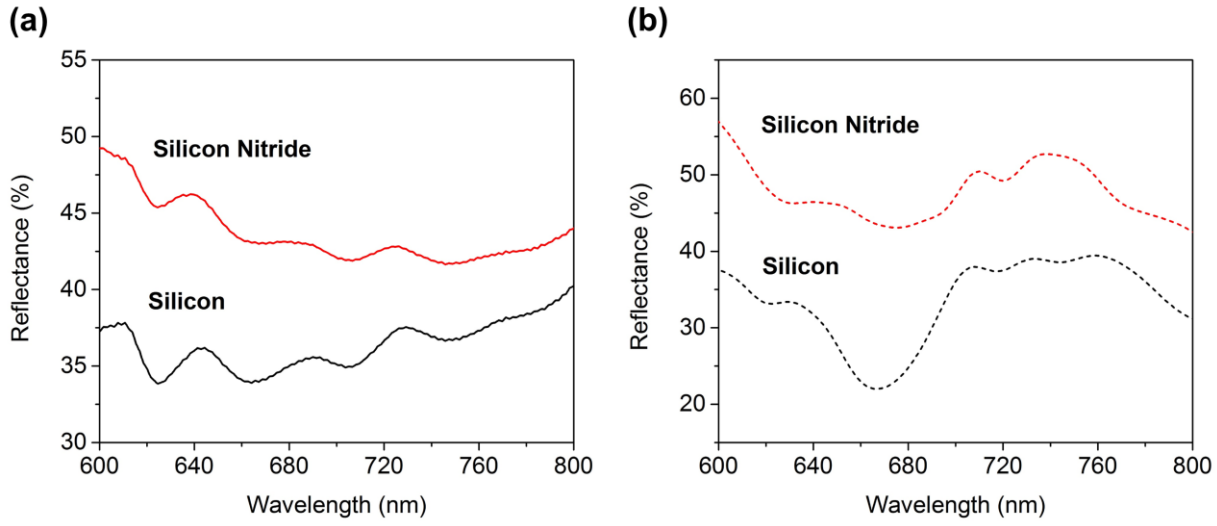

Figure 4.3 Spectrum of (a) measured spectral reflectance and (b) FDTD simulated spectral reflectance for Si and Si_3N_4 nanostructured SERS devices.

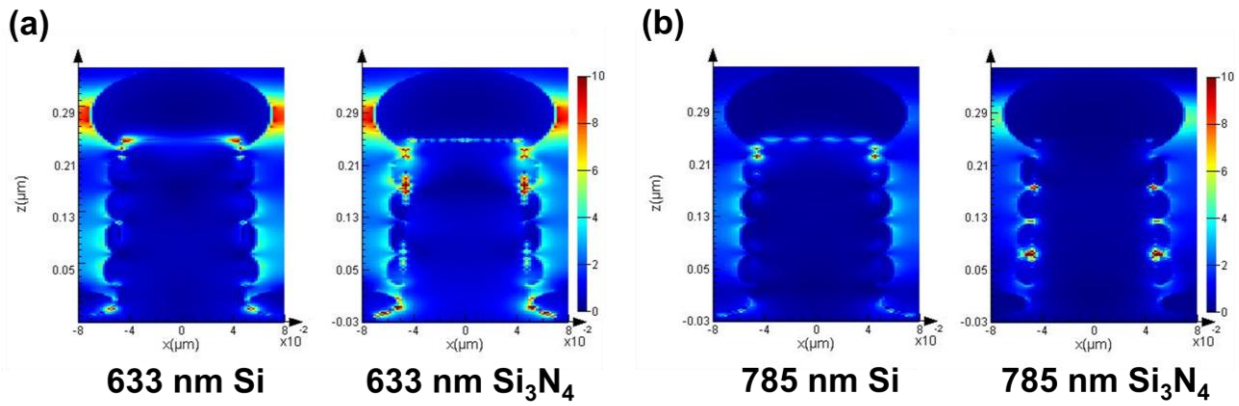

Figure 4.4 FDTD simulation of electric field distribution on Si and Si_3N_4 SERS nanostructured devices with excitation wavelength (a) 633 and (b) 785 nm.

Table 4.1. Simulated EF and enhancement ratio of Si and Si_3N_4 nanostructured SERS substrates with excitation wavelength at 633 and 785 nm.

	633 nm	785 nm
Simulated EF of Si nanostructured SERS device	1.11×10^6	1.28×10^5
Simulated EF of Si_3N_4 nanostructured SERS device	2.53×10^6	4.29×10^5
Enhancement ratio between Si and Si_3N_4 nanostructured SERS devices	2.30	3.35

Table 4.2 Measured enhancement ratio of R6G and BPE between Si and Si_3N_4 nanostructured SERS substrates with excitation wavelength at 633 and 785 nm.

Analyte	R6G		BPE	
Excitation wavelength (nm)	633	785	633	785
$I_{Si_3N_4}/I_{Si}$	2.5	4.21	3.35	4.00

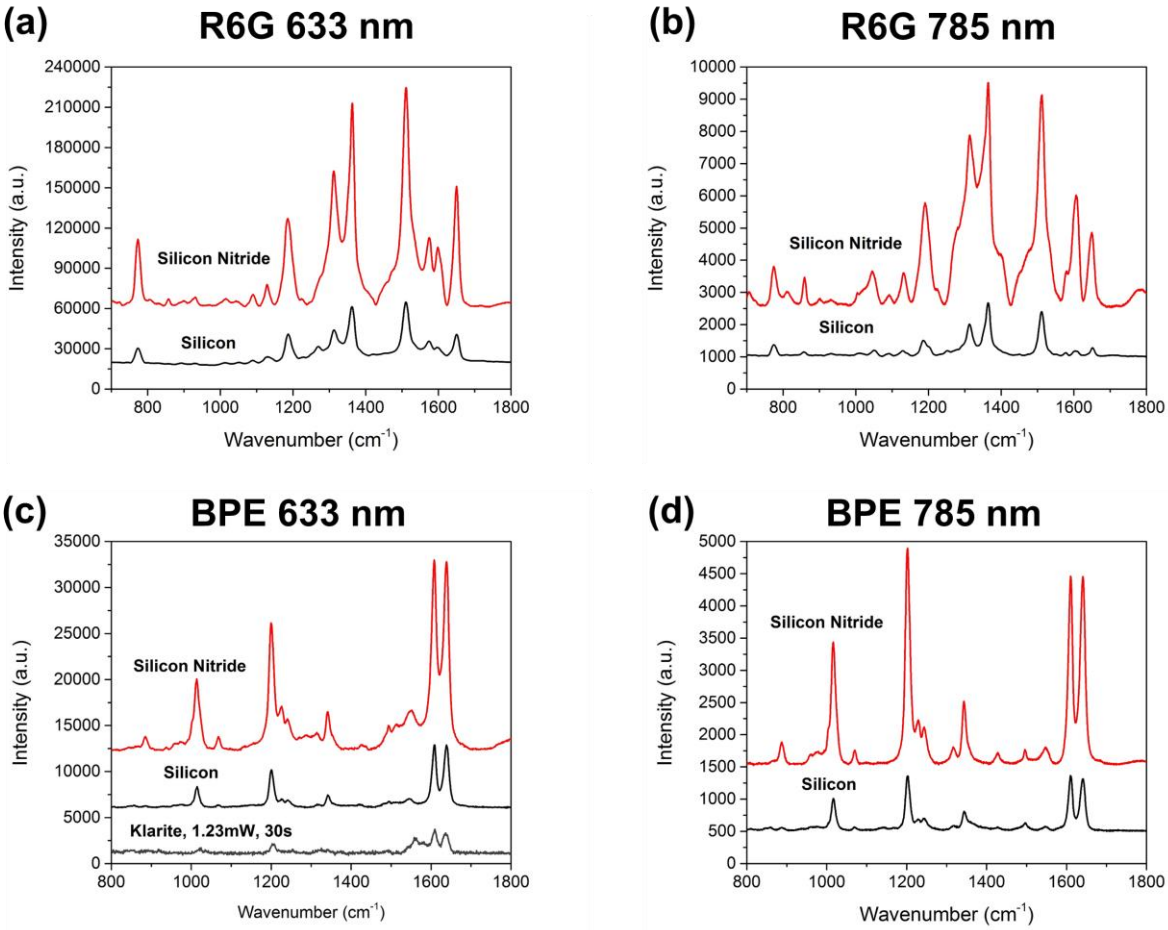

Figure 4.5 Raman spectrum of (a) R6G at 633 nm excitation wavelength. (b) R6G at 785 nm excitation wavelength. (c) BPE at 633 nm excitation wavelength. (d) BPE at 785 nm excitation wavelength on both Si and Si_3N_4 nanostructured SERS devices.

Table 4.3. Estimated EF and of Si and Si_3N_4 nanostructured SERS substrates with excitation wavelength at 633 and 785 nm based on commercial available Klarite SERS substrate.

	633 nm	785 nm
Estimated EF of Si nanostructured SERS device	2.19×10^7	4.34×10^6
Estimated EF of Si_3N_4 nanostructured SERS device	7.34×10^7	1.73×10^7

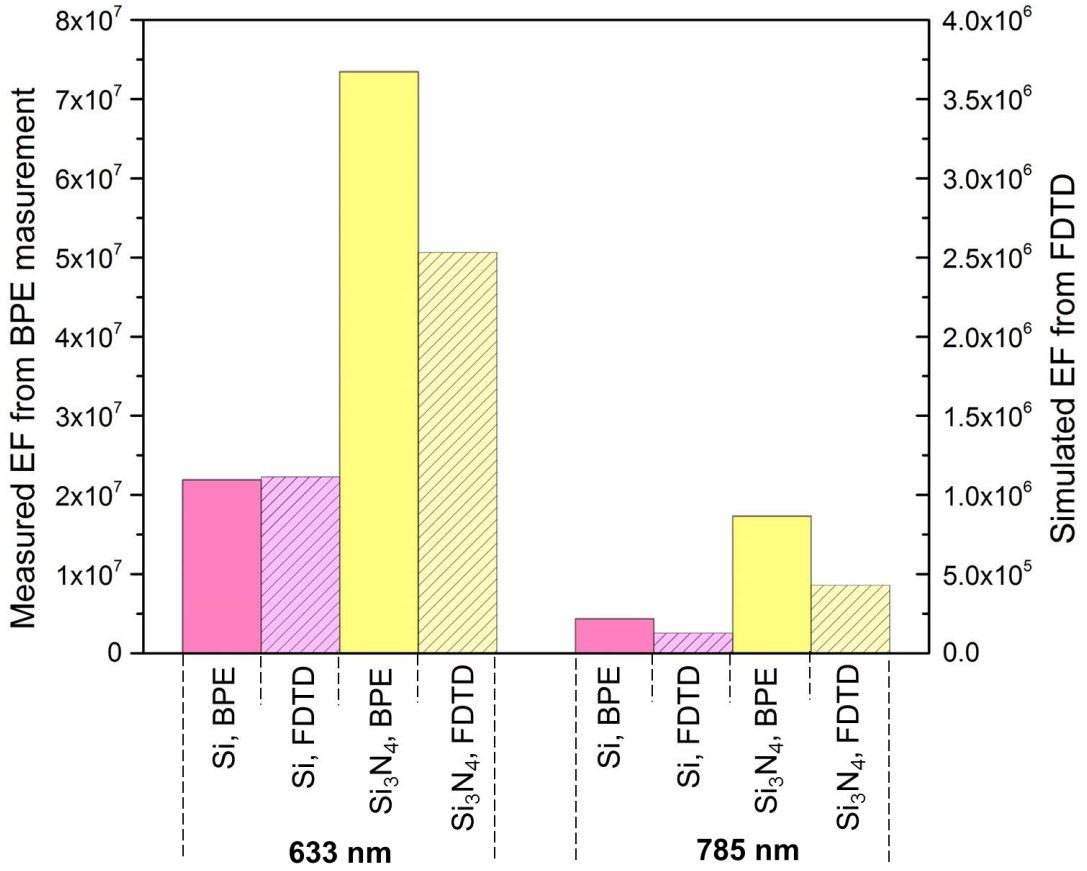

Figure 4.6 Comparison of measured BPE and FDTD simulated EF on both Si and Si_3N_4 nanostructured SERS devices with excitation wavelength 633 and 785 nm.

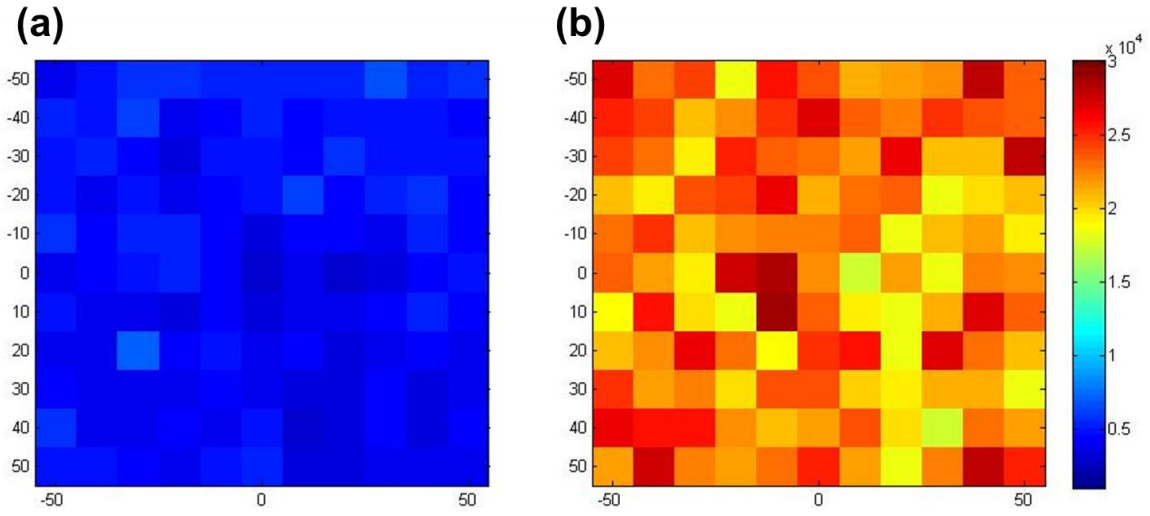

Figure 4.7 Mapping of Raman intensity at 1200 cm^{-1} of BPE on (a) Si and (b) Si_3N_4 nanostructured SERS devices at excitation wavelength 633 nm.

4.6. References

[1] Jiang, Z. Y.; Jiang, X. X.; Su, S.; Wei, X. P.; Lee, S. T.; He, Y. Silicon-Based Reproducible and Active Surface-Enhanced Raman Scattering Substrates for Sensitive, Specific, and Multiplex DNA Detection. *Appl. Phys. Lett.* **2012**, *100*, 203104.

[2] Sun, Y.; Pelton, M. Laser-Driven Growth of Silver Nanoplates on p-Type GaAs Substrates and their Surface-Enhanced Raman Scattering Activity. *Journal of Physical Chemistry C* **2009**, *113*, 6061-6067.

[3] Bian, J.; Li, Z.; Chen, Z.; He, H.; Zhang, X.; Li, X.; Han, G. Electrodeposition of Silver Nanoparticle Arrays on ITO Coated Glass and their Application as Reproducible Surface-Enhanced Raman Scattering Substrate. *Appl. Surf. Sci.* **2011**, *258*, 1831-1835.

[4] Dai, Z.; Xiao, X.; Liao, L.; Zheng, J.; Mei, F.; Wu, W.; Ying, J.; Ren, F.; Jiang, C. Large-Area, Well-Ordered, Uniform-Sized Bowtie Nanoantenna Arrays for Surface Enhanced Raman Scattering Substrate with Ultra-Sensitive Detection. *Appl. Phys. Lett.* **2013**, *103*, 041903.

[5] Yu, Q.; Braswell, S.; Christin, B.; Xu, J.; Wallace, P. M.; Gong, H.; Kaminsky, D. Surface-Enhanced Raman Scattering on Gold Quasi-3D Nanostructure and 2D Nanohole Arrays. *Nanotechnology* **2010**, *21*, 355301.

[6] Whitney, A. V.; Elam, J. W.; Zou, S. L.; Zinovev, A. V.; Stair, P. C.; Schatz, G. C.; Van Duyne, R. P. Localized Surface Plasmon Resonance Nanosensor: A High-Resolution Distance-Dependence Study using Atomic Layer Deposition. *J Phys Chem B* **2005**, *109*, 20522-20528.

[7] Aouani, H.; Wenger, J.; Gerard, D.; Rigneault, H.; Devaux, E.; Ebbesen, T. W.; Mahdavi, F.; Xu, T.; Blair, S. Crucial Role of the Adhesion Layer on the Plasmonic Fluorescence Enhancement. *Acs Nano* **2009**, *3*, 2043-2048.

[8] Chang, T.-W.; Gartia, M. R.; Seo, S.; Hsiao, A.; Liu, G. L. A Wafer-Scale Backplane-Assisted Resonating Nanoantenna Array SERS Device Created by Tunable Thermal Dewetting Nanofabrication. *Nanotechnology* **2014**, *25*, 145304.

[9] Tesler, A. B.; Chuntonov, L.; Karakouz, T.; Bendikov, T. A.; Haran, G.; Vaskevich, A.; Rubinstein, I. Tunable Localized Plasmon Transducers Prepared by Thermal Dewetting of Percolated Evaporated Gold Films. *Journal of Physical Chemistry C* **2011**, *115*, 24642-24652.

[10] Hayazawa, N.; Inouye, Y.; Sekkat, Z.; Kawata, S. Near-Field Raman Imaging of Organic Molecules by an Apertureless Metallic Probe Scanning Optical Microscope. *J. Chem. Phys.* **2002**, *117*, 1296-1301.

[11] Chu, H.; Liu, Y.; Huang, Y.; Zhao, Y. A High Sensitive Fiber SERS Probe Based on Silver Nanorod Arrays. *Optics Express* **2007**, *15*, 12230-12239.

[12] Xu, Z.; Jiang, J.; Gartia, M. R.; Liu, G. L. Monolithic Integrations of Slanted Silicon Nanostructures on 3D Microstructures and their Application to Surface-Enhanced Raman Spectroscopy. *J. Phys. Chem. C* **2012**, *116*, 24161-24170.

CHAPTER 5 RELIABLE SENSITIVITY AND UNIFORMITY IMPROVEMENT ON BIMETALLIC BARNA SERS SUBSTRATE BY SEED ASSISTED DEPOSITION

5.1. Introduction

SERS has been proved and recognized as a powerful analytical tool for label-free molecule identification especially in the region of low concentration detection [1]. However, the quantitative measurement is difficult to implement through SERS detection since the enhancement variation is not negligible with the MNPs in suspension or random nanostructured SERS substrate. On the other hand, periodic nanostructured SERS substrates fabricated by direct writing or template deposition methods show excellent deviation in enhanced Raman signal [2], but most of the available fabrication techniques are not appropriate for large-area, low-cost and high-efficiency production for industrial purposes.

In this chapter, a novel deposition technique will be introduced based on the thermal dewetting technique discussed in chapter 3. In addition to performing the pattern transferring process to create highly packed nanostructures, the thermal dewetted metallic nanoparticle array is retained and used as initial seeds for subsequent metal deposition. By this method, a more uniform nanoantenna array can be achieved both in size and shape, which leads this technique to a higher controllability for creating ultrahigh density array of SERS active hot spot. Besides, with the selection of the material in metallic nanoparticle seed array and successive metal deposition, the bimetallic nanoantenna array can be obtained without traditional chemical synthesis methods [3-4] and improves the sensitivity and stability. Most importantly, all these advantages from seed assisted deposition are based on taking out one process, the pattern stripping, from the previous fabrication procedure, which actually reduces the process time and reduces the process complexity.

5.2. Materials and methods

5.2.1. Nanofabrication process

Figure 5.1 depicts the schematic of bimetallic BARNA SERS substrate fabrication with the seed assisted deposition, which is similar to the process mentioned in chapter 3. Firstly, the single crystalline p-type doped silicon wafers were cleaned with acetone, isopropyl alcohol and DI water before preceding to any further fabrication steps. Then different thicknesses of gold thin film (4, 6, 8, 10 and 12 nm) were deposited on the substrate by Temescal six pocket electron-beam evaporation systems for thermal dewetting process as shown in figure 5.1 (a).

In order to perform thermal dewetting, rapid thermal process (RTP) system Jipelec rapid thermal processor was applied for injecting thermal energy to gold thin film, inducing thermal disturbance and eventually engendering isolated AuNPs array as shown in figure 5.1 (b). The advantage of the RTP system is significantly reduced heating time and ability to finish the process within a few minutes. The chamber was purged with nitrogen gas to prevent any oxidation during the whole process. The dewetting temperature was set at 500 °C for 90 to 600 sec.

After thermal dewetting process, pattern of metal nanoparticles was transferred by dry etching technique as shown in figure 5.1 (c). In this step, inductively coupled plasma reactive ion etching (ICP-RIE) STS advanced silicon etcher was used. The controllable aspect ratio structure can be achieved by continuously applying etching and passivation processes. SF_6 and O_2 were used for etching phase and C_4F_8 was used for passivation process. The pressure was set to 40 mTorr and the RF powers of inductive and capacitive chamber were set to be 350W and 12W respectively. Instead of removing the thermal dewetted AuNPs after pattern transferring, it was intentionally retained and used as the initial seeds for second deposition. Subsequently silver was deposited by CHA SEC-600 electron-beam evaporator system. The power of the electron beam

was 10 kV and the operating pressure was around 10^{-7} Torr. Evaporation rate was set to 0.5 Å/s to ensure uniformity of the silver layer. The deposited thicknesses were varied from 30 to 90 nm in order to find optimal SERS performance. This further deposition of different metal material is able to grow around the AuNPs seed as well as bottom surface and create a unique bimetallic backplane nanoantenna as shown in figure 5.1 (d) without any chemical synthesis reaction.

5.2.2. SERS measurement

Renishaw PL/Raman micro spectroscope system was used for Raman spectra measurement. 20X objective lens was used for focusing and collecting incident laser and Raman signals. The wavelength of excitation light source was 633 nm and acquisition time was set to 10 s. The laser intensity was varied from 1.22 mW to 211 μW in order to prevent saturation of the detector. The measured wavenumber range was from 1100 to 1900 cm^{-1}. Raman intensity mapping has been done with the laser intensity of 211 μW and integration time of 10 s. The total mapping area is 1 mm × 1mm with the step of 50 μm.

5.2.3. Numerical simulation

The near field analysis was studied by using the three-dimensional finite-difference time-domain (3D-FDTD) method and implemented by FDTD software from Lumerical Solutions, Inc. The simulated model is built by importing the SEM image. The transverse magnetic (TM) polarized electromagnetic wave was set to propagate normal to the substrate for both diffuse reflectance simulation and plasmonic enhancement simulation. The boundary condition for x, y and z directions was a perfectly matched layer to eliminate any erroneous reflection from the boundary and the maximum mesh size around the metal particles was 1.5 nm.

5.3. Results and discussion

5.3.1. Uniformity improvement

Figure 5.2 (a) and (b) show the SEM image comparison of nanostructured backplane assisted nanoantenna array with and without the seed assisted deposition. It can be clearly observed that the thermal dewetted nanoparticles act as initial seeds for a more uniform growth of successive metal deposition around them instead of non-selective physical vapor deposition. The inset in figure 5.2 (b) is the corresponding cross section SEM image which shows a clear view of top bimetallic nanoantenna array and bottom backplane. Since selective metal deposition can be achieved with the assistance of thermal dewetted seeds, it leads to a better controllability for creating highly compacted SERS active hot spots. Since the actual SERS signal is the collection of scattered photons from the laser focused region, the density of hot spots can improve the average enhanced Raman signal in not only magnitude but also uniformity. The spot size depends on the optical equipment such as objective lens and optical path collimation, which is usually in the range of a few μm. If a relatively high density of hot spots compared to the spot size can be achieved, the SERS substrate can be considered as uniformly SERS active all over the whole surface and, as a result, the randomness of the nanostructure can be ignored.

5.3.2. Optimization of nanofabrication process

In the session, the optimization process of highly compact SERS active hot spots through thermal dewetting and seed assisted deposition techniques is demonstrated to achieve both high sensitivity and uniformity. Figure 5.3 (a) shows the average thermal dewetted AuNPs size with one standard deviation performed by different deposition thicknesses of 4, 6, 8, 10 and 12 nm. It can be observed that when the thickness of thin film is smaller than 8 nm, the average size of

AuNPs increases slightly with the increment of Au thin film thickness. When the thin film thickness is larger than 8 nm, the size of the nanoparticles grows faster. The inter-distance of thermal dewetted nanoparticles can be assumed to be similar to the size of nanoparticles because the nanoparticle array is generated based on the thermal capillary perturbation.

Based the optimization discussion in chapter 3, two major parameters need to be considered to obtain high Raman enhancement. The first is the distance between the bottom backplane and top nanoantenna array, which is determined by the dry etching depth in the pattern transferring procedure. Here the etching depth is set to be 100 nm since this height has been proved in chapter 3 to have largest oscillation between top and bottom metal layers to contribute the enhanced lateral coupling. However, since the growth rate and morphology of a nanoantenna is quite different with seed assisted deposition applied, the optimization of the second critical parameter, i.e. the thickness of secondary deposition, needs to be evaluated again. Here the self-assembled monolayer of trans-1,2-bis(4-pyridyl)ethylene (BPE, Sigma-Aldrich, 99%) was applied. Firstly both of the devices were immersed in 5mM BPE ethanolic solution for 24 hours and then rinsed with pure ethanol solution to wash out extra BPE molecules stacked on the monolayer. Finally devices were blown with nitrogen gas to completely dry. Figure 5.3 (b) shows the BPE Raman spectra of different thicknesses of secondary deposition (30, 50, 70 and 90 nm) on the bimetallic backplane nanoantenna array fabricated by thermal annealing 6 nm Au thin film. By this method, the optimized deposition thickness can be discovered with certain inter-spacing of AuNPs pattern. It implies that the deposition thickness of first and second metal deposition have a dependent relationship to achieve the optimized design. As a result, a variety of combinations of these two deposition thicknesses, i.e. first thinner film for thermal dewetting phenomena (4, 6, 8, and 10 nm) and second thicker layer for creating hot spots (30, 50, 70 and 90 nm), have been examined and

are shown in figure 5.3 (c). It can be observed that a secondary Ag deposition of 50 nm on a 6 nm Au thin film thermal dewetted substrate provides the highest enhancement, which is the optimization design of bimetallic BARNA SERS substrate. As shown in figure 5.3 (d), compared with the optimized BARNA SERS substrate mentioned in chapter 3, the SERS signal is increased by 4 times with the seed assisted deposition, which also reduces the process time and complexity by skipping the pattern stripping step. The enhancement exceeds the commercially available Klarite substrate by three orders and the average EF is calculated as 5.8×10^8.

5.3.3. Near field simulation from FDTD

In order to visualize the SERS active hot spots created by bimetallic backplane nanoantenna array, the FDTD simulation is performed and shown in figure 5.4. The model is created by importing the actual geometry from the SEM image as shown in figure 5.4 (a). Figure 5.4 (b) shows the simulated results of near field distribution. In this simulation model there are two effects that cannot be simulated: one is the bimetallic configuration of top nanoantenna and the other is the supported metal backplane. As a result, the actual enhancement should be higher than what has been shown in this model. Nevertheless, it can be observed that the highly compact hot spots exists among the nanostructures, which supports the high enhancement from Raman measurement. In addition, as discussed before, the highly compact hot spot should provide higher uniformity of enhancement signal. Figure 5.5 demonstrates the uniformity comparison of Raman mapping between the optimized nanostructured SERS substrate with and without seed assisted deposition. The targeted molecule is monolayer coated BPE and the Raman peak signal is measured at 1607 cm^{-1}. The relative standard deviation (RSD) is improved from 15.2 % to 4.8 %, which indicates the uniformity is significantly improved with the help of this technique. Table 5.1 lists a variety of SERS substrates which are claimed as highly uniform with the substrate presented in this work. It

can be obviously seen that the bimetallic BARNA SERS substrate proposed here holds equal or better enhanced Raman signal uniformity as well as the high enhancement compared with periodic nanostructure SERS substrate but with a rapid, reliable, cost-efficient and large-area fabrication technique.

5.4. Conclusion

An improved fabrication process based on thermal dewetting technique is demonstrated in this chapter, which utilizes the thermal dewetted AuNPs array as not only the mask for pattern transferring but an initial seed array for secondary Ag deposition. With the help of the seed assisted deposition, better controllability of metallic nanoparticles in both size and shape can be achieved, which leads to a highly compact SERS active hot spot array. From the analysis it has been found that the dependence between the first and second metal deposition plays a significant role to attain the desired effect. A comprehensive discussion of this dependence is conducted to find the optimized design. In addition, the bimetallic configuration can be achieved by selecting the materials of first and second metal deposition without any chemical synthesis process. The bimetallic configuration of Au core and Ag shell should provide additional advantages of better oxidation resistivity [5] and higher SERS active core-shell interaction from electronic ligand effect [6-7] according to past research findings. FDTD simulations confirm the highly compact SERS active hot array exists within the substrate. The average enhancement factor (EF) and relative standard deviation (RSD) are calculated as 5.8×10^8 and 4.7 %, which is significantly improved compared to the previous optimized BARNA SERS substrate by 4× in enhancement and 3× in uniformity.

5.5. Figures and table

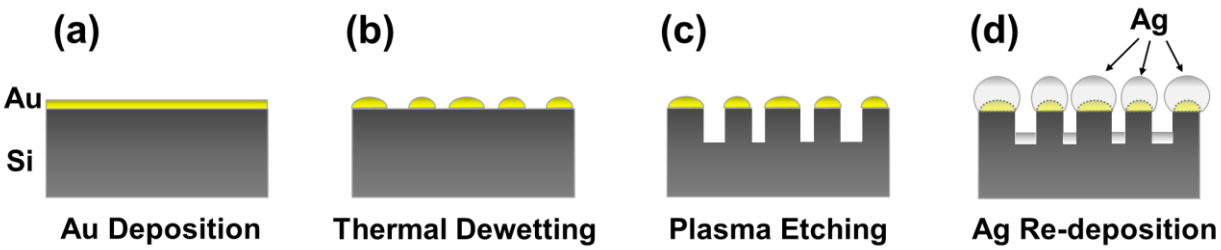

Figure 5.1 Schematic of nanostructured BARNA SERS substrate fabrication with seed assisted deposition: (a) Au thin film layer deposition by ebeam evaporation. (b) AuNPs generation by thermal dewetting technique. (c) Pattern transferred nanostructures by ICP-RIE technique. (d) Ag deposition with the assistance of initial seed array by ebeam evaporation.

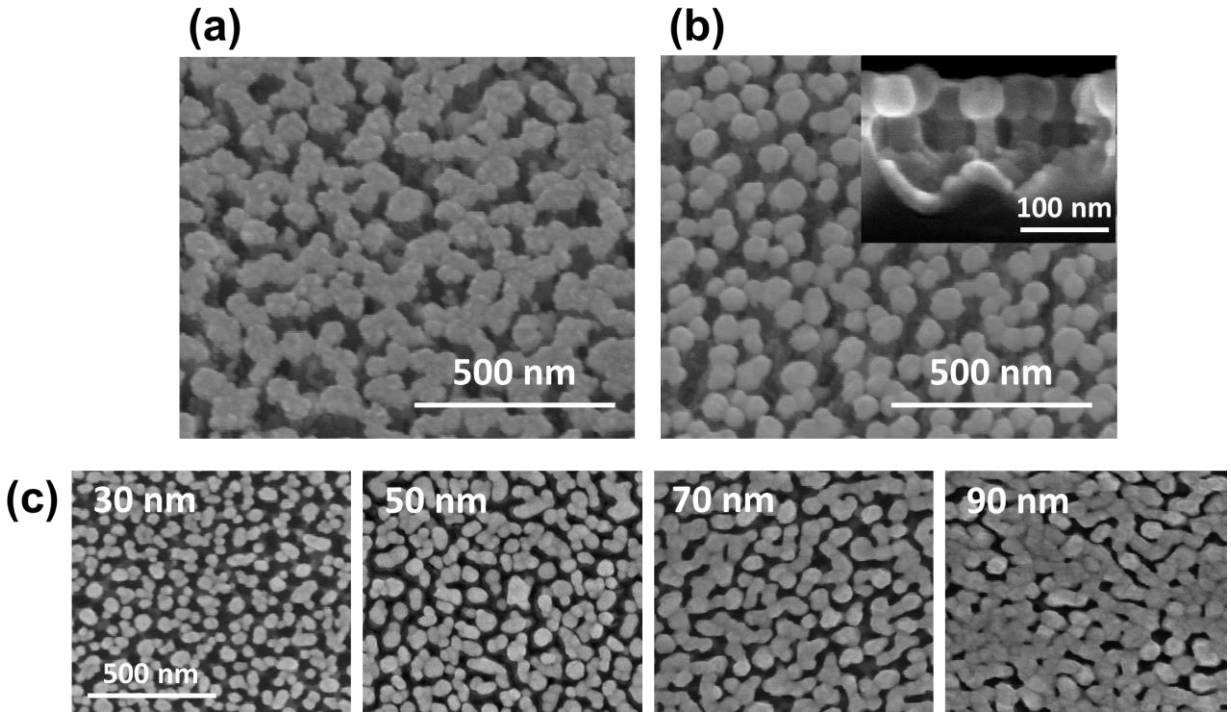

Figure 5.2 The 30° tilted SEM images of nanostructured bimetallic backplane nanoantenna (a) without and (b) with seed assisted deposition. The inset in (b) is the cross section of the structure and shows the spherical shape of bimetallic nanostructure and the backplane at the bottom. (c) The SEM images indicate the influence by depositing different thicknesses of silver (30, 50, 70 and 90 nm). The base nanostructured substrate shown here is fabricated from the thermal dewetted pattern by annealing 6 nm Au thin film.

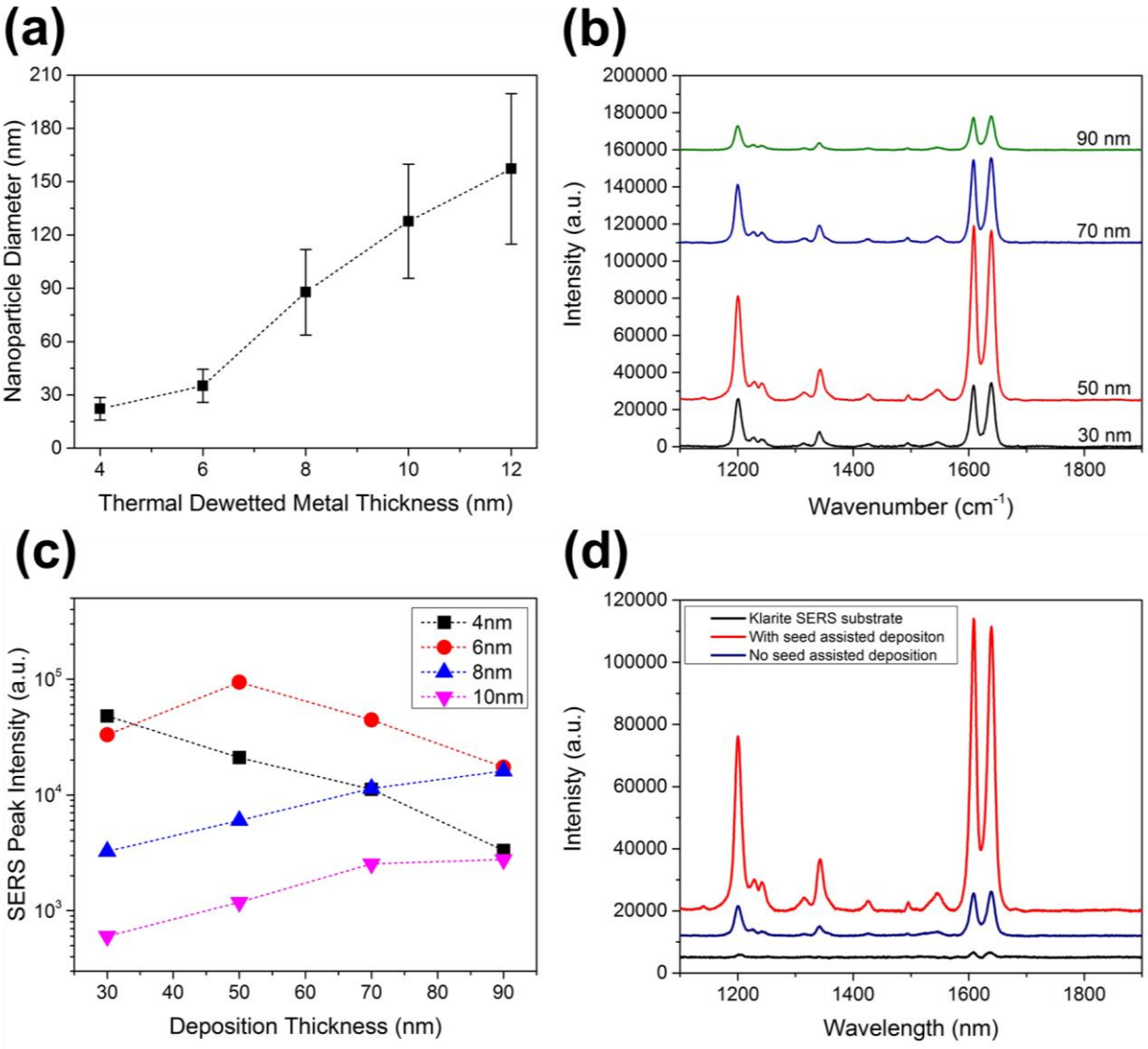

Figure 5.3 (a) The average and deviation of thermal dewetted AuNPs size with the deposition thickness of 4, 6, 8, 10 and 12 nm. (b) Raman spectra of BPE with different Ag deposition thickness (30, 50, 70 and 90 nm). The base nanostructured substrate shown here is fabricated from the thermal dewetted pattern by annealing 6 nm Au thin film. (c) The comparison of SERS peak intensity of BPE at 1607 cm^{-1} with different Ag deposition thickness (30, 50, 70 and 90 nm). The different symbol denotes different nanostructured SERS substrates fabricated from annealing on different thickness of Au thin film (4, 6, 8 and 10 nm). (d) The BPE Raman spectra of optimized nanostructured SERS substrate with and without seed assisted deposition. The Raman spectrum of commercially available Klarite substrate is also shown here for comparison.

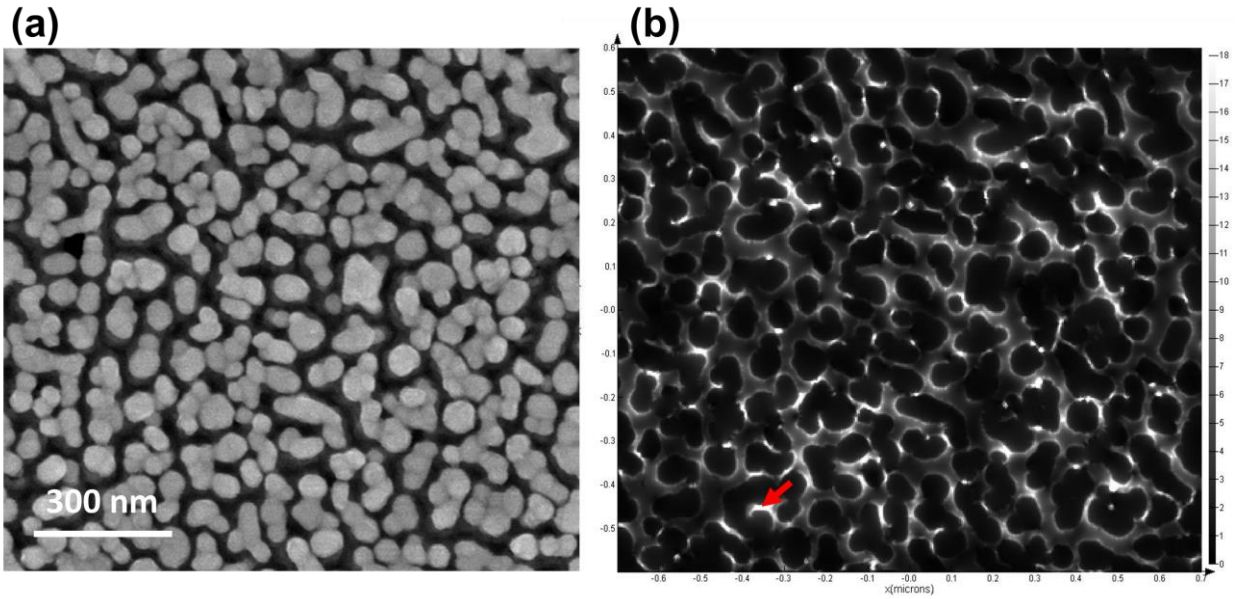

Figure 5.4 (a) The SEM image of optimized bimetallic backplane nanoantenna array (6 nm Au thin film for thermal dewetting, 100 nm of etching depth and 50 nm secondary Ag deposition). (b) FDTD electric field distribution of optimized bimetallic backplane nanoantenna array imported by the SEM image from (a). The arrow indicates the SERS active hot spot.

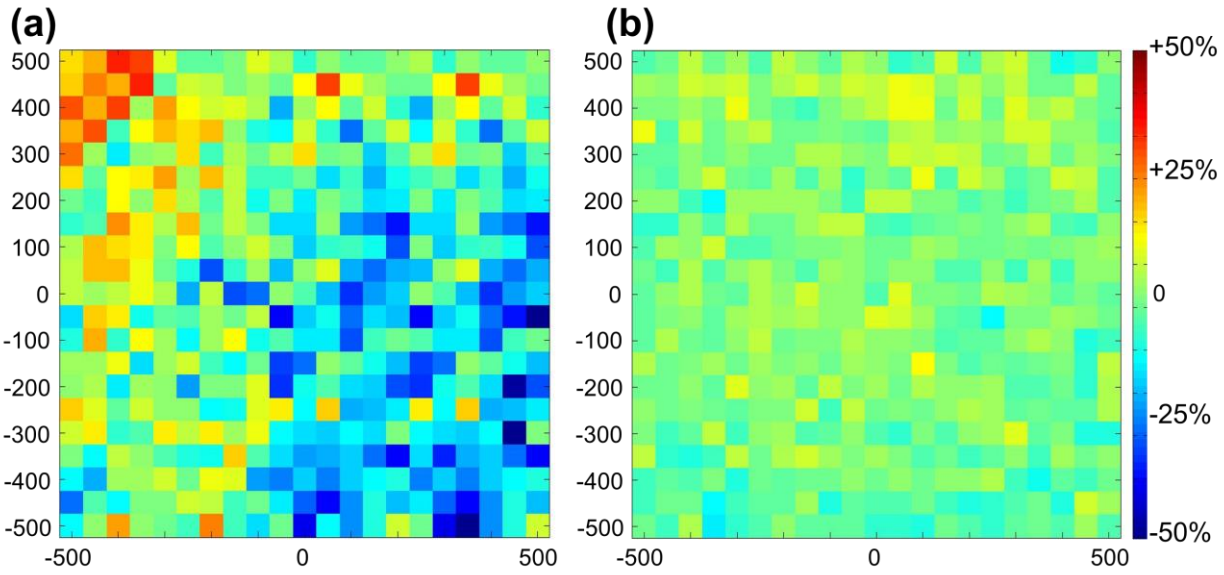

Figure 5.5 The mapping of BPE Raman intensity at 1607 cm^{-1} on (a) optimized BARNA SERS substrate and (b) nanostructured bimetallic backplane nanoantenna array at excitation wavelength 633 nm.

Table 5.1 The comparison of current work and highly uniform SERS substrates from other literature. The detail of excitation laser wavelength, calculated enhancement factor, mapping area/spectrum counts and relative standard deviation are listed.

Fabrication technique	Excitation Laser Wavelength	Enhancement Factor	Raman Mapping Area/spectrum counts	Relative Standard Deviation	Ref
silver-coated tapered silica nanopillar arrays	785 nm	4.8×10^7	200 × 200 μm	15.4 %	[2]
Femtosecond Laser Structuring Process	633 nm	NA	500 × 600 μm	12.9 %	[8]
Silver nanosheet-coated inverse opal film	514 nm	6×10^7	120 × 70 μm	> 5%	[9]
3D cavity nanoantenna coupled plasmonic nanodots	785 nm	1.2×10^9	1.6 × 1 mm	25%	[10]
Ultrahigh-Density Array of Silver Nanoclusters	514 nm	$\sim 10^8$	NA	± 5%	[11]
Bimetallic nanostructured backplane nanoantenna array	633 nm	5.8×10^8	1 × 1 mm	4.7 %	Current work

5.6. References

[1] De Angelis, F., et al. Breaking the Diffusion Limit with Super-Hydrophobic Delivery of Molecules to Plasmonic Nanofocusing SERS Structures. *Nature Photonics* **2011**, *5*, 683-688.

[2] Gartia, M. R.; Xu, Z.; Behymer, E.; Nguyen, H.; Britten, J. A.; Larson, C.; Miles, R.; Bora, M.; Chang, A. S.; Bond, T. C.; Liu, G. L. Rigorous Surface Enhanced Raman Spectral Characterization of Large-Area High-Uniformity Silver-Coated Tapered Silica Nanopillar Arrays. *Nanotechnology* **2010**, *21*, 395701.

[3] Dong, X.; Zhou, J.; Liu, X.; Lin, D.; Zha, L. Preparation of Monodisperse Bimetallic Nanorods with Gold Nanorod Core and Silver Shell and their Plasmonic Property and SERS Efficiency. *J. Raman Spectrosc.* **2014**, *45*, 431-437.

[4] Sanchez-Iglesias, A.; Aldeanueva-Potel, P.; Ni, W.; Perez-Juste, J.; Pastoriza-Santos, I.; Alvarez-Puebla, R. A.; Mbenkum, B. N.; Liz-Marzan, L. M. Chemical Seeded Growth of Ag Nanoparticle Arrays and their Application as Reproducible SERS Substrates. *Nano Today* **2010**, *5*, 21-27.

[5] Sanchez-Iglesias, A.; Aldeanueva-Potel, P.; Ni, W.; Perez-Juste, J.; Pastoriza-Santos, I.; Alvarez-Puebla, R. A.; Mbenkum, B. N.; Liz-Marzan, L. M. Chemical Seeded Growth of Ag Nanoparticle Arrays and their Application as Reproducible SERS Substrates. *Nano Today* **2010**, *5*, 21-27.

[6] Toshima, N.; Yonezawa, T.; Harada, M.; Asakura, K.; Iwasawa, Y. The Polymer-Protected Pd-Pt Bimetallic Clusters having Catalytic Activity for Selective Hydrogenation of Diene - Preparation and Exafs Investigation on the Structure. *Chem. Lett.* **1990**, 815-818.

[7] Pande, S.; Ghosh, S. K.; Praharaj, S.; Panigrahi, S.; Basu, S.; Jana, S.; Pal, A.; Tsukuda, T.; Pal, T. Synthesis of Normal and Inverted Gold-Silver Core-Shell Architectures in Beta-Cyclodextrin and their Applications in SERS. *Journal of Physical Chemistry C* **2007**, *111*, 10806-10813.

[8] Diebold, E. D.; Mack, N. H.; Doom, S. K.; Mazur, E. Femtosecond Laser-Nanostructured Substrates for Surface-Enhanced Raman Scattering. *Langmuir* **2009**, *25*, 1790-1794.

[9] He, L.; Huang, J.; Xu, T.; Chen, L.; Zhang, K.; Han, S.; He, Y.; Lee, S. T. Silver Nanosheet-Coated Inverse Opal Film as a Highly Active and Uniform SERS Substrate. *Journal of Materials Chemistry* **2012**, *22*, 1370-1374.

[10] Li, W.; Ding, F.; Hu, J.; Chou, S. Y. Three-Dimensional Cavity Nanoantenna Coupled Plasmonic Nanodots for Ultrahigh and Uniform Surface-Enhanced Raman Scattering Over Large Area. *Optics Express* **2011**, *19*, 3925-3936.

[11] Cho, W. J.; Kim, Y.; Kim, J. K. Ultrahigh-Density Array of Silver Nanoclusters for SERS Substrate with High Sensitivity and Excellent Reproducibility. *Acs Nano* **2012**, *6*, 249-255.

CHAPTER 6 NANOJET AND SURFACE ENHANCED RAMAN SPECTROSCOPY (NASERS) FOR HIGHLY REPRODUCIBLE AND CONTROLLABLE SINGLE MOLECULE DETECTION

6.1. Introduction

In chemical analysis and biological detection, researchers are devoted to thrust the detection limit to the level of single molecule. It was first achieved by fluorescence microscopic method [1-3]. However, fluorescence signal provides limited information such that identification of targeted molecule is barely possible. In contrast, vibrational spectroscopy such as Raman spectroscopy provides not only the capability of molecule detection but precise identification from molecular vibrational modes [4]. In general, typical scattering cross section of Raman signal ranges from 10^{-25} to 10^{-30} cm^{-1}, which encumbers the use of this technique in the low concentration sensing regime. Surface enhanced Raman spectroscopy (SERS) has overcome this obstruction and significantly increases the effective scattering cross section to the same order of other spectroscopic methods such as fluorescence spectroscopy [5]. It is achieved by locating the targeted molecule to the proximity of roughened metal surface or metal nanoparticles [6]. The enhancement is contributed by two mechanisms. One is the charge transfer enhancement, which is due to the additional electronic transition between metal and targeted molecule [7]. The other mechanism is electromagnetic enhancement. The targeted molecule experiences higher electric field by the localized surface plasmonic resonance (LSPR) of noble metal material. As a result, the Raman signal can be substantially amplified by approximately the ratio between localized and incident field to the fourth power [8].

First single molecule Raman spectroscopy was achieved by mixing targeted molecule into metallic nanoparticle colloidal solution. The “hotspots” from the aggregation of nanoparticles

contribute remarkably strong coupling effect for detecting a few or even a single targeted molecule [9]. Nevertheless, the aggregation of nanoparticle colloidal is difficult to control. As a result, neither the SERS performance nor hot spot location is predictable, which is undesired for sensing applications. Later on researchers attempted another method to fabricate bottom-up nanostructured SERS substrate with the advance of nanofabrication technique. Different approaches have been adopted such as ebeam lithography, focused ion beam milling, and nanosphere template deposition [10-12]. So far a reliable and simple fabrication method for fabricating both low cost and single molecule level SERS substrate is still a challenge.

In 2004, Chen et al. proposed a simple but effective way to perform subwavelength two-dimensional confinement of plane wave by micro-scale infinite dielectric cylinder [13]. The simulation results demonstrated that a "photonic nanojet" can be induced at the shadow side of microcylinder. In consequence, the backscattering of nanoparticle located near the nanojet can be enhanced by 3 to 5 orders depending on the size of the nanoparticle. Later on, a three-dimensional subwavelength confinement was proposed by applying incident Gaussian beam and dielectric microsphere [14]. Based on this phenomenon, nanojet enhanced Raman scattering has been demonstrated with the enhancement of two orders [15].

Here the combination of two enhancement approaches, i.e. plasmonic and nanojet enhanced methods, is proposed in order to construct a stable platform for single molecule Raman detection. Upon the enhancement achieved from bimetallic BARNA nanostructured SERS substrate, the additional dielectric microsphere confines the incident field and is expected to thrust the enhancement significantly. This microsphere-analyte-nanostructured SERS substrate configuration is not only to provide a simple and effective method to enhance the Raman signal.

Moreover, the three-dimensional confinement from nanojet effect offers the additional advantage of reducing the detection region.

6.2. Materials and methods

6.2.1. NASERS device fabrication

The schematic of NASERS device preparation is shown in figure 6.1 (a). The substrate used was p-type doped silicon wafer with crystalline orientation of <1,0,0>. A 6 nm Au thin film was deposited on the substrate by e-beam evaporation. Then thermal dewetting technique was performed to generate self-assembled Au nanoparticles (AuNPs) pattern. The annealing was conducted for 90 s at 500 °C. After obtaining AuNPs, the pattern was transferred onto substrate by reactive ion etching technique. Finally another thicker layer of 50 nm Ag was deposited on the nanostructured substrate. This process can significantly increase the hot spot effect by reducing the gap among metal nanostructures

After nanostructured SERS substrate has been fabricated, a 5 µL droplet of targeted molecules was placed onto the SERS substrate. Once the targeted molecule solution was completely dried, a 2 µL of 5 µm SiO_2 microsphere solution was hand-dropped onto the sensing region to form the sandwich configuration of microsphere-analyte-nanostructured SERS substrate. Figure 6.1 (b) shows the scanning electron microscopy (SEM) images of nanostructured SERS substrate. It can be observed that the Ag is mainly deposited on the top of the silicon nanostructures and forms a highly compacted Ag nanoparticle array. It helps to create a high density of hot spot coupling effect for SERS enhancement.

6.2.2. FDTD simulation

The numerical simulations of plasmonic and optical enhancement property were studied by using three-dimensional finite-difference time-domain (3D-FDTD) method with FDTD software package from Lumerical Solutions, Inc. The x-axis polarized electromagnetic Gaussian wave was set to propagate normal to the substrate (-z direction). All boundary conditions were set to be perfectly matched layers to eliminate any interference from the boundaries. The profile is modeled from the observation of the SEM image. The electric field result observed in this chapter is at x-z plane at y = 0 and the mesh size was set as 1 nm^3.

6.2.3. Raman spectroscopy measurement

Renishaw PL/Raman micro-spectroscope system was used in this paper for enhanced Raman signal measurements. 633 nm He-Ne laser was used as excitation light source. 20× objective lens was used to focus/collect incident light and Raman signal onto/from the surface of NASERS devices.

6.3. Results and discussion

6.3.1. FDTD simulation results of nanojet and plasmonic enhancement

The FDTD simulation results of enhancement effect due to nanojet and plasmonic substrate are demonstrated in figure 6.2. Firstly a Gaussian beam was set to propagate to a 5 μm SiO2 microsphere. The waist of the beam was set to be 3.03 μm to fit the spot size of the focused laser through objective lens in the Raman measurement. The focal plane was set at the center of the microsphere. As figure 6.2 (a) shows, a 3D confinement of electric field was generated as nanojet effect and the diameter of the confined beam is about 1 μm. Figure 6.2 (b) and (c) show the comparison between plasmonic nanostructured SERS substrate with and without the presence of

microspheres. It can be observed that the electric field was amplified significantly by around two orders with the nanojet effect. It indicates that the dramatic increase of near field by adding the microsphere is expected to contribute higher enhancement to the Raman signal.

6.3.2. Results of Raman spectroscopy

Firstly the experimental effect of nanojet enhancement to nanostructured SERS substrate was investigated. The targeted molecule used here was 1,2-bis(4-pyridyl)ethylene (BPE, Sigma-Aldrich). The substrate was immersed in 5 mM BPE ethanolic solution for 24 hours and then rinsed with pure ethanol solution to wash out extra BPE molecules stacked on the monolayer. Finally the substrate was blown with nitrogen gas to completely dry. Figure 6.3 (a) shows the enhancement comparison of BPE Raman spectrum with and without microsphere. It can be observed that the nanojet effect from microsphere contributes a significantly higher Raman enhancement by 5 times. Nevertheless, since the nanojet provides confinement phenomenon of incident field, the actual number of targeted molecules is greatly decreased. The enhancement from the nanojet effect is approximately 183 times.

In order to perform single molecule detection, rhodamine 6G (R6G, Sigma-Aldrich), which is a commonly used dye for low concentration detection, has been applied here as targeted molecule. Firstly the SERS performance of only nanostructure SERS substrate is evaluated and the Raman spectra of different concentrations of R6G are shown in Figure 6.3 (b). The Raman peaks from R6G can still be identified when the concentration is down to 10^{-8} M. Figure 6.3 (c) shows the Raman spectrum after adding microsphere onto the nanostructured SERS substrate. Under low concentration condition, the Raman spectrum is slightly different than the one with higher concentration. It has also been observed in other literature [16]. It can be observed that

prominent peaks can still be identified even when the concentration of R6G is down to 10^{-11} M, which is very close to single molecule detection if the confinement of incident field is considered.

6.4. Conclusion

The nanojet and surface enhanced Raman spectroscopy (NASERS) has been demonstrated. With the combination of optical confinement from nanojet and plasmonic amplification from nanostructured metal surface, the near field is significantly amplified according to the FDTD simulation results. This phenomenon is also experimentally demonstrated and the enhancement of combing nanojet effect with traditional SERS technique is calculated as 183 times. The low concentration detection of R6G has been performed and the detection limit is down to 10^{-11} M, which is near single molecule detection level. This setup provides a simple but effective method to boost the Raman enhancement on current SERS technique by two orders. This additional enhancement can be crucial for ultralow concentration detection such as single molecule detection by nanostructured solid SERS substrate.

6.5. Figures

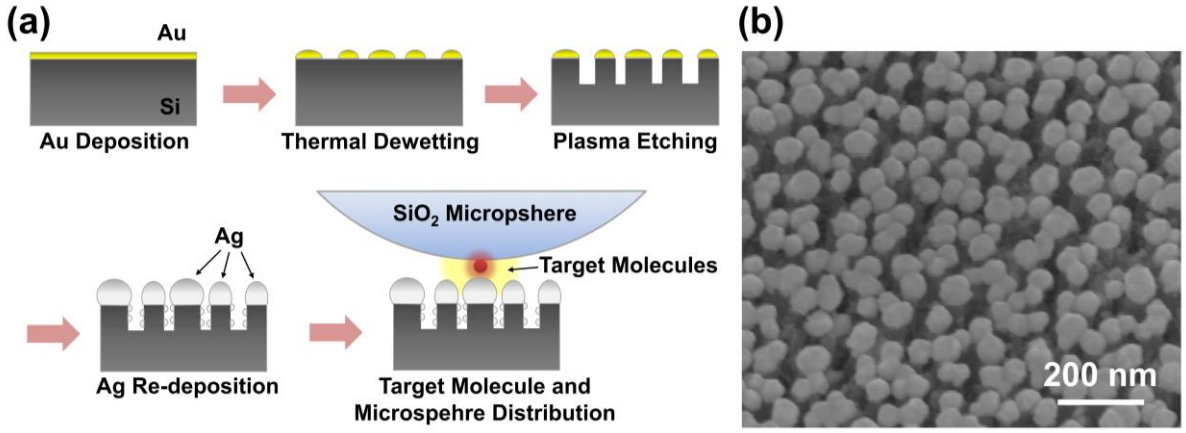

Figure 6.1 (a) Schematic of the NASERS setup preparation. (b) 30 degree tilted SEM images of nanostructured SERS substrate.

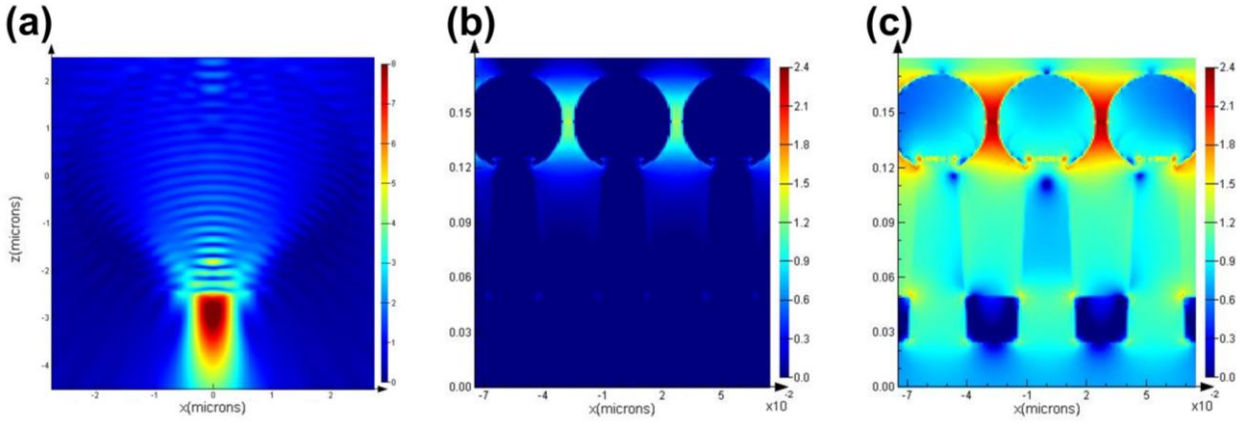

Figure 6.2 (a) Electric field distribution of nanojet confinement by propagating a Gaussian beam into a 5 µm SiO2 microsphere. (b) and (c) logarithm electric field distribution of nanostructured SERS substrate without and with the presence of microsphere.

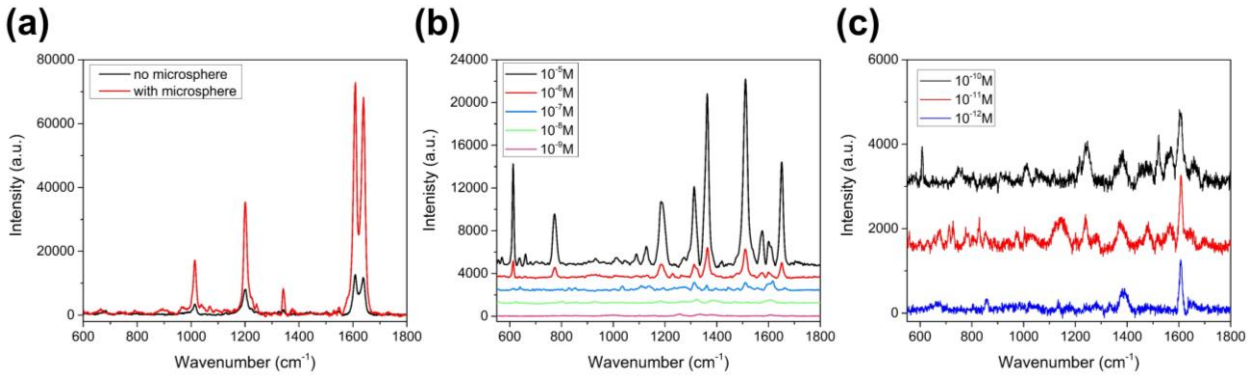

Figure 6.3 (a) The comparison of BPE Raman spectra with and without the presence of microsphere. (b) The Raman spectra of different concentration (10^{-5} to 10^{-9} M) measured with only nanostructured SERS substrate. (c) The Raman spectra of different concentration (10^{-10} to 10^{-12} M) measured with NASERS setup.

6.6. References

[1] Eigen, M.; Rigler, R. Sorting Single Molecules - Application to Diagnostics and Evolutionary Biotechnology. *Proc. Natl. Acad. Sci. U. S. A.* **1994**, *91*, 5740-5747.

[2] Nie, S. M.; Chiu, D. T.; Zare, R. N. Probing Individual Molecules with Confocal Fluorescence Microscopy. *Science* **1994**,*266*, 1018-1021.

[3] Goodwin, P. M.; Ambrose, W. P.; Keller, R. A. Single-Molecule Detection in Liquids by Laser-Induced Fluorescence. *Acc. Chem. Res.* **1996**, *29*, 607-613.

[4] Kneipp, K.; Wang, Y.; Kneipp, H.; Perelman, L. T.; Itzkan, I.; Dasari, R.; Feld, M. S. Single Molecule Detection using Surface-Enhanced Raman Scattering (SERS). *Phys. Rev. Lett.* **1997**, *78*, 1667-1670.

[5] Kneipp, K.; Kneipp, H. Single Molecule Raman Scattering. *Appl. Spectrosc.* **2006**, *60*, 322A-334A.

[6] Fan, M.; Andrade, G. F. S.; Brolo, A. G. A Review on the Fabrication of Substrates for Surface Enhanced Raman Spectroscopy and their Applications in Analytical Chemistry. *Anal. Chim. Acta* **2011**, *693*, 7-25.

[7] Campion, A.; Kambhampati, P. Surface-Enhanced Raman Scattering. *Chem. Soc. Rev.* **1998**, *27*, 241-250.

[8] Willets, K. A.; Van Duyne, R. P. Localized Surface Plasmon Resonance Spectroscopy and Sensing. *Annu. Rev. Phys. Chem.***2007**, *58*, 267-297.

[9] Qian, X.; Nie, S. M. Single-Molecule and Single-Nanoparticle SERS: From Fundamental Mechanisms to Biomedical Applications. *Chem. Soc. Rev.* **2008**, *37*, 912-920.

[10] Duan, H.; Hu, H.; Kumar, K.; Shen, Z.; Yang, J. K. W. Direct and Reliable Patterning of Plasmonic Nanostructures with Sub-10-Nm Gaps. *Acs Nano* **2011**, *5*, 7593-7600.

[11] Im, H.; Bantz, K. C.; Lindquist, N. C.; Haynes, C. L.; Oh, S. Vertically Oriented Sub-10-Nm Plasmonic Nanogap Arrays. *Nano Letters* **2010**, *10*, 2231-2236.

[12] Haynes, C. L.; Van Duyne, R. P. Plasmon-Sampled Surface-Enhanced Raman Excitation Spectroscopy. *J Phys Chem B***2003**, *107*, 7426-7433.

[13] Chen, Z. G.; Taflove, A.; Backman, V. Photonic Nanojet Enhancement of Backscattering of Light by Nanoparticles: A Potential Novel Visible-Light Ultramicroscopy Technique. *Optics Express* **2004**, *12*, 1214-1220.

[14] Devilez, A.; Bonod, N.; Wenger, J.; Gerard, D.; Stout, B.; Rigneault, H.; Popov, E. Three-Dimensional Subwavelength Confinement of Light with Dielectric Microspheres. *Optics Express* **2009**, *17*, 2089-2094.

[15] Dantham, V. R.; Bisht, P. B.; Namboodiri, C. K. R. Enhancement of Raman Scattering by Two Orders of Magnitude using Photonic Nanojet of a Microsphere. *J. Appl. Phys.* **2011**, *109*, 103103.

[16] Choi, C. J.; Xu, Z.; Wu, H.; Liu, G. L.; Cunningham, B. T. Surface-Enhanced Raman Nanodomes. *Nanotechnology***2010**, *21*, 415301.

CHAPTER 7 BIFUNCTIONAL NANO LYCURGUS CUP ARRAY (NANOLCA) PLASMONIC SENSOR FOR SURFACE ENHANCED RAMAN SPECTROSCOPY AND COLORIMETRIC SENSING BY NANOIMPRINT REPLICA TECHNIQUE

7.1. Introduction

Label-free detection has been widely recognized as a promising next-generation sensing method to replace the traditional current labeling detection in chemical analysis, biological sensing and drug screening. It provides the significant advantage of eliminating the need for tags or dyes to reduce possible interference with the probed molecule. In the past few decades much work has been devoted to this area and various approaches have been explored. One popular approach is based on measuring the resonance peak wavelength shift (PWS) when the probed molecule appears in the proximity of sensor, which modulates the resonance condition. PWS based sensors include photonic crystal [1], whispering gallery mode (WGM) [2] and surface plasmon resonance (SPR) in Kretschmann configuration [3]. Many different kinds of analyte such as DNA bases, antigen-antibody and immunoassays have been successfully detected under such configuration. However, the range of the peak wavelength shift of most PWS sensors is limited to the order of few nanometers. As a result, complicated and specialized instruments such as multiplexer, high accuracy spectrometer or complex optical system are necessary in order to obtain desired information. Sensors based on LSPR have been applied to label-free sensing application as well; these usually consist of nano-scale metal colloidal which processes LSPR resonance at visible range (e.g. silver or gold) [4]. By the aggregation of colloidal with the targeted analytes, the LSPR peak will experience a shift (usually towards longer wavelength). The ease of instrumental demand reveals its value and has drawn researchers' attention. Nevertheless, the sensitivity is slightly lower the transitional SPR sensor in Kretschmann configuration by approximately one order [5]. Besides,

the non-uniformity of metal colloidal conjugation results in difficulties of quantitative measurement [4].

Another approach is based on a periodic sub-wavelength structure with optically thick metal deposition as plasmonic active layer, which is well known as an extraordinary transmission (EOT) device [6-7]. The highly ordered structure is usually fabricated through a costly and time-consuming direct writing technique. In addition, the multiple resonance peaks from current EOT devices usually require further analysis from spectrometer system and hinder straightforward detection by naked eye or simple microscope [6]. Quasi-3D plasmonic crystals improve sensitivity of EOT sensors by applying multiple metal layers onto the structure [8]. However, most of this type of sensor have only been demonstrated in the range of near infrared or far infrared. Also there is no obvious resonance shift that can be observed when the absorption of analytes happens, which results in the difficulty of analyte detection or quantification.

Recently, the nano Lycurgus cup array (nanoLCA) plasmonic sensor has been demonstrated to offer its advantages in refractive index sensing [9]. Unlike most other EOT sensors, which are fabricated by expensive and time-consuming processes such as focused ion beam milling or electron beam lithography, the fabrication of nanoLCA is based on large-area and cost-effective nanoreplica technique. Besides, the huge absolute peak wavelength shift from nanoLCA opens an opportunity for colorimetric sensing by simple microscopic system or naked eye instead of applying complicated spectroscopic system. Although nanoLCA has shown its significant advantages on plasmonic colorimetric sensing, its application is still limited by the nature of refractive index sensing technique: high purity of sensing environment is required and the probing molecule must be identified beforehand; otherwise the undesired interference from impurities may lead to false positive or readout error for quantitative measurement. Although the surface

functionalization can increase the specificity to the targeted molecule, it requires specialized laboratory facilities and professional personnel to perform time-consuming and multi-step procedures. As a result, it is not suitable in point-of-care or resource-limited environments.

In contrast, Raman spectroscopy is able to precisely identify chemical molecules by their distinctive molecular vibrational modes. Moreover, surface enhanced Raman spectroscopy (SERS) greatly extends this capability to ultralow concentration detection. SERS has been performed on several devices which have similar configuration as nanoLCA such as nanohole array and quasi-3D devices. However, the Raman enhancements of these devices are moderate (~10^3 to 10^6) compared to other SERS substrates and they do not easily to meet the practical requirement of detection at lower analyte concentration [10-13].

In this chapter, we demonstrate the bifunctional property of nanoLCA, which possesses combined colorimetric sensing and SERS capability. A similar idea of multifunctional plasmonic sensor has been reported in other literature; however, none of those devices has satisfactory performance with both refractive index sensing and SERS for practical applications [14-15]. The simulated and experimental results presented here show that the unique configuration of nanoLCA, which is a combination of periodic quasi-3D nanostructure array pattern and dense sidewall metallic nanoparticles, enables both high sensitivity and sharp resonance peak in refractive sensing. In addition, we demonstrate the highest Raman enhancement from nanoLCA device compared with any other reported periodic EOT based devices in liquid sensing environment. This dual functionality of nanoLCA shows great potential to provide a sensing platform which can rapidly screen large amounts of liquid samples by colorimetric sensing with minimum sample preparation and facility requirement. Consequently, the SERS can perform molecule identification on selected

samples on the same device. It compensates for the deficiency of both low specificity on refractive index sensing and non-linearity on SERS molecule quantification.

7.2. Materials and methods

7.2.1. Nanoimprint replica technique

The schematic of nanoLCA fabrication process by nanoimprint replica technique is shown in figure 7.1 (a). The glass master mold consists of a nanocone array, which is fabricated by laser interference lithography [16]. The periodicity, height, and width of the nanostructure are 350, 500, and 200 nm. Before the nanoreplica process, the glass master mold was immersed into dimethyl dichlorosilane solution for 30 minutes. The mold was rinsed with DI water and ethanol to wash out extra molecules to form a monolayer of saline on the mold surface. This step is to achieve a hydrophobic surface for the master mold and to assist in the removal of cured polymer replica. About 10 µL UV-curable polymer (NOA-61) was evenly spread on the nanopillar surface. A 250 µm thick flexible polyethylene terephthalate (PET) sheet was used as a supporting substrate for the replica process. UV light-curing flood lamp system (Dymax EC-Series) was applied to provide constant UV light with power density of 105 $mWcm^{-2}$. The curing time was set as 60 seconds. After replication, metal deposition was implemented by CHA SEC-600 e-beam evaporator system. Thin layers of 9 nm titanium (Ti) and 90 nm silver (Ag) were deposited on the replicated device by electron beam evaporation. Ti was used as an adhesive layer to tightly bond Ag to the polymer substrate. The power of electron beam was set at 10 kV and operating base pressure was around 10^{-7} Torr. The deposition rate was controlled at 1 Å/s to ensure surface uniformity.

7.2.2. FDTD simulation

The numerical simulations of optical characteristics were studied by using three dimensional finite-difference time-domain (3D-FDTD) method with FDTD software package from Lumerical Solutions, Inc. The x-axis polarized electromagnetic wave was set to propagate normal to the substrate (-z direction) for reflection, transmission, and near-field simulations. Perfect matching layer (PML) was applied to the boundary conditions in z axis to eliminate any interference from the boundaries. In addition, PML and periodic boundaries were applied at x and y axes for simulating single and array nanostructure respectively. The near-field simulation observed in this paper is at x-z plane where y = 0. The mesh size was set as 1.5 nm and the total FDTD simulation region was 350 nm × 350 nm × 1000 nm.

7.2.3. Optical characteristic

The optical images were collected by Olympus BX51 Upright Fluorescence Microscope equipped with a mercury lamp in the Micro and Nanotechnology Laboratory, University of Illinois at Urbana-Champaign. The microscope was set at bright field mode without applying any filter. The light was focused onto the sample with 20X (NA = 0.45) objective lens. The transmission and reflection spectra were collected by the same microscopy setup with USB2000+ Fiber Optic Spectrometer by Ocean Optics. The detection wavelength range is from 200 to 1100 nm and the spectral resolution is up to 0.3 nm FWHM. The extinction spectrum shown here is defined as the subtraction from the measured transmission and reflection spectrum.

7.2.4. Raman spectroscopy measurement

Renishaw PL/Raman micro-spectroscope system was applied in this for SERS signal measurements. 633 nm He-Ne lasers are used as excitation light source. 20X objective lens (NA = 0.45) was used to focus/collect incident light and Raman signal onto/from the surface of

nanoLCA plasmonic sensor. The range of collected wavenumber was from 200 to 2000 cm^{-1}. The acquisition times for the nanoLCA plasmonic device and Klarite SERS substrate are 10 and 30 seconds. Every spectrum shown in this chapter is the average value measured from five different spots.

7.2.5. Image analysis

The filtered color images of nanoLCA device were taken by the same microscope system mentioned in optical characterization section at 20X magnification with exposure time of 50 ms (gain = 1; gamma = 1). FTIC fluorescence emission filter was applied, which enables a narrow passing wavelength band from 505 to 535 nm. Each image contains three 8-bit channels of red, green and blue. The image analysis was done by ImageJ software. For the calculation, an area of 512 × 512 pixels was selected to remove the boundary areas.

7.3. Results and discussion

7.3.1. Morphology observation

The images of scanning electron microscopy (SEM) are shown in figure 7.1(b) and (c). It can be clearly observed that nanoLCA holds high uniformity after the replication process and each nanocup contains a top Ag layer and bottom Ag nanodisk, which is similar to quasi-3D device [15]. Moreover, due to the unique cup-shaped profile of nano Lycurgus cup, a dense array of sub 50 nm Ag nanoparticles was formed on the sidewall after metal deposition.

7.3.2. Optical characterization

In order to understand the plasmonic property of nanoLCA device, a 3D-finite-difference time-domain (FDTD) method was applied to simulate the optical characterization based on this configuration. First, Ag plane thin film, single and periodic cup-shaped nanostructures (profile is the same as nano Lycurgus cup) with only top Ag layer were compared to identify the resonance peaks. The thickness of the top Ag layer in all the geometries was kept the same at 90 nm. Figure 7.2 shows the transmission spectra of all three configurations and the cross-section z-direction electric field (E_z) distribution of periodic cup-shaped nanostructure with top Ag layer at the wavelengths of 354, 455, and 644 nm. All three transmission spectra exhibit resonance peak at 320 nm, which is related to bulk plasma of Ag [17]. Additional peak at 354 nm appears in both single and periodic nanostructures. According to the electric field distribution at 354 nm, the strong electric field is focused on the upper rim edge of the top Ag layer, which indicates that this peak is due to LSPR [18]. On the other hand, peaks at 455 and 644 nm are only found in the periodic case. Moreover, the cross-section electric fields at both wavelengths are focused at the interface of air-Ag and Ag-substrate, which is the signature pattern of SPR mode [19]. Therefore these two peaks can be identified as surface plasmon polariton-Bloch wave modes (SPP-BW) [20-22]. Peaks at 455 and 644 nm are related to (1,0) mode at air-Ag and Ag-substrate interface respectively. Other literature has also identified these two modes at similar wavelengths for the periodic nanostructured device with the same periodicity [23].

Based on previous analysis, the resonance peaks from cup-shaped nanostructure array with top Ag layer are identified. However, comparing to the actual nanoLCA configuration, some important structural components of nanoLCA such as the bottom Ag nanodisk and sidewall Ag nanoparticles are not included yet. Hence, a step-by-step analysis of adding these components was performed to

understand the unique configuration of nanoLCA and its resonance conditions. The study will elucidate the mechanism of nanoLCA resonance compared to other EOT devices. The simulation model of nanoLCA was based on the observation of SEM images and shown in figure 7.3 (a). Since in reality the sidewall Ag nanoparticles are randomly distributed, different diameters (D) of sidewall Ag nanoparticle (D = 30, 40, and 50 nm) were simulated to match the measurement data as shown in figure 7.3 (b). We modelled the sidewall Ag nanoparticles to be in 4 rows and evenly distributed in height. In each row there were 8 nanoparticles as observed in the SEM images. From the simulation results, Ag nanoparticles with the diameter of 40 nm on the sidewall matched the experimental data the best and were applied in the following analysis.

Figure 7.3 (c) depicts the transmission spectra through the same periodic cup-shaped nanostructure but with different Ag components. Spectra A, B, C, and E are simulated transmission spectra with top Ag layer, bottom Ag nanodisk, quasi-3D configuration (refers to the combination of top Ag layer and bottom Ag nanodisk), and nanoLCA configuration respectively. The scattering spectrum of only sidewall Ag nanoparticles is also included in the figure as spectrum D. It can be observed that the resonance peaks from top Ag layer only (spectrum A) and bottom Ag nanodisk only (spectrum B) are coupled to form multiple resonance peaks at 438, 463, and 495 nm in quasi-3D configuration (spectrum C). This phenomenon of coupled resonance was observed in other literature as well [24-25]. However, when the sidewall Ag nanoparticles are taken into consideration, the scattering from sidewall Ag nanoparticles (spectrum D) is in the same spectral range as coupled resonance peaks of quasi-3D configuration. As a result, a single and sharper resonance peak with full wave half maximum (FWHM) of ~50 nm compared to traditional nanohole array configuration (refers to spectrum A in the figure with FWHM of ~100 nm) are

formed and plotted in spectrum E. This sharper FWHM is beneficial for refractive index sensing providing better FOM as well as in the image analysis of colorimetric sensing.

The comparison of transmission spectra between simulated and experimental data is shown in figure 7.4 (a). Air (n = 1) and water (n = 1.333) superstrates, which were defined as the dielectric material above the nanoLCA device, were examined and presented in the figure. The logarithmic electric field intensities of corresponding resonance peaks are shown in figure 7.4 (b). In general, the simulated model predicts the actual optical phenomenon very well despite minor resonance offsets at longer wavelength with water superstrate (610 nm in experiment and 592 nm in simulation). From the electric field intensity diagrams, it can be seen that peaks (i) and (iii) are in the same resonance mode in different superstrates, where the electric field is mainly focused at the upper edge of top Ag layer and the first row of sidewall Ag nanoparticles. On the other hand, peaks (ii) and (iv) are in the same resonance condition since the electric field patterns are the same and have strong coupling among sidewall Ag nanoparticles. This can also explain the minor resonance offset at longer wavelength with water superstrate mentioned before: the difference between the simulated and measured spectra of the nanoLCA may be due to the limitations in the simulation software to accurately represent the quasi-random spatial distribution of sidewall Ag nanoparticles.

7.3.3. Characterization of colorimetric sensing performance

To characterize the colorimetric sensing performance of nanoLCA, glycerol solutions with different wt% concentrations (0, 3, 10, 20, 30, and 40%) were used to vary the refractive index of superstrate covered on nanoLCA. The measured results of transmission spectra are shown in figure 7.5 (a). It can be observed that the resonance peaks were red-shifted when the refractive index of superstrate increased. 3D-FDTD simulation with the same condition is shown in figure 7.5 (b). From the simulation, the wavelength shift of resonance peaks is consistent with the measurement

results. Figure 7.5 (c) depicts the peak resonance shift with respect to the refractive index change of superstrate by analyzing the resonance peak at shorter wavelength (refer to the peak at 465 nm with 0% concentration of glycerol). The sensitivity ($\Delta\lambda/\Delta n$, λ is the wavelength and n is the refractive index) was calculated to be 796 nm/RIU by using linear curve fitting method. The maximum figure of merit ($FOM = sensitivity/\Delta w$, where Δw is the FWHM of the peak inconsideration) is calculated as 12.7 with the FWHM width of 62.55 nm at that resonance peak. The corresponding bright field optical images of the spectral measurement are shown in figure 7.5 (d) and demonstrate the colorimetric sensing capability of nanoLCA with simple microscope setup. As the concentration of glycerol increased, the color of transmission optical image became more reddish, which is consistent with the red-shifting phenomenon in the experimental transmission spectrum results.

7.3.4. Characterization of SERS performance

The surface enhanced Raman spectroscopy (SERS) capability of the nanoLCA device was analyzed by applying a monolayer of 1,2-bis(4-pyridyl)ethylene (BPE, Sigma-Aldrich, 99%) as the probing molecule. Firstly the nanoLCA devices were immersed in 5 mM BPE ethanolic solution for 24 hours and then rinsed with pure ethanol solution in order to wash out extra BPE molecules stacked on the surface. Finally devices were blown with nitrogen gas to completely dry. Figure 7.6 (a) shows the extinction spectra of nanoLCA device with air and water superstrates. It can be observed that nanoLCA exhibits higher absorption at 633 nm in water than in air, which indicates the resonance should be stronger in water with the excitation wavelength at 633 nm. As shown in figure 7.6 (b), the simulated logarithmic electric field intensity with water superstrate also possesses much stronger near field than the case in air, especially among the sidewall Ag nanoparticles. The simulated results further prove that the nanoLCA device is optimized for liquid

SERS detection with 633 nm excitation wavelength. Figure 7.6 (c) shows the Raman spectra of BPE on nanoLCA in both air and water. For comparison, commercially available Klarite SERS substrate (Klarite KLA-313, D3 Technologies Ltd., UK) was measured with the same treatment and the result is included in the figure as well. All spectra show characteristic Raman peaks of BPE at 1020, 1200, 1340, 1607 and 1637 cm^{-1}. It can be observed that the Raman enhancement is approximately 20 times higher when nanoLCA is covered with water than with air after normalization of excitation laser power, which matches the trend that nanoLCA exhibits higher resonance with water superstrate from the results of extinction spectra and FDTD simulation. Furthermore, nanoLCA device under solution-based detection environment provides 148 and 107 times better performance than the commercially available Klarite SERS substrate with air and water as superstrate. The minor Raman signal improvement of Klarite SERS substrate in water compared to air can be attributed to the low resonance peak shift with respect to refractive index change [26]. The enhancement factor (EF) is estimated by the integration of peak intensity at 1607 cm^{-1} with respect to the bulk BPE solution and calculated to be 2.8×10^7. (The information of EF calculation can be found in Appendix A.) This is so far the highest SERS enhancement achieved compared to other EOT devices such as nanohole array or quasi-3D devices. (The list of SERS performance compared to other similar EOT devices can be found in table 7.1). In addition, most of the SERS performances from other devices were characterized and optimized under dry-state measurement; however most of the chemical or biological molecules exist in solution-based environment. Therefore, the actual SERS performance from those devices might be lower with the application of solution-based measurement. The nanoLCA device shows its great advantage for *in-vivo* SERS detection or rapid SERS testing with minimal sample preparation time (no waiting time to dry the sample); at the same time, it possesses comparable sensitivity in refractive index

sensing compared to other types of plasmonic sensor. To examine the uniformity of SERS performance of nanoLCA device, a mapping of SERS spectra on nanoLCA was performed and the peak intensity at 1607 cm^{-1} is shown in figure 7.6 (d). The total mapping is carried out on an area of 1 mm × 1 mm and measured at a spacing of 100 µm. The averaged intensity of total measured data was set as baseline (0% in the figure) to estimate the uniformity of spatial SERS performance. The relative standard deviation (RSD) was calculated as 10.2 %, which demonstrates the high spatial uniformity of nanoLCA device in SERS detection for quantitative measurement.

7.3.5. Detection of urea concentration

In this section the detection of urea concentration was demonstrated as a proof-of-concept to show the potential of utilizing the dual functionality of nanoLCA for diagnostics in resource limited environments: on-site plasmonic colorimetric screening can be performed with ordinary bright field microscopy to rapidly select out the samples of interest (without specificity). This sample-screening process requires minimum laboratory facility, sample preparation, and professional personnel. Later on the selected samples can be further analyzed for identification of the molecules with high specificity by Raman spectroscopy with the same nanoLCA plasmonic device. This complementary two-step analytical procedure provides a sensing platform with high speed, sensitivity and specificity while minimizing the probability of false positives.

Urea is one of the major components in urine and plays a significant role in maintaining fluid and electrolyte balance in the body [27]. Urea concentration in urine is directly related to the amount of protein intake. Sudden decrease of urea concentration indicates protein breakdown, which is a sign of acute kidney failure, malnutrition and severe liver damage. Figure 7.7 demonstrates the results of both colorimetric and Raman spectroscopy detection of urea concentration by nanoLCA plasmonic device. Ordinary bright field microscopy (with filters) was

used to take optical images with different concentrations of urea solution (0, 25, 50, 100, 250, 500, 750 and 1000 mM). All the images were taken with FITC emission filter, which only allows the light between 505 and 535 nm to be captured by the CCD camera. This step is able to avoid the interference from incident light within other wavelengths. As shown in the inset of figure 7.7 (a), when the urea concentration increases, the resonance peak experienced red shift due to the increase of refractive index. As a result, the total intensity within FITC filtered range will be increased accordingly. Figure 7.7 (a) shows the averaged green-channel intensity extracted from images with respect to urea concentration. The relationship curve fits the Langmuir equation since urea has strong adsorption to the silver surface [28]. The results of Raman spectroscopy are shown in figure 7.7 (b) with the same concentrations of urea as used in the colorimetric measurements. All spectra show the dominant peak at 708 cm^{-1}, which is π_{CO} vibrational mode when the urea is adsorbed on the silver surface. With the concentration higher than 500 mM, peaks at 1007 and 1145 cm^{-1} can be observed, which are related to Raman peaks from bulk urea molecules [29]. The plot of peak intensity at 708 cm^{-1} with respect to different concentrations of urea is shown in the inset of figure 7.7 (b). The intensity curve also fits the Langmuir equation and further validates the results obtained from colorimetric measurement. This experiment proves the concept of utilizing the capability of molecule identification from SERS to increase the specificity of the refractive index sensing, while the colorimetric screening process can quickly recognize the targeted sample with minimum sample preparation. Most of all, these two sensing methods can be directly performed on the very same device without any modification.

7.4. Conclusion

In summary, a bifunctional nanoLCA plasmonic device has been developed and demonstrated for both colorimetric and SERS sensing. Proved by both simulation and experiments, the unique configuration of nanoLCA, which contains periodic quasi-3D nanostructure and dense Ag sidewall nanoparticles, leads to sharper FWHM (~50 nm) compared to traditional nanohole array device (~100 nm). The sensitivity was calculated as 796 nm/RIU with the FOM of 12.7 and the capability of utilizing nanoLCA for colorimetric sensing has been performed as well. In addition, the Ag sidewall nanoparticles contribute to strong coupling and enable the nanoLCA device to be optimized for SERS measurement under the solution-based environment, where most biological and chemical analyses are typically performed. The SERS EF was calculated as 2.8×10^7 in a solution based environment with 10.2 % RSD, which is so far the highest reported SERS enhancement achieved with similar periodic EOT devices. Finally, the detection of urea concentration has been demonstrated as proof-of-concept of the two-step sensing process, which enables rapid on-site screening and further molecule identification.

7.5. Figures and table

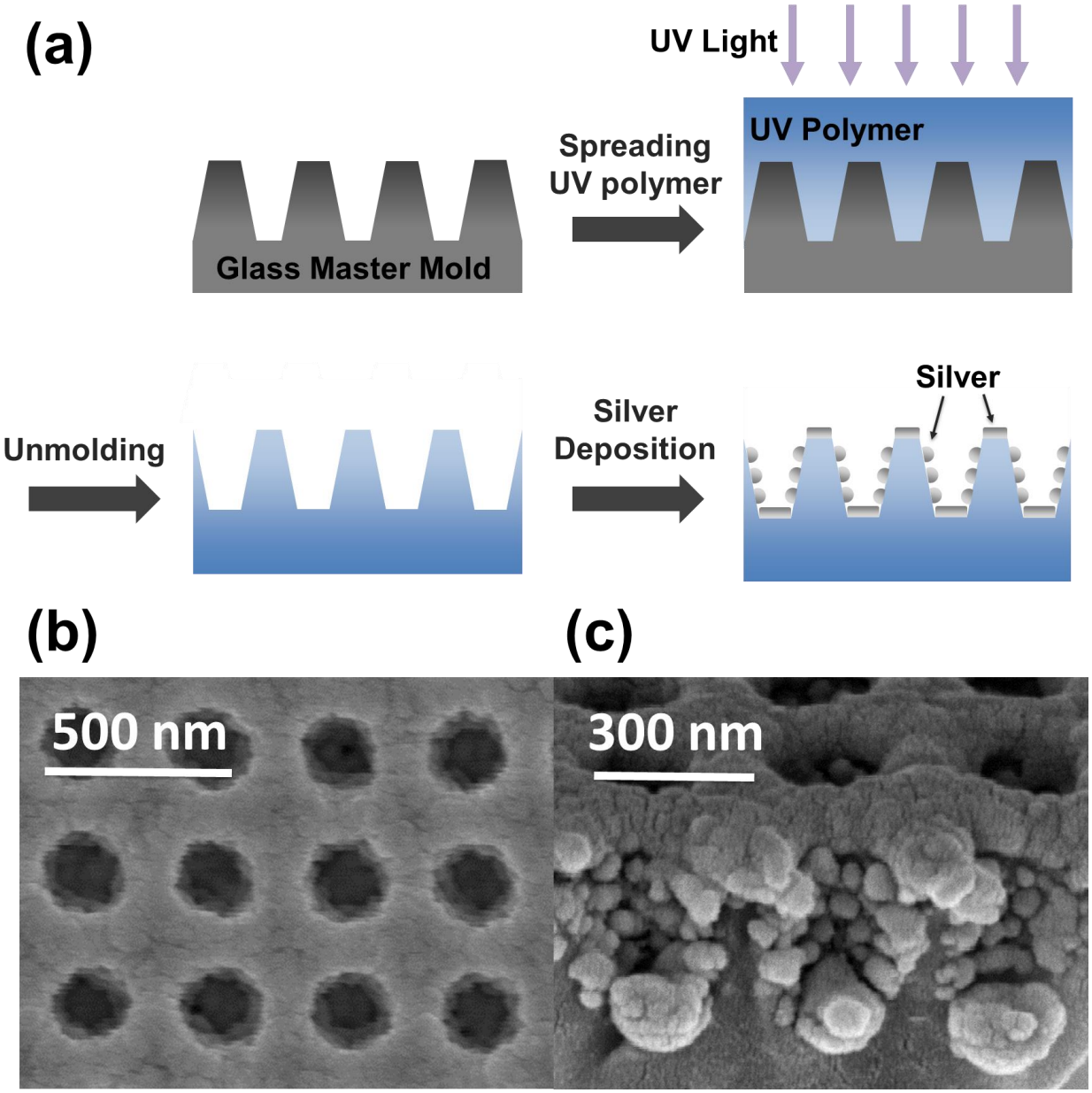

Figure 7.1 (a) Schematics of nanoLCA plasmonic sensor fabrication. (b) Top side and (c) 60° tilted angle view SEM images of nanoLCA plasmonic sensor fabrication.

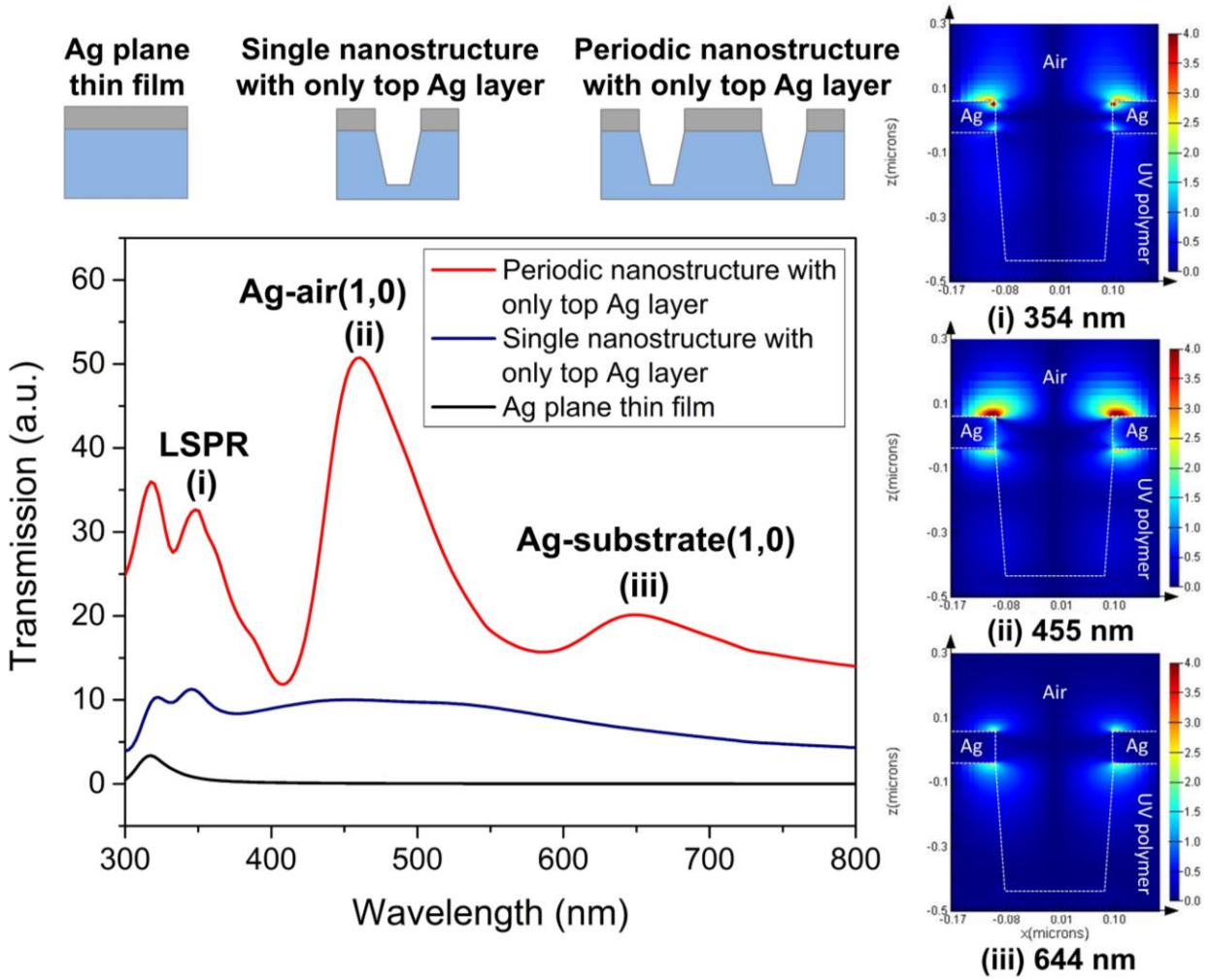

Figure 7.2 Simulated transmission spectra of Ag plane thin film, single and periodic cup-shaped nanostructure with only top Ag layer. The thickness of Ag layer all kept as 90nm. The simulations of z-direction electric field (E_z) of periodic cup-shaped nanostructure with top Ag layer at 354, 455, and 644 nm are included in the figure.

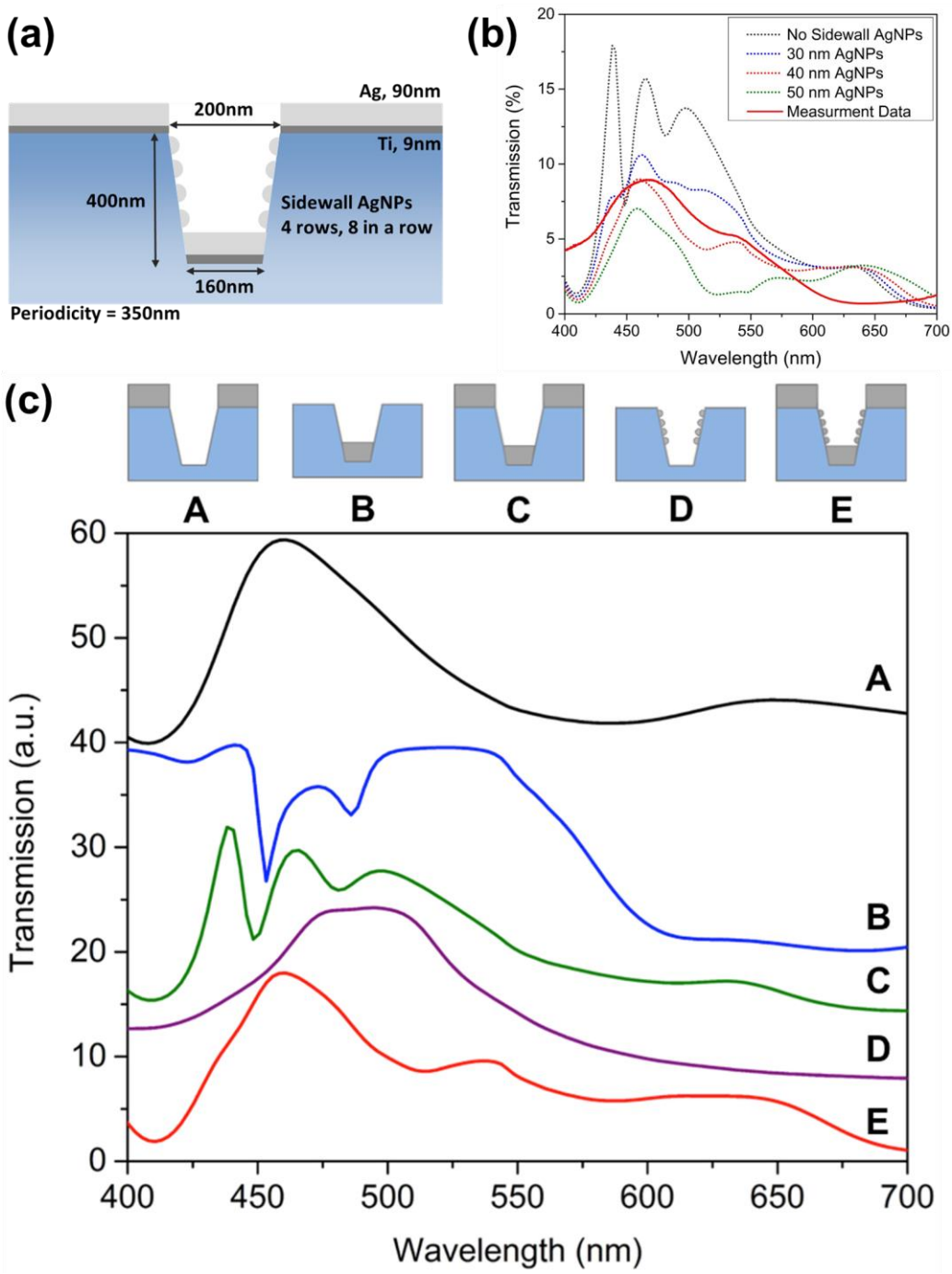

Figure 7.3 (a) Simulation model of nanoLCA plasmonic sensor. (b) Simulated transmission spectra of nanoLCA with no sidewall Ag nanoparticles and different sizes of sidewall Ag nanoparticles (diameter = 30, 40, and 50 nm). The measured transmission spectrum of nanoLCA is shown in the figure as well for comparison. (c) Simulated transmission spectra of periodic cup-shaped nanostructure with (A) top Ag layer, (B) bottom Ag nanodisk, (C) quasi-3D configuration, (E) actual configuration of nanoLCA. Scattering spectrum of only sidewall Ag nanoparticles is plotted in this figure as spectrum D.

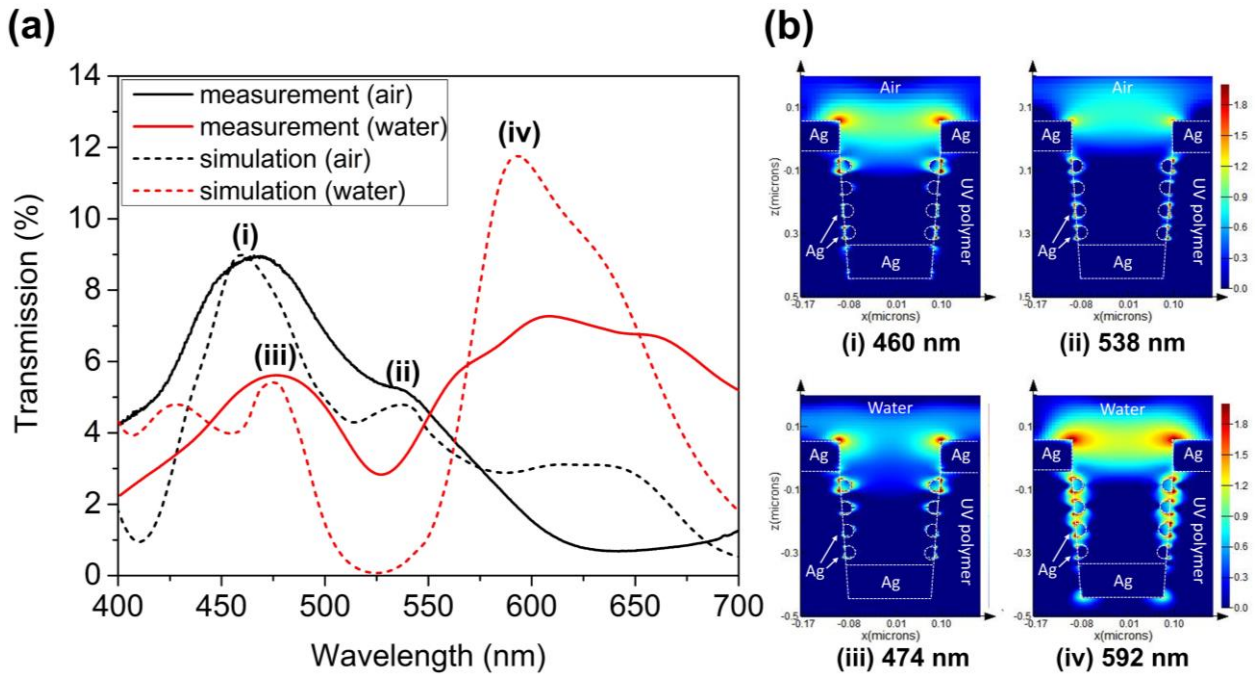

Figure 7.4 (a) Comparison of simulated and measured transmission spectra of nanoLCA covered with air and water. (b) Logarithmic electric field intensity of nanoLCA at 460 and 538 nm with air (i and ii) and 474 and 592 nm with water (iii and iv).

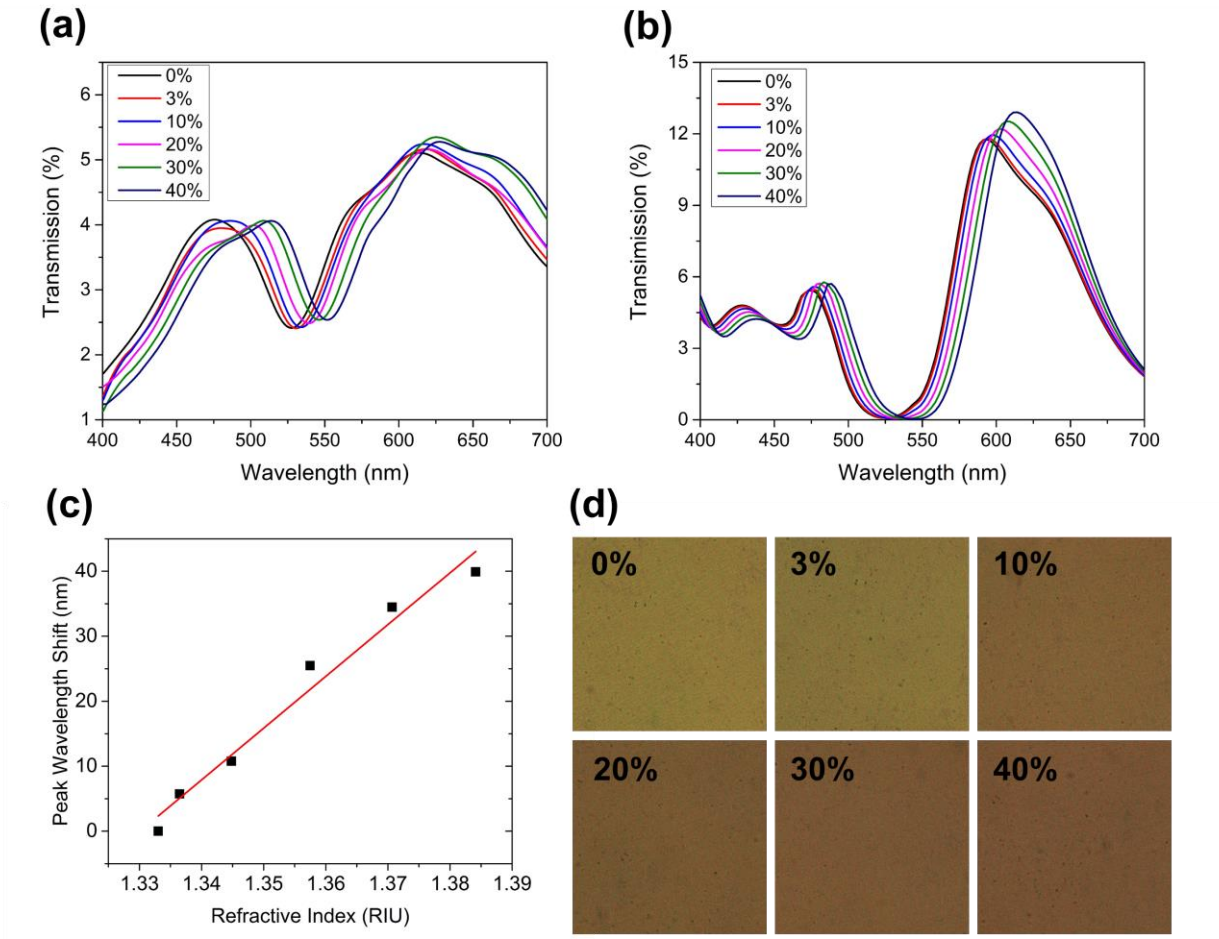

Figure 7.5 (a) Measured and (b) simulated transmission spectra of nanoLCA covered with different wt% concentrations of glycerol (0, 3, 10, 20, 30, and 40%). (c) Sensitivity of nanoLCA calculated for glycerol concentration range from 0-40%. The sensitivity was calculated as 796 nm/RIU. (d) Optical images of different wt% concentrations of glycerol on nanoLCA.

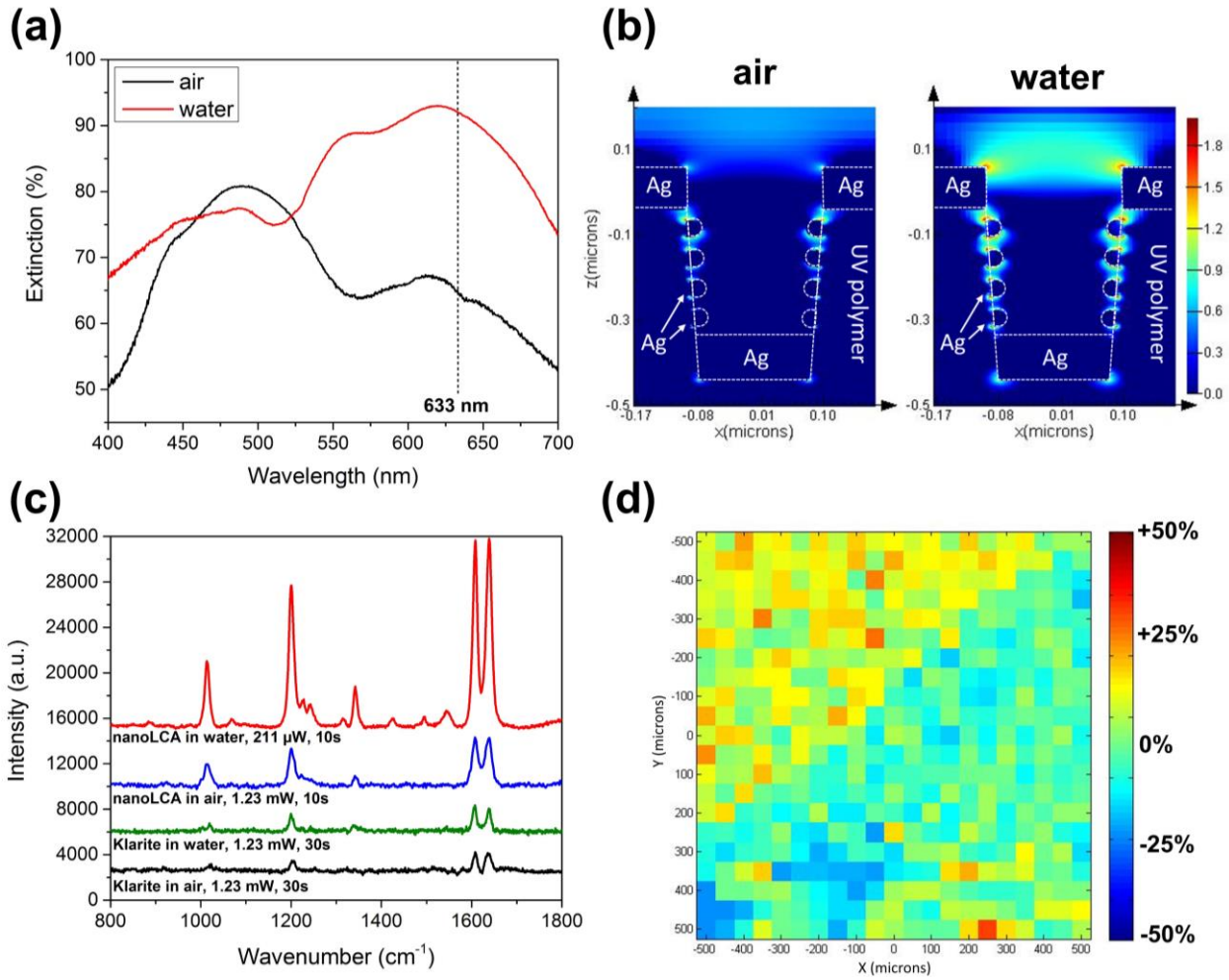

Figure 7.6 (a) Extinction spectra of nanoLCA covered with air and water. (b) The logarithm electric field intensity of nanoLCA with supertrates of air and water. (c) Raman spectra of BPE on both nanoLCA and commercially available Klarite SERS substrate covered with air and water. (d) Mapping of Raman intensity at 1607 cm^{-1} of BPE on nanoLCA at excitation wavelength 633 nm. The total mapping is on area of 1 mm × 1mm and measured at every 100 µm distance.

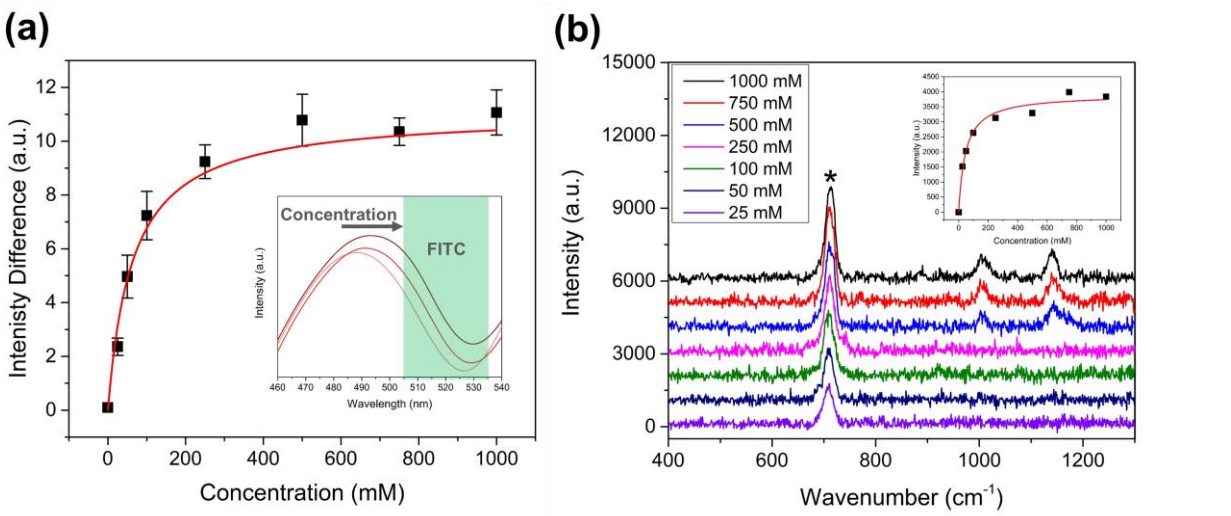

Figure 7.7 (a) Averaged green-channel intensity of nanoLCA device with different concentrations of urea. All images are taken with FITC filter applied. The inset figure demonstrates the shift of transmission spectrum when the concentration of urea becomes higher (25 to 100 mM in this example). The green shadow region represents the filtered band of FITC in spectrum. (b) Raman spectra of nanoLCA device with different concentrations of urea at 708 cm^{-1}.

Table 7.1 Comparison of SERS EF with different configurations of EOT devices.

Nanostructure	Structural Dimension (nm)	Excitation Laser Wavelength (nm)	Estimated EF	Ref.
Nano Lycurgus Cup Array	D = 200 H = 400 P = 350 T = 90 (Ag)	633	2.81×10^7	Present Study
Self-Assembled Nanohole Array with Plating Etching	D = 200 & 300 P = 400 & 600 T = 50 (Ag)	532	1.58×10^5	[10]
		633	3.26×10^6	
Quasi-3D nanostructure	D = 400 H = 300 P = 500 T = 50 (Au)	785	6.4×10^5	[11]
Nanohole Array	D = 370-645 P = 500-780 T = 50-200 (Au)	633	5.5×10^3 – 6.3×10^4	[12]
Nanoring Cavity	D = 370/216-645/317 (outer/inner) P = 500-780 T = 55 (Au)		1.3×10^5 – 3.1×10^5	
X-shaped quasi-3D nanostructure	H = 400 P = 520 T = 50 (Ag)	785	75 folds compared to Klarite SERS substrate	[13]
Nanopost Plasmonic Crystal	D = 170-1120 H = 360 P = 500-1750 T = 40 (Au & Ag)	785	~ 10^5 (Au) ~ 10^6 (Ag)	[30]

7.6. References

[1] Ganesh, N.; Zhang, W.; Mathias, P. C.; Chow, E.; Soares, J. A. N. T.; Malyarchuk, V.; Smith, A. D.; Cunningham, B. T. Enhanced Fluorescence Emission from Quantum Dots on a Photonic Crystal Surface. Nature Nanotechnology 2007, 2, 515-520.

[2] Vollmer, F.; Arnold, S. Whispering-Gallery-Mode Biosensing: Label-Free Detection Down to Single Molecules. *Nature Methods* **2008**, *5*, 591-596.

[3] Haes, A. J.; Van Duyne, R. P. A Unified View of Propagating and Localized Surface Plasmon Resonance Biosensors. *Analytical and Bioanalytical Chemistry* **2004**, *379*, 920-930.

[4] Ahamad, N.; Bottomley, A.; Ianoul, A. Optimizing Refractive Index Sensitivity of Supported Silver Nanocube Monolayers. *Journal of Physical Chemistry C* **2012**, *116*, 185-192.

[5] Kabashin, A. V.; Evans, P.; Pastkovsky, S.; Hendren, W.; Wurtz, G. A.; Atkinson, R.; Pollard, R.; Podolskiy, V. A.; Zayats, A. V. Plasmonic Nanorod Metamaterials for Biosensing. *Nature Materials***2009**, *8*, 867-871.

[6] Ebbesen, T. W.; Lezec, H. J.; Ghaemi, H. F.; Thio, T.; Wolff, P. A. Extraordinary Optical Transmission through Sub-Wavelength Hole Arrays. *Nature* **1998**, *391*, 667-669.

[7] Genet, C.; Ebbesen, T. W. Light in Tiny Holes. *Nature* **2007**, *445*, 39-46.

[8] Stewart, M. E.; Mack, N. H.; Malyarchuk, V.; Soares, J. A. N. T.; Lee, T.; Gray, S. K.; Nuzzo, R. G.; Rogers, J. A. Quantitative Multispectral Biosensing and 1D Imaging using Quasi-3D Plasmonic Crystals. *Proc. Natl. Acad. Sci. U. S. A.* **2006**, *103*, 17143-17148.

[9] Gartia, M. R.; Hsiao, A.; Pokhriyal, A.; Seo, S.; Kulsharova, G.; Cunningham, B. T.; Bond, T. C.; Liu, G. L. Colorimetric Plasmon Resonance Imaging using Nano Lycurgus Cup Arrays. *Advanced Optical Materials* **2013**, *1*, 68-76.

[10] Lee, S. H.; Bantz, K. C.; Lindquist, N. C.; Oh, S.; Haynes, C. L. Self-Assembled Plasmonic Nanohole Arrays. *Langmuir* **2009**, *25*, 13685-13693.

[11] Yu, Q.; Braswell, S.; Christin, B.; Xu, J.; Wallace, P. M.; Gong, H.; Kaminsky, D. Surface-Enhanced Raman Scattering on Gold Quasi-3D Nanostructure and 2D Nanohole Arrays. *Nanotechnology* **2010**, *21*, 355301.

[12] Ho, C.; Zhao, K.; Lee, T. Quasi-3D Gold Nanoring Cavity Arrays with High-Density Hot-Spots for SERS Applications Via Nanosphere Lithography. *Nanoscale* **2014**, *6*, 8606-11.

[13] Wang, D.; Yu, X.; Yu, Q. X-Shaped Quasi-3D Plasmonic Nanostructure Arrays for Enhancing Electric Field and Raman Scattering. *Nanotechnology* **2012**, *23*, 405201.

[14] Canpean, V.; Astilean, S. Multifunctional Plasmonic Sensors on Low-Cost Subwavelength Metallic Nanoholes Arrays. *Lab on a Chip* **2009**, *9*, 3574-3579.

[15] Potara, M.; Gabudean, A.; Astilean, S. Solution-Phase, Dual LSPR-SERS Plasmonic Sensors of High Sensitivity and Stability Based on Chitosan-Coated Anisotropic Silver Nanoparticles. *Journal of Materials Chemistry* **2011**, *21*, 3625-3633.

[16] Gartia, M. R.; Xu, Z.; Behymer, E.; Nguyen, H.; Britten, J. A.; Larson, C.; Miles, R.; Bora, M.; Chang, A. S.; Bond, T. C.; Liu, G. L. Rigorous Surface Enhanced Raman Spectral Characterization of Large-Area High-Uniformity Silver-Coated Tapered Silica Nanopillar Arrays. *Nanotechnology* **2010**, *21*, 395701.

[17] Chaturvedi, P.; Hsu, K. H.; Kumar, A.; Fung, K. H.; Mabon, J. C.; Fang, N. X. Imaging of Plasmonic Modes of Silver Nanoparticles using High-Resolution Cathodoluminescence Spectroscopy. *ACS Nano* **2009**, *3*, 2965-2974.

[18] Yue, W.; Yang, Y.; Wang, Z.; Han, J.; Syed, A.; Chen, L.; Wong, K.; Wang, X. Improved Surface-Enhanced Raman Scattering on Arrays of Gold Quasi-3D Nanoholes. *Journal of Physics D-Applied Physics* **2012**, *45*, 425401.

[19] Lindquist, N. C.; Nagpal, P.; McPeak, K. M.; Norris, D. J.; Oh, S. Engineering Metallic Nanostructures for Plasmonics and Nanophotonics. *Reports on Progress in Physics* **2012**, *75*, 036501.

[20] Chang, S. H.; Gray, S. K.; Schatz, G. C. Surface Plasmon Generation and Light Transmission by Isolated Nanoholes and Arrays of Nanoholes in Thin Metal Films. *Optics Express* **2005**, *13*, 3150-3165.

[21] Zhang, X.; Li, Z.; Ye, S.; Wu, S.; Zhang, J.; Cui, L.; Li, A.; Wang, T.; Li, S.; Yang, B. Elevated Ag Nanohole Arrays for High Performance Plasmonic Sensors Based on Extraordinary Optical Transmission. *Journal of Materials Chemistry* **2012**, *22*, 8903-8910.

[22] Brolo, A. G.; Gordon, R.; Leathem, B.; Kavanagh, K. L. Surface Plasmon Sensor Based on the Enhanced Light Transmission through Arrays of Nanoholes in Gold Films. *Langmuir* **2004**, *20*, 4813-4815.

[23] Degiron, A.; Ebbesen, T. W. The Role of Localized Surface Plasmon Modes in the Enhanced Transmission of Periodic Subwavelength Apertures. *Journal of Optics A-Pure and Applied Optics* **2005**, *7*, S90-S96.

[24] Stewart, M. E.; Mack, N. H.; Malyarchuk, V.; Soares, J. A. N. T.; Lee, T.; Gray, S. K.; Nuzzo, R. G.; Rogers, J. A. Quantitative Multispectral Biosensing and 1D Imaging using Quasi-3D Plasmonic Crystals. *Proc. Natl. Acad. Sci. U. S. A.* **2006**, *103*, 17143-17148.

[25] Auguie, B.; Barnes, W. L. Collective Resonances in Gold Nanoparticle Arrays. *Phys. Rev. Lett.* **2008**, *101*, 143902.

[26] Wu, H.; Choi, C. J.; Cunningham, B. T. Plasmonic Nanogap-Enhanced Raman Scattering using a Resonant Nanodome Array. *Small* **2012**, *8*, 2878-2885.

[27] Sands, J. M. Critical Role of Urea in the Urine-Concentrating Mechanism. *Journal of the American Society of Nephrology* **2007**, *18*, 670-671.

[28] Lukomska, A.; Sobkowski, J. Adsorption of Urea on a Polycrystalline Silver Electrode; Comparison of Electrochemical and Radiometric Methods. *Journal of Solid State Electrochemistry* **2005**, *9*, 277-283.

[29] Moskovits, M.; Suh, J. S. The Geometry of several Molecular-Ions Adsorbed on the Surface of Colloidal Silver. *J. Phys. Chem.* **1984**, *88*, 1293-1298.

[30] Baca, A. J.; Montgomery, J. M.; Cambrea, L. R.; Moran, M.; Johnson, L.; Yacoub, J.; Truong, T. T. Optimization of Nanopost Plasmonic Crystals for Surface Enhanced Raman Scattering. *Journal of Physical Chemistry C* **2011**, *115*, 7171-7178.

CHAPTER 8 DEVELOPMENT OF OPTO-MICROFLUIDIC AND SMARTPHONE BASED PLATFORM FOR BIFUNCTIONAL NANOLCA PLASMONIC DEVICE APPLICATION

8.1. Introduction

In chapter 7, a novel and promising bifunctional sensing system has been proposed and demonstrated to show its potential on complementary rapid screening and precise identification sensing platform within the same device. Here the development of an opto-microfluidic and smartphone based platform is demonstrated as the fundamental hardware component of the bifunctional sensing platform for future potential applications.

8.2. On-chip bifunctional opto-microfluidic nanoLCA platform

Traditional labels such as fluorophores, chromophores, or radioactive labels are widely used in microfluidic applications to visualize flow [1] or detect the presence or concentration of relevant species [2-3]. However, each of these labels has shortcomings including bleaching of fluorophores, non-specificity of chromophores, and steric blocking of conjugated labels [4-6]. In particular in microfluidics, labeling with multiple dyes may suffer from the low Reynolds number laminar flow and when introduced at high concentration, may alter the physical properties of the flow solution. Label-free detection based on optical techniques has revolutionized the ability to detect a broad range of biological samples, such as protein-protein interaction and DNA hybridization, simply based on the intrinsic dielectric permittivity of samples without the need for labeling [7-9]. Due to the unique transmission/reflection peak wavelengths of nanoLCA in the visible wavelength range, visible colorimetric changes can be demonstrated simply due to the changes in the refractive index on and near the surface of the sensor upon the changes of the presence or the concentration of the

sample of interest. The capability of nanoLCA to on-chip applications by integrating relevant microfluidic designs, such as parallel flow channels and droplet generator, is demonstrated in this section by demonstrating colorimetric visualization of static and transient dynamics of optically-transparent solutions, which previously could not be visualized in a colorimetric manner.

Since the PDMS-based microfluidic device comes into contact with the gold-coated surface of nanoLCA, the traditional bonding technique of oxygen plasma treatment is not sufficient to create a strong bond between the two substrates. The integration of the nanoLCA with the microfluidic device was accomplished using a "stamp and stick" method [6], which utilizes a UV-curable optical adhesive to act as an adhesive layer between the PDMS-based microfluidic device and the nanoLCA substrate as shown in figure 8.1 (a). A thin layer of UV-curable optical adhesive (Norland 61, Norland Products, NJ, USA) is formed on a flat substrate by spin-coating at 6000 RPM for 120 seconds. The PDMS mold with microfluidic design is brought into contact with the thin layer of UV-curable polymer adhesive for 30 seconds. Then the PDMS substrate with microfluidic design is removed and subsequently brought into contact with the nanoLCA substrate. The bonded PDMS-nanoLCA substrate is exposed to UV lamp for five minutes and then placed on a hot plate set at 65°C for 12 hours for adhesive aging. The bonding between the nanoLCA substrate and the microfluidic PDMS substrate has withstood flow rates up to 30 µL min-1 without any leaks or delamination and is compatible with different solvent types including mineral oil and deionized water. The UV-curable adhesive based bonding is a facile process in terms of required equipment and processing time relative to oxygen plasma treatment. Static spectral and optical colorimetric characterization of microfluidic nanoLCA was performed using a parallel-channel microfluidic device bonded to the nanoLCA substrate as shown in figure 8.1 (c). The parallel-channel design (width: 500 µm, height: 200 µm) allows for maximal area usage of the nanoLCA

substrate by accommodating multiple solutions on a single device, with minimal volume of sample needed (~ 100 nL).

To demonstrate real-time colorimetric sensing and spatial localization of different refractive indices with nanoLCA, we chose two solutions (water and mineral oil) due to the large difference in refractive index (n = 1.332 and n = 1.467) and the immiscibility between the two solutions. These solutions are widely used in droplet formation with water in dispersed phase and oil in continuous phase [10-11]. Optical images of the two solutions on nanoLCA showed the expected red-shift appearance in the transmission mode and the blue-shift appearance in the reflection mode due to the increase in refractive index as shown in figure 8.2 (a). The red shift in transmission mode is confirmed with the measured transmission spectra of the two solutions, where the transmission spectrum of water has an intensity peak at 589 nm and that of oil has an intensity peak at 635 nm. To spatially modulate the two immiscible solutions, we fabricated a microfluidic device with flow focusing geometry to generate water droplets in oil emulsion (figure 8.2 (b)) with the flow focus junction placed on the nanoLCA. Figure 8.2 (c) shows the close up view of the water inlet channel and the two oil inlet channels at the flow focusing junction on nanoLCA. Note that in this reflection image the contrast in the color appearance of the two immiscible solutions is apparent and the interface between the two appears as dark regions. The two solutions were perfused into the microfluidic device using two syringe pumps (Harvard Apparatus, MA, USA) at a rate of 10 µL min-1 (water) and 5 µL min-1 (oil), and at steady state, water-in-oil droplets were generated at a rate of approximately one hertz. Figure 8.2 (d) shows a series of time lapsed images of generated water-in-oil droplets traversing across a selected region on nanoLCA. Due to the large sensor area, the entirety of the generated droplet can be visualized at relatively high temporal resolution. More importantly, the difference in refractive index of the water droplet in oil emulsion

can be visualized in real-time as the water droplets wetted the surface of nanoLCA as they traveled toward the outlet. Upon closer inspection, we observed partial wetting at the leading edge of the water droplet where there were green streaks trailing the droplet edge, indicating the gradual displacement of oil molecules by the water molecules as the droplet wets the surface. Likewise, the observed green streak inside the droplet away from the edge of the droplet was due to a thin layer of oil that was trapped on the surface of nanoLCA. This demonstrates the high sensitivity to the refractive index of the solution immediately adjacent to the surface where the evanescent field penetrates approximately 200 nm to 300 nm into the dielectric medium [12].

The on-chip opto-microfluidic nanoLCA device mentioned before can be easily integrated with Raman spectroscopy. By combining with molecule identification from Raman spectroscopy, the in-situ observation of biological reaction such as fluidic mixing, protein-protein binding, DNA hybridization and kinetic study of molecule reaction can be simultaneously observed by high sensitivity and rapid response of visual colorimetric sensing and precise molecule analysis of SERS detection.

8.3. Smartphone based nanoLCA colorimetric platform

As discussed in chapter 7, the rapid colorimetric sensing can be potentially applied to point-of-care and resource limited environments. As a result, a convenient, user-friendly and highly accessible portable sensing platform is the key point for such application. Recently with the dramatic advance of CMOS technique, the computational power of mobile platform has significantly improved and is able to perform complex calculation and analysis without any assistance from external equipment. In addition, the camera on the mobile platform also has made considerable progress in image quality. As a result, the mobile-based imaging platform is the most promising tool to apply to personal health monitoring and is a highly accessible analytical method.

Figure 8.3 (a) shows the prototype of the smartphone sensing platform. It contains an embedded light source at the bottom, which emits light through the nanoLCA sample placed at the middle sample slot. The distance and relative planar position between the smartphone camera and sample can be adjusted manually to ensure the image is taken at normal angle to eliminate any possible diffraction effect from nanostructures within the nanoLCA device. The design of sample is shown in figure 8.3 (b), which has a central circle sensing area with nanoLCA device. Around the sensing region there are 8 square standard colors: (1) full red (R = 255, G = 0 and B = 0), (2) half red (R = 128, G = 0 and B = 0), (3) full green (R = 0, G = 255 and B = 0), (4) half green (R = 0, G = 128 and B = 0), (5) half blue (R = 0, G = 0 and B = 255), (6) half blue (R = 0, G = 0 and B = 128), (7) transparent (R = 0, G = 0 and B = 0), (8) gray (R = 128, G = 128 and B = 128). These standard color regions are used for calibration to achieve better sensing linearity.

The characterization of nanoLCA device on smartphone platform was implemented with different concentrations of glycerol solution (wt% = 10, 20, 30 and 40 %). The optical images are shown in figure 8.4 (a). It can be observed that the color changes when the concentration of glycerol increases. The extracted RGB values are firstly normalized by the full RGB values obtained from standard color regions. Then the corresponding RGB values are calculated by the following equation:

$$\frac{Rescaled\ R, G, B}{\sqrt{(rescaled\ R)^2 + (rescaled\ G)^2 + (resacled\ B)^2}}$$

The original and calibrated RGB values with different concentrations of glycerol are shown in figure 8.4 (b) and (b). It can be observed that better linearity can be achieved after the calibration.

Next, BSA total protein detection using Coomassie (Bradford) Protein Assay was implemented as a proof-of-concept experiment. When mixed with a protein solution, the acidic coomassie-dye reagent changes from brown to blue in proportion to the amount of protein present in the sample. The absorbance spectrum of different concentrations of BSA protein with and without nanoLCA device measured by microplate reader is shown in figure 8.5. The limit of detection has been improved around 10^3 with the assistance of nanoLCA plasmonic effect. Figure 8.6 shows the RGB analysis of different concentrations of BSA total protein measured with the smartphone based platform. The linear sensing region can be observed when the concentration is higher than 1 mg/mL. It proves the concept of using a smartphone as a platform to perform colorimetric sensing.

8.4. Figures

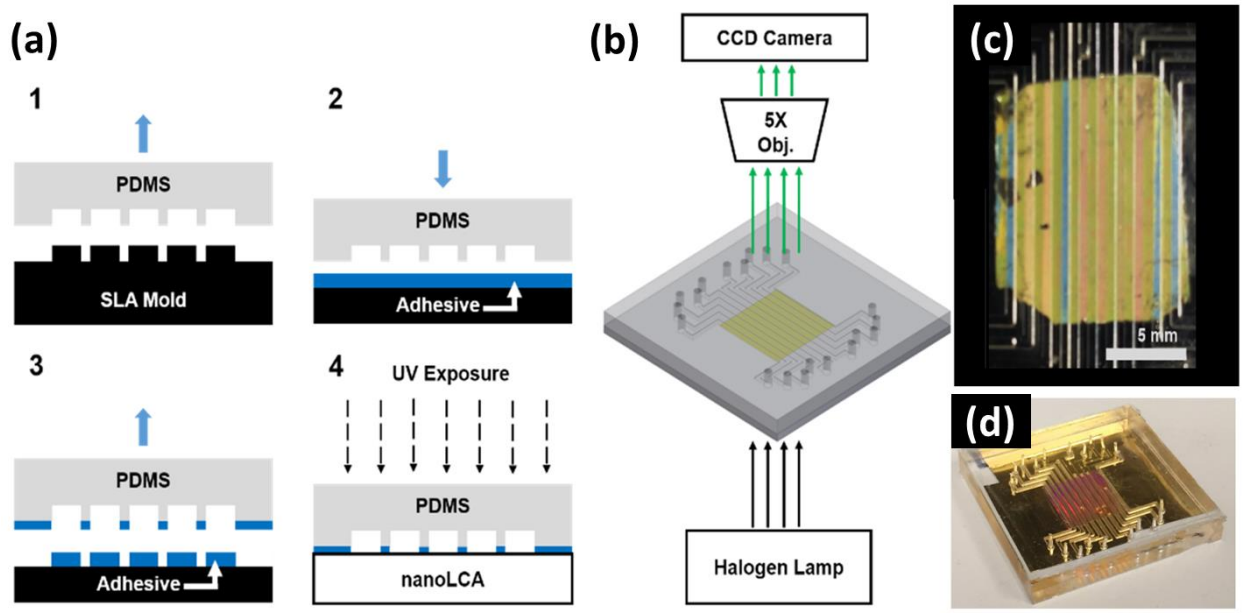

Figure 8.1 Schematic of the construction and the assembly of microfluidic nanoLycurgus Cup Array (nanoLCA) sensor. (a.1) Polydimethylsiloxane (PDMS)-based microfluidic device is replicated from a stereolithography (SLA) master mold. (a.2-3) The microfluidic device is brought into contact with a thin layer of UV-curable optical adhesive and the adhesive is transferred onto the contacted PDMS surface. (a.4) The adhesive-coated microfluidic device is brought into contact with the nanoLCA and the adhesive is cured by exposure to UV light. (b) Colorimetric imaging is performed in transmission and reflection modes using illumination provided by a halogen lamp and imaging using a 5X objective and a CCD camera. (c) A microfluidic device with ten parallel channels bonded to the nanoLCA layer, perfused with various aqueous solutions (yellow and red color appearances) and empty (blue color appearance) (channel width: 500 μm). (d) A scanning electron microscope image of the individual nanocups on nanoLCA after metal deposition.

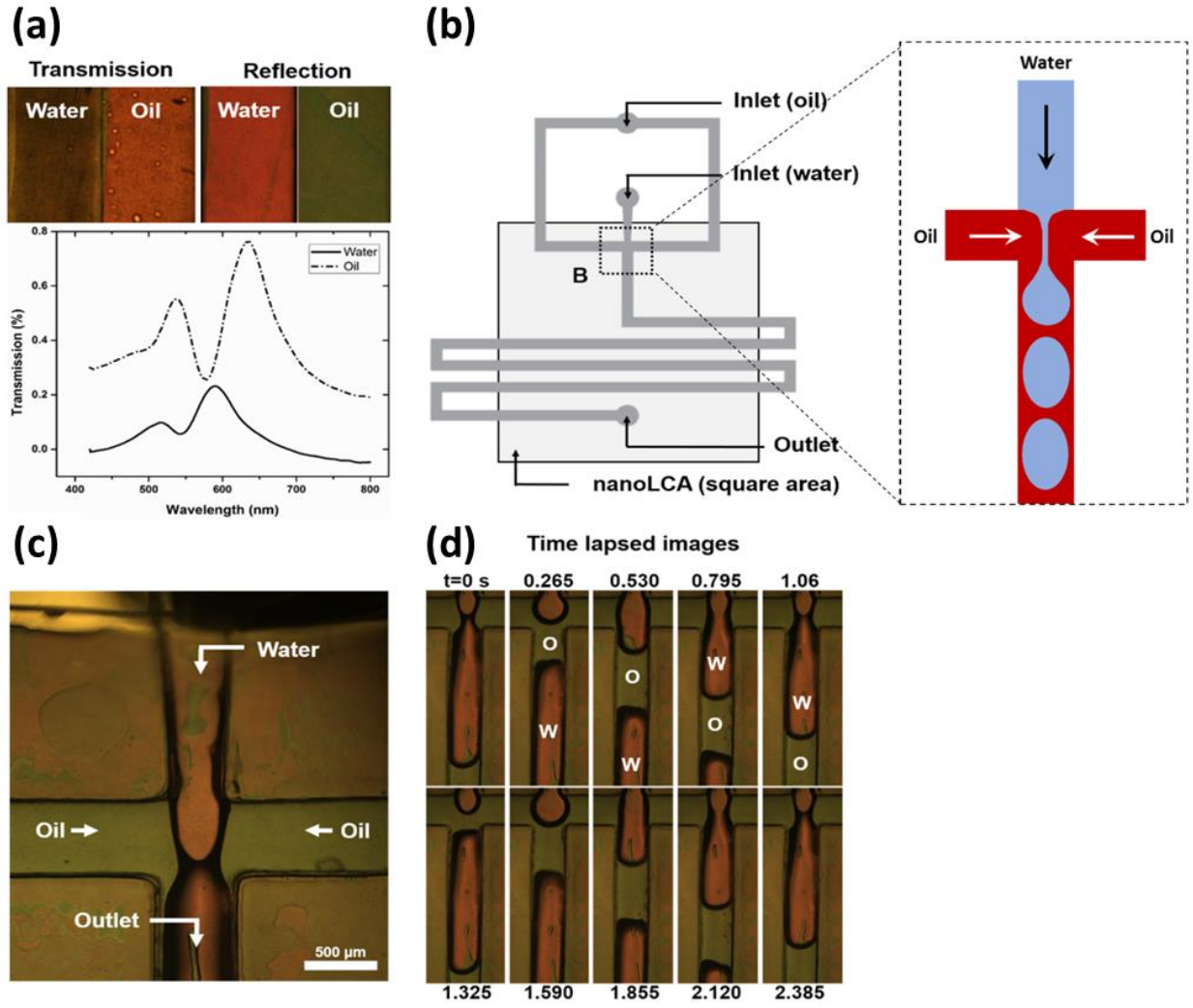

Figure 8.2 Modulation of two immiscible solutions (water and oil) with different refractive indices on microfluidic nanoLCA via micro-droplet generation. (a) Microfluidic scheme for droplet generation, using water-in-oil emulsion, placed over the nanoLCA. (b) Close-up view of the microfluidic droplet generation nozzle region (dotted area from figure A) with top inlet for water and side inlets for oil (solid arrow indicates the direction of the flow). (b) Time lapsed reflection images of water (W) droplet formation, release, and re-formation in oil (O) emulsion at the nozzle region. (d) Top row shows the transmission (left) and reflection (right) colorimetric images of water and oil on the nanoLCA. Bottom plot is the transmission spectra of water and oil on nanoLCA.

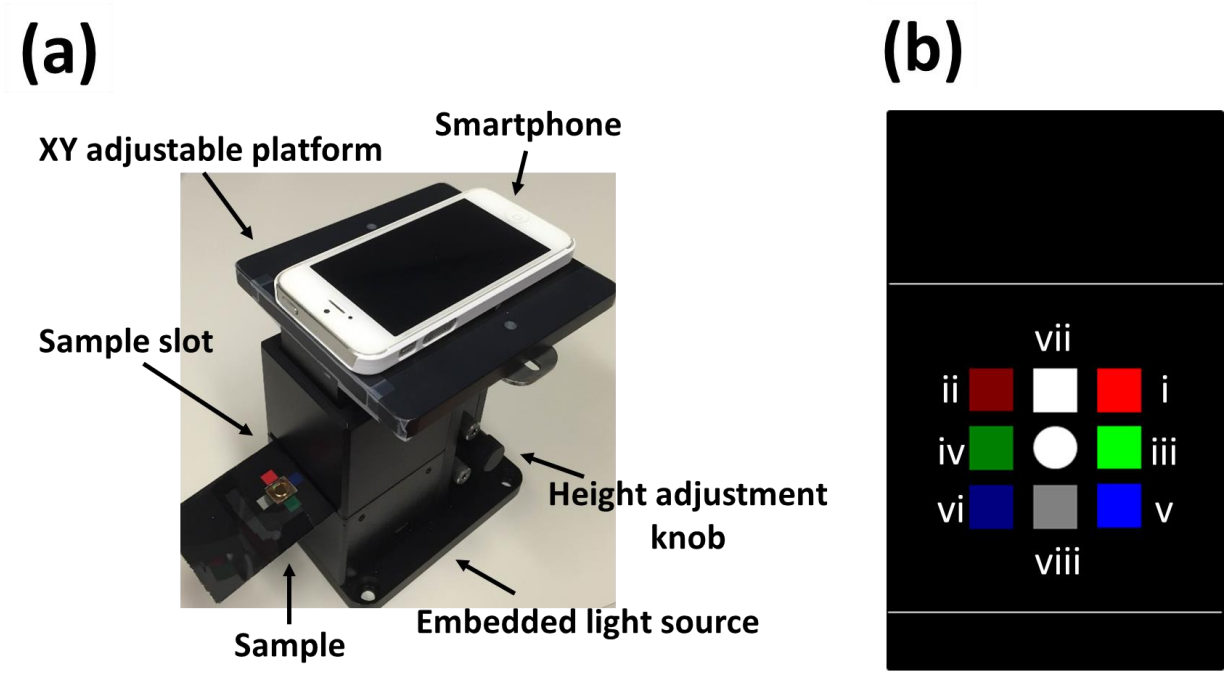

Figure 8.3 (a) The setup of smartphone based colorimetric sensing system. (b) The design of colorimetric sensing sample. The middle circular region contains Au nanoLCA device and 8 square regions from i to viii around are standard colors for calibration (i. full red (R = 255, G = 0 and B = 0); ii. half red (R = 128, G = 0 and B = 0); iii. full green (R = 0, G = 255 and B = 0); iv. half green (R = 0, G = 128 and B = 0); v. half blue (R = 0, G = 0 and B = 255); vi. half blue (R = 0, G = 0 and B = 128); vii. transparent (R = 0, G = 0 and B = 0); viii. gray (R = 128, G = 128 and B = 128)).

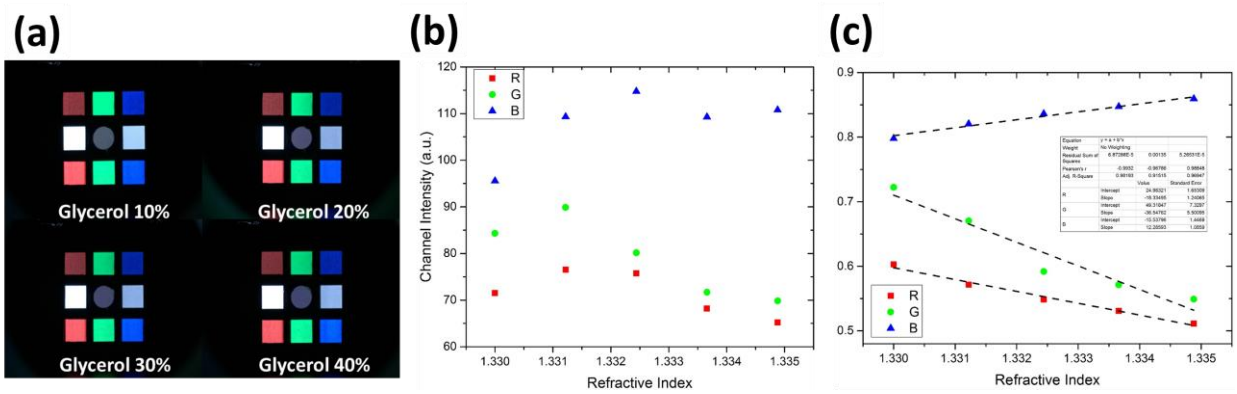

Figure 8.4 (a) The optical images of nanoLCA sample with different concentrations of glycerol taken by smartphone based system.; (b) Extracted and (c) calibrated RGB values with converted refractive index change from different concentrations of glycerol.

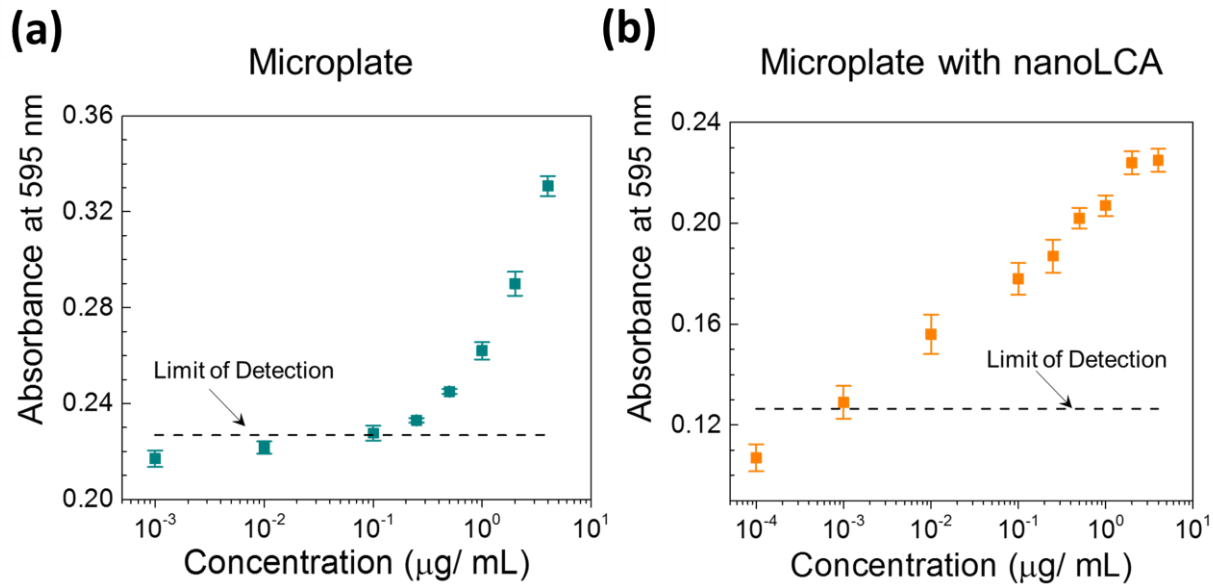

Figure 8.5 The absorbance measurement of different concentrations of BSA protein with Coomassie (Bradford) Protein Assay by microplate reader (a) without and (b) with the nanoLCA device.

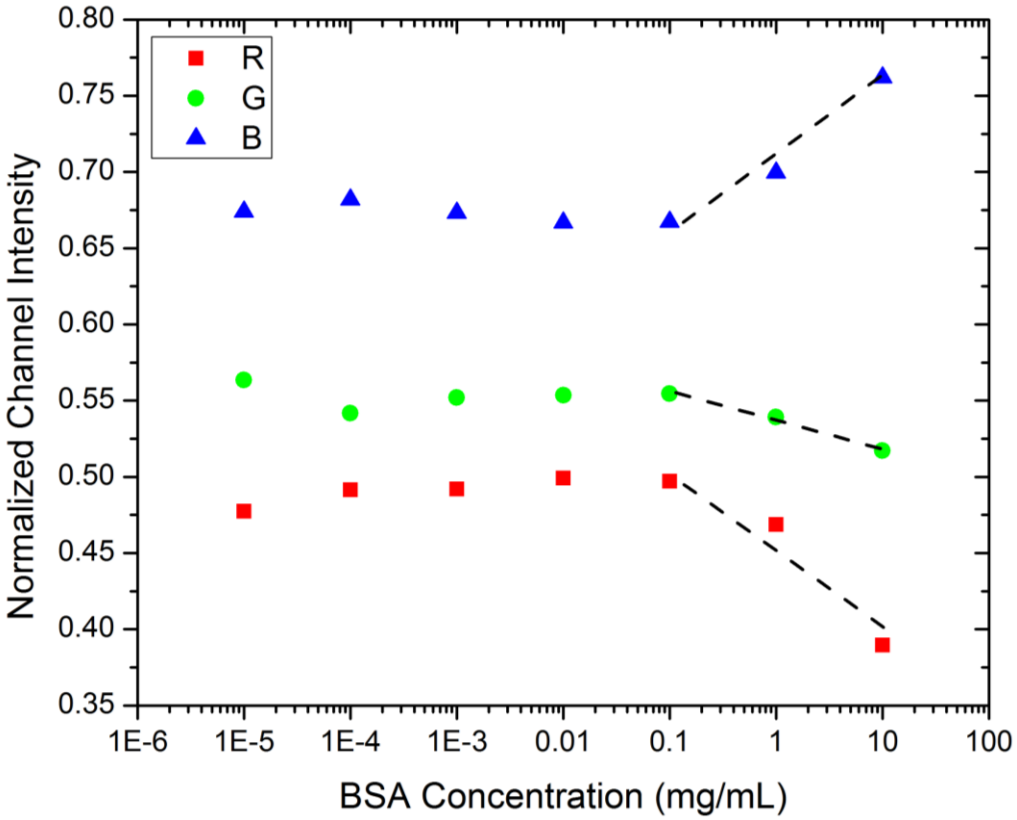

Figure 8.6 The nanoLCA transmission measurement of different concentrations of BSA protein with Coomassie (Bradford) Protein Assay by smartphone based setup.

8.5. References

[1] Sinton, D. Microscale Flow Visualization. *Microfluidics and Nanofluidics* **2004**, *1*, 2-21.

[2] Ng, A. H. C.; Uddayasankar, U.; Wheeler, A. R. Immunoassays in Microfluidic Systems. *Analytical and Bioanalytical Chemistry* **2010**, *397*, 991-1007.

[3] Bange, A.; Halsall, H. B.; Heineman, W. R. Microfluidic Immunosensor Systems. *Biosens. Bioelectron.* **2005**, *20*, 2488-2503.

[4] Lichtman, J. W.; Conchello, J. A. Fluorescence Microscopy. *Nature Methods* **2005**, *2*, 910-919.

[5] J. R. Lakowicz, Principles of fluorescence spectroscopy. New York, N.Y.: Springer, **2006**.

[6] Tate, J.; Ward, G. Interferences in Immunoassay. *The Clinical biochemist Reviews / Australian Association of Clinical Biochemists* **2004**, *25*, 105-20.

[7] Haes, A. J.; Van Duyne, R. P. A Unified View of Propagating and Localized Surface Plasmon Resonance Biosensors. *Analytical and Bioanalytical Chemistry* **2004**, *379*, 920-930.

[8] Fan, X.; White, I. M.; Shopova, S. I.; Zhu, H.; Suter, J. D.; Sun, Y. Sensitive Optical Biosensors for Unlabeled Targets: A Review. *Anal. Chim. Acta* **2008**, *620*, 8-26.

[9] Cooper, M. A. Label-Free Screening of Bio-Molecular Interactions. *Analytical and Bioanalytical Chemistry* **2003**, *377*, 834-842.

[10] Chang, C.; Sustarich, J.; Bharadwaj, R.; Chandrasekaran, A.; Adams, P. D.; Singh, A. K. Droplet-Based Microfluidic Platform for Heterogeneous Enzymatic Assays. *Lab on a Chip* **2013**, *13*, 1817-1822.

[11] Chen, A.; Byvank, T.; Chang, W.; Bharde, A.; Vieira, G.; Miller, B. L.; Chalmers, J. J.; Bashir, R.; Sooryakumar, R. On-Chip Magnetic Separation and Encapsulation of Cells in Droplets. *Lab on a Chip* **2013**, *13*, 1172-1181.

[12] Jung, L. S.; Campbell, C. T.; Chinowsky, T. M.; Mar, M. N.; Yee, S. S. Quantitative Interpretation of the Response of Surface Plasmon Resonance Sensors to Adsorbed Films. *Langmuir* **1998**, *14*, 5636-5648.

APPENDIX A: ENHANCEMENT FACTOR CALCULATION

The calculation of average SERS enhancement factor (EF) used in this thesis (except chapter 5) is explained in the following equation:

$$EF = \frac{I_{SERS}}{I_{Raman}} \times \frac{N_{Raman}}{N_{SERS}} \times \frac{P_{Raman}}{P_{SERS}} \times \frac{T_{Raman}}{T_{SERS}}$$

where I_{SERS} and I_{Raman} are integrated scattered intensities of Raman signal from SERS substrate and BPE bulk solution. N_{SERS} and N_{Raman} are the numbers of molecules being probed on SERS substrate and in the BPE bulk solution. P_{SERS} and P_{Raman} are the power intensities of excitation laser applied onto SERS substrate and BPE bulk solution. T_{SERS} and T_{Raman} are the acquisition times when measuring Raman signal on the SERS substrate and in the BPE bulk solution. I_{SERS} and I_{Raman} were measured with the integrated peak intensity. Active Raman enhanced surface area is calculated as the total surface area of metal covered on the device. The laser spot size and focal length after 20X objective lens were measured as 6.06 μm and 3 mm [1]. The surface area of single BPE molecule is 30 $Å^2$ [2]. The concentration of BPE bulk solution was 100 mM. As a result, N_{Raman} can be calculated as 5.22×10^{12}.

A.1 References

[1] E. C. Le Ru, E. Blackie, M. Meyer, P. G. Etchegoin, *J. Phys. Chem. C* **2007**, *111*(37), 13794-13803.

[2] N. Felidj, J. Aubard, G. Levi, J. R. Krenn, M. Salerno, G. Schider, B. Lamprecht, A. Leitner, F. R. Aussenegg, *Phys. Rev. B* **2002**, *65*(7), 075419